



**EXPERIMENTAL RESULTS FOR A HIGH
SWIRL, ULTRA COMPACT COMBUSTOR
FOR GAS TURBINE ENGINES**

THESIS

Ryan J. Quaale, Captain, USAF
AFIT/GAE/ENY/03-5

**DEPARTMENT OF THE AIR FORCE
AIR UNIVERSITY**

AIR FORCE INSTITUTE OF TECHNOLOGY

Wright-Patterson Air Force Base, Ohio

APPROVED FOR PUBLIC RELEASE; DISTRIBUTION UNLIMITED.

The views expressed in this thesis are those of the author and do not reflect the official policy or position of the United States Air Force, Department of Defense, or the United States Government.

AFIT/GAE/ENY/03-5

EXPERIMENTAL RESULTS FOR A HIGH SWIRL, ULTRA COMPACT
COMBUSTOR FOR GAS TURBINE ENGINES

THESIS

Presented to the Faculty

Department of Aeronautics and Astronautics

Graduate School of Engineering and Management

Air Force Institute of Technology

Air University

Air Education and Training Command

In Partial Fulfillment of the Requirements for the
Degree of Master of Science in Aeronautical Engineering

Ryan J. Quaale, BS, MSEM

Captain, USAF

March 2003

APPROVED FOR PUBLIC RELEASE; DISTRIBUTION UNLIMITED.

EXPERIMENTAL RESULTS FOR A HIGH SWIRL, ULTRA COMPACT
COMBUSTOR FOR GAS TURBINE ENGINES

Ryan J. Quaale, BS, MSEM
Captain, USAF

Approved:

| | |
|---|---------------|
| _____/SIGNED/_____ Ralph A. Anthenien (Chairman) | _____ date |
|---|---------------|

| | |
|---|---------------|
| _____/SIGNED/_____ Milton E. Franke (Member) | _____ date |
|---|---------------|

| | |
|---|---------------|
| _____/SIGNED/_____ Mark F. Reeder (Member) | _____ date |
|---|---------------|

Acknowledgments

I would like to thank my advisor Captain Ralph Anthenien who provided guidance and assistance throughout the data collection and writing process. His talent and interest in combustion have been an encouragement and his caring attitude is a credit to his integrity.

I would like to especially thank Dr. Julian M. Tishkoff from AFOSR/NA and Dr. Robert Hancock AFRL/PRTS who provided funding and support to make this project possible.

In everything I have done the Lord Jesus Christ has been there to guide me and I thank him each day for his tremendous blessings.

I have accomplished nothing without the help of others. Most important is my wife who has shown me what it means to enjoy life and be passionate. She has also shown me love I would never have known without her.

My parents have always encouraged me in everything I have done and have always taken time to witness everything from the minor to most significant events in my life. They have obviously helped shape me into the person I am today.

My in-laws have also been a tremendous encouragement and supported me throughout this experience and I thank them deeply.

Ryan J. Quaale

Table of Contents

| | Page |
|---|-------|
| Acknowledgments | iv |
| List of Figures | viii |
| List of Tables | xii |
| List of Symbols | xiii |
| Abstract | xviii |
| I Introduction and Overview | 1 |
| I.1 Motivation | 1 |
| I.2 Method | 2 |
| I.3 Conventional Combustor Types | 3 |
| I.4 Data Analysis | 4 |
| I.5 Thesis Content | 4 |
| II Background and Theory | 5 |
| II.1 Combustor | 5 |
| II.1.1 Diffuser | 5 |
| II.1.2 Primary Zone | 6 |
| II.1.3 Intermediate Zone | 6 |
| II.1.4 Dilution Zone | 6 |
| II.2 Trapped Vortex Combustor | 7 |
| II.3 Ultra-Compact Combustor Concept | 8 |
| II.4 Thermodynamic Cycle | 9 |
| II.4.1 Inlet and Diffuser | 11 |
| II.4.2 Compressor | 11 |
| II.4.3 Main Burner | 11 |
| II.4.4 Conventional Turbine Configuration | 12 |
| II.4.5 Inter-Turbine Burner Configuration | 12 |
| II.4.6 Afterburner | 13 |
| II.4.7 Nozzle | 14 |
| II.4.8 Engine Performance and Analysis | 14 |
| II.5 Centripetal Acceleration | 15 |
| II.6 Taylor Vortices | 16 |
| II.7 Analytical Model | 17 |
| II.7.1 Cavity Air Navier-Stokes Equations | 17 |
| II.7.2 Main Air Navier-Stokes Equations | 19 |

| | Page |
|---|------|
| II.8 Laser Doppler Velocimetry | 21 |
| II.8.1 Fringe Pattern and Speed Measurement | 22 |
| II.8.2 Frequency Shifting..... | 23 |
| II.8.3 Lasers and Optics..... | 24 |
| II.8.4 Seeding | 25 |
| II.8.5 Velocity Biasing | 25 |
| II.9 Combustion..... | 26 |
| II.9.1 Deflagration | 27 |
| II.9.2 Chemical Reaction..... | 28 |
| II.9.3 Reaction Rate..... | 28 |
| II.9.4 Carbon Monoxide | 29 |
| II.9.5 Unburned Hydrocarbons..... | 29 |
| II.9.6 Soot..... | 30 |
| II.9.7 Nitrogen Oxides..... | 30 |
| III Experimental Configuration | 33 |
| III.1 Ultra Compact Combustor Setup..... | 33 |
| III.1.1 Centerbody..... | 33 |
| III.1.2 Liner Ring..... | 33 |
| III.1.3 Pressure Ring..... | 34 |
| III.1.4 Mounting Flange..... | 34 |
| III.1.5 Quartz Window..... | 34 |
| III.1.6 Exhaust System..... | 35 |
| III.2 Laser Setup | 35 |
| III.3 Data Collection Facilities | 36 |
| III.4 NO _x Measurements | 37 |
| III.5 Hydrocarbon Measurements..... | 37 |
| III.6 Carbon Monoxide and Carbon Dioxide Measurements | 37 |
| IV Results and Discussion | 39 |
| IV.1 Experiment and Models..... | 39 |
| IV.2 Velocity Measurements | 39 |
| IV.3 Combustion Efficiency | 44 |
| IV.4 CO Emissions | 46 |
| IV.4.1 Chemical Kinetics..... | 47 |
| IV.5 Error Analysis..... | 48 |
| IV.6 CFD Temperature Calculations | 49 |
| IV.7 Analytical Analysis..... | 50 |
| IV.7.1 Cavity Flow | 50 |
| IV.7.2 Main Flow..... | 52 |

| | |
|---|------|
| | Page |
| V Conclusion | 56 |
| V.1 Conclusions..... | 56 |
| V.2 UCC Future..... | 58 |
| Appendix A: Figures..... | 59 |
| Appendix B: Analytical Derivation | 94 |
| Appendix C: Recommendations | 105 |
| Bibliography | 107 |
| Vita | 110 |

List of Figures

| | Page |
|---|------|
| Figure 1: Conventional Combustor (adapted from Lefebvre, 1999:17) | 59 |
| Figure 2: UCC Rear View and UCC Cavity Side View (used with permission from Anthenien, 2001:6) | 59 |
| Figure 3: UCC Partially Disassembled Rear View Picture | 60 |
| Figure 4: Integration of the UCC and Turning Vanes (used with permission from Anthenien, 2001:6) | 61 |
| Figure 5: Conventional (dashed line) and ITB Cycle (solid line) T-s Diagram (adapted from Sirignano and Liu, 2001:2) | 61 |
| Figure 6: Engine Stations (adapted from Sirignano and Liu, 2001:2)..... | 62 |
| Figure 7: UCC Boundary Condition Locations (rear view not to scale) | 62 |
| Figure 8: LDV Laser Setup Diagram for Forward Scatter (adapted from Wheeler and Ganji, 1996:311) | 63 |
| Figure 9: Fringe Diagram for LDV (adapted from Drain, 1980:86) | 63 |
| Figure 10: Frequency Shift for Velocity Determination..... | 64 |
| Figure 11: Experimental UCC Cross Section..... | 64 |
| Figure 12: Liner Ring (used with permission from Ehret, 2002: Appendix A) | 65 |
| Figure 13: Quartz Window Picture Following Testing | 66 |
| Figure 14: Pressure and Temperature Tap Locations | 67 |
| Figure 15: Diagram of LDV Measurement Positions A, B and C..... | 67 |
| Figure 16: Circumferential and Radial Velocities at ~22% Cavity Air Mass Flow For All Equivalence Ratios (Position A)..... | 68 |
| Figure 17: Circumferential and Radial Velocities at ~22% Cavity Air Mass Flow For All Equivalence Ratios (Position C) | 68 |

| | |
|---|----|
| Figure 18: CFD Raw Data Plot of Circumferential Velocity at 4% Pressure Drop In Line with Upstream Air Jets (used with permission from Ehret) | 69 |
| Figure 19: CFD Raw Data Plot of Circumferential Velocity at 2% Pressure Drop In Line with Upstream Air Jets (used with permission from Ehret) | 70 |
| Figure 20: Circumferential and Radial Velocities at ~22% Cavity Air Mass Flow For All Equivalence Ratios (Position B) | 71 |
| Figure 21: CFD Raw Data Plot of Circumferential Velocity at 4% Pressure Drop In Line with Fuel Injector (used with permission from Ehret)..... | 72 |
| Figure 22: CFD Raw Data Plot of Circumferential Velocity at 2% Pressure Drop In Line with Fuel Injector (used with permission from Ehret)..... | 73 |
| Figure 23: U_θ Mean for All Equivalence Ratios (Position A) | 74 |
| Figure 24: U_r Mean for All Equivalence Ratios (Position A) | 74 |
| Figure 25: U_θ Mean for All Equivalence Ratios (Position B) | 75 |
| Figure 26: U_r Mean for All Equivalence Ratios (Position B)..... | 75 |
| Figure 27: U_θ Mean for All Equivalence Ratios (Position C) | 76 |
| Figure 28: U_r Mean for All Equivalence Ratios (Position C)..... | 76 |
| Figure 29: Main Air Effect on U_θ Mean for All Equivalence Ratios (Position A)..... | 77 |
| Figure 30: Main Air Effect on U_r Mean for All Equivalence Ratios (Position A)..... | 77 |
| Figure 31: Main Air Effect on U_θ Mean for All Equivalence Ratios (Position B)..... | 78 |
| Figure 32: Main Air Effect on U_r Mean for All Equivalence Ratios (Position B) | 78 |
| Figure 33: Main Air Effect on U_θ Mean for All Equivalence Ratios (Position C)..... | 79 |
| Figure 34: Main Air Effect on U_r Mean for All Equivalence Ratios (Position C) | 79 |
| Figure 36: Effect of Main and Cavity Air Mass Flow on Radial Turbulence Intensity (Position A)..... | 80 |

| | |
|---|----|
| Figure 37: Effect of Main and Cavity Air Mass Flow on Radial Turbulence Intensity (Position B) | 81 |
| Figure 38: Effect of Main and Cavity Air Mass Flow on Radial Turbulence Intensity (Position C) | 81 |
| Figure 39: Effect of Main and Cavity Air Mass Flow on Circumferential Turbulence Intensity (Position A) | 82 |
| Figure 40: Effect of Main and Cavity Air Mass Flow on Circumferential Turbulence Intensity (Position B) | 82 |
| Figure 41: Effect of Main and Cavity Air Mass Flow on Circumferential Turbulence Intensity (Position C) | 83 |
| Figure 42: Circumferential Velocities for Positions A, B and C with Main Air Mass Flow | 83 |
| Figure 43: Circumferential Velocities for Positions A, B and C with Cavity Air Mass Flow | 84 |
| Figure 44: Radial Velocities for Positions A, B and C with Main Air Mass Flow | 84 |
| Figure 45: Radial Velocities for Positions A, B and C with Cavity Air Mass Flow | 85 |
| Figure 46: Impact of Φ on G-Loading and Cavity Mass Flow (Position A) | 85 |
| Figure 47: Impact of Φ on G-Loading and Cavity Mass Flow (Position B) | 86 |
| Figure 48: Impact of Φ on G-Loading and Cavity Mass Flow (Position C) | 86 |
| Figure 49: Impact of Φ on Efficiency and G-Loading (Position A) | 87 |
| Figure 50: Efficiency with changes in Longwell Loading Parameter | 87 |
| Figure 51: Changes in CO Emission Index with G-Loading (Position A) | 88 |
| Figure 52: Longwell Loading Parameter and CO Emission Index | 88 |
| Figure 53: Diagram of Chemical Kinetics Model for the UCC | 89 |
| Figure 54: Chemical Kinetics Numerical Results for CO Emission Index with Longwell Loading Parameter | 89 |

| | |
|--|----|
| Figure 55: CFD Temperature Plot In Line With the Upstream Pilot Air Jets For 2% Pressure Drop at 22% Cavity Air Mass Flow (used with permission from Ehret, 2002: Appendix A)..... | 90 |
| Figure 56: CFD Temperature Plot In Line With the Fuel Injector For 2% Pressure Drop at 22% Cavity Air Mass Flow (used with permission from Ehret, 2002: Appendix A)... | 91 |
| Figure 57: CFD Temperature Plot In Line With the Upstream Pilot Air Jets For 4% Pressure Drop at 22% Cavity Air Mass Flow (used with permission from Ehret, 2002: Appendix A)..... | 92 |
| Figure 58: CFD Temperature Plot In Line With the Fuel Injector For 4% Pressure Drop at 22% Cavity Air Mass Flow (used with permission from Ehret, 2002: Appendix A)... | 93 |

List of Tables

| | Page |
|---|------|
| Table 1: Cavity Flow Boundary Conditions | 19 |
| Table 2: Main Flow Boundary Conditions | 21 |
| Table 3: LDV Advantages and Disadvantages | 22 |
| Table 4: Test Matrix | 40 |
| Table 5: Experimental and CFD Mean Velocities (Positions A, B, C) | 42 |
| Table 6: Cavity Flow Assumptions | 50 |
| Table 7: Cavity Flow Non-Dimensionalization | 51 |
| Table 8: Cavity Flow Similarity Boundary Conditions | 52 |
| Table 9: Main Flow Assumptions | 53 |
| Table 10: Main Flow Non-Dimensionalization | 54 |
| Table 11: Main Flow Similarity Boundary Conditions | 54 |

List of Symbols

Nomenclature

A = Arrhenius pre-exponential factor for 2nd order [cc/mols]

c = Speed of light [m/s]

C_p = Constant pressure specific heat

D = Mass diffusivity [m²/s]

Da = Damkohler number [1]

E = Activation energy [J/mol K] or [cal/mol K]

EI = Emission Index [g/kg]

f = frequency [1/s]

g = gravitational constant [m/s²]

h = heat transfer coefficient [W/m² K]

k = thermal conductivity [W/m K]

K = Arrhenius reaction rate [mol/cc]¹⁻ⁿ[1/s]

Le = Lewis number [1]

M = Mach number [1]

P = Power [W]

P = Pressure [Pa]

Pe = Peclet number [1]

Q_R = Fuel heating value [J/kg]

r = Radial direction [m]

R = Radial location in the UCC [m], Gas constant [J/mol K]

s = Entropy [J/K] or [J/kg K] for specific entropy

S = Fringe width [m]

S_B = Flame speed [m/s]

T = Temperature [K]

TI = Turbulence Intensity [%]

u_e = Exit velocity [m/s]

U_r = Radial velocity [m/s]

U_R = Velocity at a specific radius R [m/s]

U_θ = Circumferential velocity [m/s]

U_z = Axial velocity [m/s]

V = Velocity (General) [m/s], Volume [m³]

V_f = Fringe velocity [m/s]

Y = Mass fraction [1]

z = Axial direction [m]

Symbols

α = Angle between laser beams [deg], thermal diffusivity [m²/s]

β = Coupling Function

ϕ = Equivalence Ratio [1]

μ = Refractive index [1], viscosity [kg/m s]

Δh_f° = Heat of formation [J/kg]

ν = kinematic viscosity [m²/s]

θ = Circumferential direction [deg]

ν = Light wave frequency [1/s]

λ = Wavelength [m]

γ = Ratio of specific heats for air [1]

\dot{m} = Mass flow rate [kg/s]

η = Efficiency

ω = Heat Generation [J/s kg]

π = Pressure ratio [1]

ρ = Density [kg/m³]

ζ = Similarity variable

Subscripts

a = Atmospheric, Air

ab = Afterburner

av = Average

b = Burner

c = Compressor

d = Diffuser

fab = Fuel to the afterburner

fb = Fuel to the burner

ftb = Fuel to the turbine burner

i = Species (General)

N = Nozzle

o = Sea level, initial

O = Oxygen

std.dev. = Standard deviation

t = Turbine

tb = Turbine burner

02 = Diffuser inlet

03 = Compressor inlet

04 = Burner inlet

05 = Conventional cycle turbine inlet

05' = ITB cycle turbine inlet

06 = Conventional cycle afterburner inlet

06' = ITB cycle afterburner inlet

07 = Nozzle inlet

inner = Inner location of the cavity

outer = Outer wall of the cavity

centerbody = Inner wall of the main flow

Glossary

CFD = Computational Fluid Dynamics

CTB = Continuous Turbine Burner

ITB = Inter Turbine Burner

LLP = Longwell Loading Parameter

LDV = Laser Doppler Velocimetry

MTBM = Mean Time Between Maintenance

RQL = Rich burn, Quick quench, Lean burn

TSFC = Thrust Specific Fuel Consumption

T/W = Thrust to Weight Ratio

TVC = Trapped Vortex Combustor

ST = Specific Thrust

UAV = Unmanned Air Vehicle

UCC = Ultra Compact Combustor

WSR = Well Stirred Reactor

Abstract

Laser Doppler Velocimeter (LDV) experiments have been conducted within the cavity of an atmospheric pressure, small scale, Ultra Compact Combustor (UCC). The UCC uses highly swirled flow in a cavity around the outside periphery of the combustor to generate high centripetal acceleration in the fluid. This enhances mixing and leads to a very short axial flame length. Additionally, due to the circumferential velocity, much of the residence time required by the flame is provided by the circumference of the engine rather than axial length as in conventional combustors. These two effects combine to produce observed flame lengths less than half those of conventional swirl stabilized combustors. These short flame lengths lend themselves to reduced engine size and weight and open the possibility for inter-turbine burning (ITB) reheat cycles for aircraft engines. The ITB reheat cycle has been shown to have the potential for large gains in specific thrust (>50%) with equal or reduced thrust specific fuel consumption (Anthenien and others, 2001:1). The LDV experiments were conducted in a small scale, atmospheric pressure, axi-symmetric combustor. Swirl is generated by air entering through evenly spaced holes angled radially at 45 degrees on the cavity outer perimeter. Cavity mass flow is roughly 22% of the main axial mass flow and may be controlled independently. JP-8 fuel is injected into the cavity by pressure atomizing nozzles. The measurements were conducted using a two-component LDV system in back-scatter. Flow measurements indicate circumferential velocities of 20-45 m/s with average turbulence intensities of 30%. These velocities correspond to accelerations of 1000-4500g. By

comparison, conventional swirl stabilized flames have accelerations of $\sim 100g$ (Anthenien and others, 2001:1). Increasing g-loading values have shown a direct relationship to increased efficiency. These measurements compare favorably to results from a concurrent CFD model. Combustion efficiencies of 99+% have been recorded over a wide range of operating conditions and Longwell Loading Parameters down to $O(10^7)$. High efficiencies were observed for cavity equivalence ratios from $\phi = 0.8$ to $\phi = 1.5$. Hydrocarbon, CO, and CO₂ emissions data were recorded concurrent with LDV measurements. Reduced CO emissions are clearly linked to the enhanced residence time gained by using the engine circumference. Data collected in these experiments is used to validate results from the CFD model and optimize air hole injection spacing and angles in the next configuration. An analytical model of the UCC was also created that further validates the LDV measurements. Cavity and main flows were linked through adjoining boundary conditions. There is agreement between the experimental and numerical data. These results favor the UCC as a possibility for use in future aircraft engines.

EXPERIMENTAL RESULTS FOR A HIGH SWIRL, ULTRA COMPACT COMBUSTOR FOR GAS TURBINE ENGINES

I Introduction and Overview

I.1 Motivation

Gas turbine engines are constantly improving with new innovations to make them smaller, more efficient and more environmentally friendly. The allure of a significantly shorter combustor or an ultra-compact combustor (UCC) for gas turbine aircraft engines is two fold. First, a combustor that is shortened by as much as ~33% reduces the weight of the engine, which can greatly improve thrust to weight ratio (T/W) (Anthenien and others, 2001:2). Second, a combustor made short enough with no penalty in efficiency or emissions makes it possible to add a reheat cycle between turbines. The UCC can also be combined with the turning vanes to the Low Pressure Turbine (LPT) and with the turning vanes between the LPT and High Pressure Turbine (HPT). Finally, the stator used to straighten flow into the burner can be eliminated because the swirling motion is desirable for use in the UCC. All changes taken together could make a UCC engine as much as ~66% shorter than an engine with a conventional combustor system (Anthenien and others, 2001:2).

These changes allow for combinations of improvements for engines with different requirements. An engine with a UCC main burner and a UCC reheat cycle can provide a significant increase in specific thrust (ST) beyond that of a conventional engine of the same size with no penalty in thrust specific fuel consumption (TSFC) (Anthenien and others, 2001:1). Alternatively, a smaller more fuel efficient engine could be produced

that provides the same thrust as a larger, conventional engine with an improvement in T/W. Finally, a similar size engine with the same ST and TSFC can provide longer turbine blade life and ultimately reduce the engine mean time between maintenance (MTBM) through lower turbine inlet temperatures.

Theory and data collected from the Trapped Vortex Combustor (TVC) (Roquemore and others, 2001:1) concepts was used in the development of the UCC. Research conducted by Lewis was used to support the concept of high g-loading to enhance mixing for complete combustion in a small volume (Lewis, 1973:413-418). Sirignano and Liu performed a cycle analysis that supports the UCC as a method for developing jet engines with a reheat cycle (Liu and Sirignano, 2000:1-8). Finally, the UCC builds upon the Jet Swirl High Loading Combustor research done by Yonezawa et al. Benefits from high g-loading in a combustor were confirmed, which supported development of the UCC concept (Yonezawa and others, 1990:1-7).

1.2 Method

Initial design of the UCC was completed by Anthenien et al. (Anthenien and others, 2001:1-7) in the Propulsion Branch (PRTS) of the Air Force Research Laboratory (AFRL) and a CFD modeling effort was later made by Ehret (Ehret, 2002:Ch 1-6). Flow velocity experimental data was desired to validate the CFD effort. Relations between g-loading and performance of the combustion process inside the cavity were also necessary to validate the assumption that g-loading enhances the mixing process. Laser Doppler Velocimetry (LDV) was chosen to measure the circumferential and radial velocities in the UCC cavity. Emissions, pressure, and temperature data were also taken to further validate findings. A range of main air, cavity mass flows and equivalence ratios were

used to find the operating range of the UCC and performance at these design points. Efficiency data was also calculated, and with velocity measurements the effect of g-loading on combustor performance has been attained. Many combinations of mass flow, g-loading, efficiency, emissions, equivalence ratio, and Longwell Loading Parameter (LLP) were compared against one another to analyze trends. Finally, for analytical purposes the combustor was split into two portions, the cavity and main flow. An analytical model was created for each piece with qualifying assumptions and the two parts were coupled through boundary conditions at their interface. The combined results helped validate the experimental and numerical data that was taken with LDV and CFD. The combined information from these three sources will orchestrate design changes in the UCC for future configurations.

I.3 Conventional Combustor Types

The three main types of conventional swirl stabilized gas turbine combustors are tubular, tuboannular, and annular. The tubular combustor consists of several cylindrical combustor liners mounted concentrically inside another larger cylindrical pressure casing. Depending on the engine there may be several of the concentric cylinders mounted around the engine core (Lefebvre, 1999:9). Tubular combustors are mostly used in industry where ease of maintenance is important. Tuboannular combustors consist of several cylindrical liners mounted around the core and inside a single annular pressure casing. This configuration combines the compactness of an annular chamber with the mechanical strength of the tubular chamber. However, consistent airflow can be difficult to obtain and diffuser design is difficult (Lefebvre, 1999:9). The annular combustor consists of an annular pressure casing concentric around an annular combustor liner that

is concentric around the engine core. This design allows for a more compact unit with much less pressure loss than the other two types. However, there is a very heavy buckling load on the outer liner, which has restricted annular combustors to low pressure ratios in the past (Lefebvre, 1999:12). The UCC can be considered an annular combustor type that will use the circumference of the annulus for burning. It is also possible the UCC could be incorporated into each tube of a tuboannular combustor.

I.4 Data Analysis

Plots of velocity calculated from the CFD model were compared against plots of velocity and emissions data from the LDV experiments. Analysis of the CFD data was obtained through contour and raw data plots of a 60 deg periodic section of the UCC. The model was programmed to have the same elements that exit the downstream side of the cavity also enter the upstream side to simulate fluid completing the entire circumference.

I.5 Thesis Content

This work covers the experimental work completed on the UCC and the velocity and emissions measurements taken. A comparison is done between the data collected in the experiments and a previously completed CFD effort (Ehret, 2002:Ch1-6).

Additionally, an analytical model of the UCC has been created that is also compared against the experimental and CFD data. Finally, conclusions about the data collected are assessed to address trends that lead to hypotheses.

II Background and Theory

II.1 Combustor

A combustor is divided into three zones called primary, intermediate, and dilution. The diffuser encases these zones and prepares the air for proper conditions before ignition. The zones each serve a different role in the combustion process. These parts are shown in Fig. 1 as they appear in a conventional combustor.

II.1.1 Diffuser

A combustor consists of several basic components that allow it to operate. First, it is necessary to minimize the static pressure drop across the combustor to keep high efficiency. Pressure drop through the combustor can be separated into two categories: cold and hot loss. The cold pressure loss is due to drag from pushing the air through the combustor and the hot pressure loss comes from adding heat to high velocity air. The cold pressure loss consists of drag loss due to the diffuser and the liner. However, diffuser pressure loss is wasted while the liner pressure loss contributes to turbulence that is beneficial to mixing. Values of cold pressure loss are typically between 2.5 and 5 percent of inlet pressure (Lefebvre, 1999:13-15). Hot pressure loss occurs whenever heat is added to a flowing gas and can be represented by the following equation.

$$\Delta P_{hot} = \frac{1}{2} \rho U^2 \left(\frac{T_4}{T_3} - 1 \right) \quad (1)$$

Lower inlet velocity (U) will greatly reduce the hot pressure loss due to a non-linear relationship. The diffuser will reduce the inlet air velocity, recover much of the dynamic pressure, and provide the liner with a stable flow (Lefebvre, 1999:13-15). The lower velocity is also necessary to prevent blow-off and keep the flame stabilized.

II.1.2 Primary Zone

The main function of the primary zone is to provide a stable flame and complete combustion of the fuel-air mixture. An important feature of the primary zone is to provide a toroidal flow reversal that causes recirculation of hot combustion gases for continuous ignition. Equivalence ratio (ϕ) is used to describe the amount of fuel and air in the combustor. Equivalence ratios less than one are fuel lean and ratios greater than one are fuel rich. The ϕ in this zone is generally greater than one, which is important to aircraft engines because it increases stability and helps prevent lean blow-out (Lefebvre, 1999:15).

II.1.3 Intermediate Zone

High concentrations of CO and UHCs result from equivalence ratios greater than one. Adding air mass to the intermediate zone can decrease the temperature from the primary zone and lower the equivalence ratio below one. This will cause burnout of soot and allow CO and other unburned hydrocarbons to completely burn. Otherwise, CO and possibly UHCs will be released from the combustor as a pollutant and combustion efficiency is decreased (Lefebvre, 1999:15-16).

II.1.4 Dilution Zone

The dilution zone takes in the remaining air after combustion and wall cooling. It quenches the reaction and decreases the temperature of the products to a level that is acceptable for the turbine. If too many radicals are left in the air from the combustion process they will damage the turning vanes or turbine blades when they recombine and release heat. Also, if the temperature is above the maximum temperature for the turbine blade material then the blades will also become damaged over time (Lefebvre, 1999:16).

The dilution zone increases turbine life and therefore contributes significantly to decreasing the MTBM.

II.2 Trapped Vortex Combustor

The AFRL Propulsion Branch previously developed a trapped vortex combustor (TVC) to provide low emission and high performance for a gas turbine combustor (Roquemore and others, 2001:1-5). The TVC consists of staged main and pilot combustion zones. The pilot is created by a stable recirculation zone where a combusting vortex is trapped in a small cavity. This eliminates the need for a primary combustion zone in front of the intermediate zone where combustion can become unstable. This also makes a more compact combustion design. The vortex is sustained by properly placed fuel and air jets that enhance the swirling motion. The combusting fuel and air are transported along the front wall toward the main air mass flow from the cavity to the intermediate zone in the main flow where combustion is completed. A large range of main air flow velocities are allowable because the pilot zone is protected in the cavity from blow out. According to Roquemore et al. the TVC concept can provide a low emissions alternative with high performance (Roquemore and others, 2001:1-5). The very stable cavity pilot configuration offers very low lean blow out limits and the ability to relight at high altitudes. Exceptional mixing provides low NO_x emissions and high combustion efficiencies. This concept also provided a stepping stone for the UCC because the same mixing enhancements and cavity configuration were analyzed for future advancements (Roquemore and others, 2001:1-5).

II.3 Ultra-Compact Combustor Concept

A conventional swirl stabilized gas turbine combustor is designed to complete the burning process in the axial direction of the engine as in Fig. 1. The UCC uses the circumference of the engine to complete the burning process and thereby significantly saves space. Additionally, the acceleration due to the swirl significantly enhances the combustion process, further shortening the flame (Anthenien and others, 2001:1). A diagram of the UCC is shown in Fig. 2 and a photograph of the UCC partially disassembled in Fig. 3. If a conventional combustor were made this short the residence time would be insufficient and complete combustion will not occur before entering the turbine blades. This would severely limit the life of the turbine blades and cause frequent maintenance and poor efficiency. The UCC provides complete combustion by allowing sufficient residence time and reduced chemical time through enhanced mixing in a very short axial distance. This enhanced mixing is a result of the very high g-loading swirl created in the UCC. The shortened combustion length can decrease the entire engine in length and weight, but still provide the same and possibly better performance than the conventional axial combustor configuration. The UCC can also be coupled with the turning vanes before the turbine to further decrease engine length. Fig. 4 shows how the turning vanes and UCC may possibly be integrated.

The compact circumferential configuration also opens the door for an inter-turbine burner (ITB), which makes a reheat cycle possible. In the past, reheat cycles have been typically used on ground-based gas turbine engines where space and weight are not critical. However, on an aircraft, space and weight have driven many design choices. An additional UCC can be coupled with the stator between the high and low pressure turbine

so that engine length will not increase. A reheat cycle makes a much more powerful engine of the same size as a conventional engine. The decrease in engine size for the same performance can make the engine lighter as well.

The UCC has been designed to use a cavity similar to the TVC as the primary combustion zone. In this way there is a more stable recirculation zone that can aid in a restart. Combusting fuel and air from the cavity are transported down the front wall and into the main flow and into the intermediate zone, which is similar to the TVC.

II.4 Thermodynamic Cycle

The addition of an ITB between the low and high pressure turbine would allow for a reheat cycle that could dramatically increase the amount of fuel or heat that can be added to the process. The UCC is a far superior choice as an ITB over the conventional combustor. The major concern with shortening a conventional combustor to meet this application is decreased residence time and latent combustion in the turbine, which can lead to decreased turbine blade life. However, the advantages of combustion in the turbine are tremendous and approach optimal transfer of energy from gas to blades. Liu and Sirignano completed a cycle analysis and found that a burner between the high and low pressure turbines has significant advantages. Most notably they found that a combustor with an ITB cycle can allow elimination or reduction in afterburner length and weight, and as a result, can reduce TSFC (Liu and Sirignano, 1999:1). It can also increase ST, which will allow greater thrust for the same engine cross section or the same thrust for a smaller cross section. Liu and Sirignano also found that TSFC increases and ST decreases with increasing Mach number at a slower rate with the ITB cycle (Liu and Sirignano, 1999:1). The ITB cycle can also operate at higher Mach numbers than the

conventional cycle and thereby increase the operating envelope. Specifically, the ITB cycle was shown to operate much better at supersonic speeds where the conventional cycle is weak. Figure 5 shows the T-s diagram for an engine cycle with and without an ITB. The corresponding diagram of engine station numbers is in Fig. 6. In Fig. 5 the area inside the line is directly related to the power generated by the cycle. The dashed line represents the conventional jet engine cycle with an afterburner. The afterburner will increase the thrust output of the engine, but since the combustion occurs at a lower pressure the cycle is very inefficient. Combustion of fuel and air at a higher pressure such as between the high and low pressure turbine results in a much more efficient cycle. The solid line indicates the ITB cycle. The energy equation shows the relationship between fuel mass flow and changes in temperature across the burner, which relates directly to ST and TSFC (Sirignano and Liu, 1999:2).

$$\frac{\dot{m}_{fb}}{\dot{m}_a} = \frac{C_p(T_{04} - T_{03})}{Q_R\eta_b - C_p T_{04}} \quad (2)$$

The temperature limit on turbine blades (T_{04}) will restrict the amount of heat that can be added to the system. However, an ITB allows much more heat because the heat can be dispersed between stages rather than being deposited entirely in the main burner.

The cycle analysis by Liu and Sirignano is briefly repeated here. The analysis illustrates the differences between the conventional and ITB burner concept. The following assumptions were made.

1. No air bleeding
2. Complete expansion
3. No auxiliary power take-off

4. Perfect gas and constant gas properties
5. Heating organized in the turbine burner to maintain constant stagnation temperature

II.4.1 Inlet and Diffuser

The compressor inlet and diffuser stagnation temperature and pressure can be found using the following equations denoted as station 2.

$$T_{02} = T_a \left(1 + \frac{\gamma - 1}{2} M^2 \right) \quad (3)$$

$$P_{02} = P_a \left(1 + \eta_d \left[\left(\frac{T_{02}}{T_a} \right) - 1 \right] M^2 \right)^{\frac{\gamma}{\gamma - 1}} \quad (4)$$

II.4.2 Compressor

The compressor (2-3) stagnation temperature and pressure ratios can be calculated using the following equations.

$$\frac{P_{03}}{P_{02}} = \pi_c \quad (5)$$

$$\frac{T_{03}}{T_{02}} = 1 + \left(\frac{1}{\eta_c} \right) \left(\pi_c^{\frac{\gamma - 1}{\gamma}} - 1 \right) \quad (6)$$

Power required to drive the compressor is given below.

$$P_c = \dot{m}_a C_p (T_{03} - T_{02}) \quad (7)$$

II.4.3 Main Burner

The main burner (3-4) energy relation for combustion if enthalpy is neglected is shown below.

$$\dot{m}_{fb} Q_R \eta_b = C_p T_{04} (\dot{m}_a + \dot{m}_{fb}) - C_p T_{03} \dot{m}_a \quad (8)$$

The total pressure loss can be calculated using the following relation.

$$P_{04} = \pi_b P_{03} \quad (9)$$

II.4.4 Conventional Turbine Configuration

In the conventional turbine configuration (4-5') without an ITB it is assumed there is no auxiliary power or friction taken from the engine. Therefore, turbine and compressor power will be equal giving the following power balance.

$$\dot{m}_t C_{pt} (T_{04} - T_{05'}) = \dot{m}_c C_{pc} (T_{03} - T_{02}) \quad (10)$$

Stagnation temperature and pressure ratios are calculated as follows.

$$\frac{T_{05'}}{T_{04}} = 1 - \frac{T_{03} - T_{02}}{T_{04}} \quad (11)$$

$$\frac{P_{05'}}{P_{04}} = \left[1 - \frac{1}{\eta_t} \left(1 - \frac{T_{05'}}{T_{04}} \right) \right]^{\frac{\gamma}{\gamma-1}} \quad (12)$$

II.4.5 Inter-Turbine Burner Configuration

The ITB (4-5) can replace the above calculations if chosen. The following relationship would be the new relationship for temperature ratio.

$$T_{05} = T_{04} \quad (13)$$

In the ITB configuration the total temperature will remain constant because the energy released from combustion does not increase the temperature of the gas. The energy is put directly into turbine work required to drive the compressor. This is possible because the gas is expanding through the rotor while the energy is being released. From this ideal condition the correct fuel mass flow rate can be calculated using the equation below.

$$\dot{m}_{fib} = \frac{P_t}{Q_R \eta_{ib}} \quad (14)$$

The average temperature (T_{av}) added to the flow from this amount of fuel can be estimated using the following equation if an estimated average Mach number (M_{av}) is 0.7.

$$T_{av} = \frac{T_{04}}{1 + \frac{\gamma-1}{2} M_{av}^2} \quad (15)$$

The change in entropy can also be calculated as follows.

$$s_5 - s_4 = \frac{\dot{m}_{fib} Q_R \eta_{tb}}{(\dot{m}_a + \dot{m}_{fb}) T_{av}} = \frac{P_t}{(\dot{m}_a + \dot{m}_{fb}) T_{av}} \quad (16)$$

The pressure ratio for the ITB configuration that takes stagnation pressure loss into account goes as follows.

$$\frac{P_{05}}{P_{04}} = e^{\frac{s_5 - s_4}{R}} \quad (17)$$

A stagnation pressure recovery factor (π_{tb}) is introduced to account for the complicated combustion dynamics.

$$\frac{P_{05}}{P_{04}} = \pi_{tb} e^{\frac{s_5 - s_4}{R}} \quad (18)$$

II.4.6 Afterburner

The pressure ratio and mass flows in the afterburner can be calculated for both the regular afterburner (5'-6') and reduced afterburner (5-6) for the ITB configuration.

$$\pi_{ab} = \frac{P_{05}}{P_{06}} \quad (19)$$

$$\frac{\dot{m}_{fab}}{\dot{m}_a + \dot{m}_{fb} + \dot{m}_{fib}} = \frac{C_p (T_{06} - T_{05})}{Q_R \eta_{ab} - C_p T_{06}} \quad (20)$$

II.4.7 Nozzle

Finally, the last component in the engine is the nozzle and it contains the following relationships for stagnation temperature and static pressure respectively.

$$T_{07} = T_{06} \quad (21)$$

$$P_7 = P_a \quad (22)$$

The flow exit velocity from the nozzle can also be calculated as follows.

$$u_e = \sqrt{2\eta_N C_p T_{06} \left[1 - \left(\frac{P_a}{P_{06}} \right)^{\frac{\gamma-1}{\gamma}} \right]} \quad (23)$$

All of the ITB variables at stations 5, 6, and 7 in the afterburner and nozzle can be replaced by the conventional turbine variables using the following stations 5', 6', and 7'.

II.4.8 Engine Performance and Analysis

The engine performance in the form of ST and TSFC can be calculated using the following relationships respectively (Liu and Sirignano, 2000:8).

$$ST = \frac{T}{\dot{m}_a} = \left(1 + \frac{\dot{m}_{fb}}{\dot{m}_a} + \frac{\dot{m}_{fib}}{\dot{m}_a} + \frac{\dot{m}_{fab}}{\dot{m}_a} \right) u_e - u \quad (24)$$

$$TSFC = \frac{\dot{m}_f}{T} = \frac{\dot{m}_{fb} + \dot{m}_{fib} + \dot{m}_{fab}}{ST \dot{m}_a} \quad (25)$$

According to Liu and Sirignano a turbofan single ITB configuration without afterburner shows a 20% increase in ST for only a 10% increase in TSFC over a regular cycle with no afterburner. However, an engine with a full afterburner increases TSFC by 50% while providing the 20% increase in ST. In addition, the single ITB configuration with the addition of a reduced afterburner also produced a higher ST with a lower TSFC compared

to a conventional engine with an afterburner. The performance gains are even greater for a 2-ITB cycle and increases steadily up to the continuous turbine burner (CTB) cycle. The 2-ITB specifically can increase ST by about 80% at Mach 1 with only a 10% increase in TSFC. The CTB cycle can increase ST by 120% with only a 15% increase in TSFC. However, the CTB requires burning inside the turbine, which at this time is technologically unfeasible due to material constraints. In addition, these cycles can operate over the entire range of Mach numbers from 0 to 2 while the conventional cycle will not operate above Mach 1.25 (Liu and Sirignano, 2000:8). These results provide the impetus for development of the UCC because it can be combined with turning vanes and fit between turbine stages without increasing engine length and weight. This will enable and ITB cycle for aircraft engines.

II.5 Centripetal Acceleration

Fuel and air are injected into the cavity of the UCC such that a swirling motion is created in a cavity around the main air flow. The highly accelerated gas has tremendous centripetal acceleration acting on it once it enters the cavity. The colder and heavier air and fuel droplets are forced toward the outer edge of the cavity forcing the hotter products occupying the outer edge toward the center and out the cavity. Several forces are acting on the air mass and fuel droplets. Buoyancy forces are also causing products to leave one area and move to another. The equation below shows a sum of the forces with a positive coordinate system pointing to the centerbody.

$$\Sigma F = ma_{centripetal} = \Delta Momentum = Buoyancy_{hot} - Buoyancy_{cold} - \frac{dP}{dr} \quad (26)$$

Additionally, the cavity mass flow is forcing matter to migrate toward the cavity exit.

The combination of these factors and centrifugal instabilities discussed later are increasing mixing and hence combustion efficiency. According to Lewis, g-loading up to about 200g is ineffective at improving flame propagation (Lewis, 1973:415). From 200g to 500g there is an area of transition, and from 500g to 3500g the flame speed can be approximated by the following equation (Lewis, 1973:418).

$$S_B = 1.25\sqrt{g} \quad (27)$$

Beyond 3500g the flame speed reverses and decreases with centripetal force. The optimal g-loading for combusting flow that can enhance flame speed and allow more heat added to the system is between 500g and 3500g. In this range flame drops that are tossed out beyond the flame front due to g-loading can drive the flame speed (Lewis, 1973:415). Combustion with fuel droplets occurs when the outer surface of the drop comes in contact with air. A sliver of fuel molecules evaporates off the droplet and combusts one layer at a time until the droplet disappears. When the fuel droplets are forced out into the air this process can occur more quickly. The g-loading in the cavity can be calculated through circumferential velocity measurements in the following equation.

$$g = \frac{U_\theta^2}{Rg_0} \quad (28)$$

From equation 27 flame speed is proportional to circumferential velocity.

II.6 Taylor Vortices

An important phenomenon of centrifugal instability known as Taylor vortices occurs in laminar and turbulent boundary layer flow. The UCC is subject to this instability as it has fluid flowing along a concave wall. The flow along this wall is very

similar to Taylor vortices. These vortices will enhance mixing. Fluid may be caught in one of several vortices that line up next to one another against the wall and rotate in opposite directions as they move in the same direction as the main stream flow (Sherman, 1990:491-501).

II.7 Analytical Model

The Navier-Stokes equations were simplified to conform to an analytical model for the cavity and main air mass flows. The momentum, continuity, species, and energy equations were used to set up these models. Boundary conditions were applied to these two situations and an attempt was made to couple them to form a solution. The model became too difficult to solve analytically, but should be explored in the future. Below are the basic formulations of these models under the stoichiometric condition.

II.7.1 Cavity Air Navier-Stokes Equations

The fluid flow, chemical activity, and energy transfer inside the cavity can be modeled using the Navier-Stokes equations to include the species, and energy equations. Some assumptions are made to tailor these equations to the cavity. The cavity is modeled as steady flow, axi-symmetric and incompressible with no axial velocity or gradients. The swirling nature of the UCC allows residence time to be 20 times greater than mixing time according to CFD results (Ehret, 2002:Ch 4). The cavity is therefore well mixed and may be considered to have a uniform temperature with Mach numbers well below 0.3. For this reason we may assume the flow in the cavity is incompressible except for the radial pressure gradient, which is very small (less than a percent). The geometry of the UCC lends itself to cylindrical coordinates. Below is the equation for r -direction momentum,

$$\rho \left(U_r \frac{\partial}{\partial r} U_r - \frac{U_\theta^2}{r} \right) = -\frac{\partial P}{\partial r} + \mu \left[\frac{\partial}{\partial r} \left[\frac{1}{r} \frac{\partial}{\partial r} (r U_r) \right] \right] \quad (29)$$

θ -direction momentum,

$$\rho \left(U_r \frac{\partial}{\partial r} U_\theta + \frac{U_\theta U_r}{r} \right) = \mu \left[\frac{\partial}{\partial r} \left[\frac{1}{r} \frac{\partial}{\partial r} (r U_\theta) \right] \right] \quad (30)$$

continuity,

$$\frac{\rho}{r} \frac{\partial}{\partial r} (r U_r) = 0 \quad (31)$$

species,

$$\rho \left(U_r \frac{\partial}{\partial r} Y_i \right) + \frac{\rho}{r} \frac{\partial}{\partial r} \left(-r D \frac{\partial}{\partial r} Y_i \right) = \omega_i \quad (32)$$

and energy where viscous dissipation and other minor effects have been neglected,

$$\rho C_p \left(U_r \frac{\partial}{\partial r} T \right) - \left(U_r \frac{\partial}{\partial r} P \right) = \lambda \left[\frac{1}{r} \frac{\partial}{\partial r} \left(r \frac{\partial}{\partial r} T \right) \right] - \left(\sum_{i=1}^N \omega_i \Delta h_f^o \right) \quad (33)$$

The boundary conditions consist of reactants in the form of fuel and air entering unmixed and uniformly at the outer circumference of the cavity. The temperature of the outer wall is assumed to be 533K, which is equal to that of the entering heated air. A no slip condition exists between the main and cavity flow. Also, the reactants are assumed to be completely combusted at the inner circumference of the cavity. Below is a table showing the boundary conditions and Fig. 7 shows the boundary locations.

Table 1: Cavity Flow Boundary Conditions

| | | | |
|-----------------|-------------|--------------------------------|--|
| $r = R_{inner}$ | $T = 1800K$ | $Y_F = 0$ $Y_O = 0$ | $U_r = U_r(main)$ $U_\theta = U_\theta(main)$ $U_z = U_z(main)$ |
| $r = R_{outer}$ | $T = 533K$ | $Y_F = 0.068$ $Y_O = 0.233$ | $U_r = U_{air} \sin(45)$ $U_\theta = U_{air} \cos(45)$ $U_z = 0$ |

II.7.2 Main Air Navier-Stokes Equations

The main air mass flow that passes inside the cavity region has similar Navier-Stokes equations with slight variations and different boundary conditions. Below is the r -direction momentum equation,

$$\rho \left(U_r \frac{\partial}{\partial r} U_r - \frac{U_\theta^2}{r} + U_z \frac{\partial}{\partial z} U_r \right) = -\frac{\partial}{\partial r} P + \mu \left[\frac{\partial}{\partial r} \left[\frac{1}{r} \frac{\partial}{\partial r} (r U_r) \right] + \frac{\partial^2}{\partial z^2} U_r \right] \quad (34)$$

The θ -direction momentum equation,

$$\rho \left(U_r \frac{\partial}{\partial r} U_\theta + \frac{U_\theta U_r}{r} + U_z \frac{\partial}{\partial z} U_\theta \right) = \mu \left[\frac{\partial}{\partial r} \left[\frac{1}{r} \frac{\partial}{\partial r} (r U_\theta) \right] + \frac{\partial^2}{\partial z^2} U_\theta \right] \quad (35)$$

The z -direction momentum equation,

$$\rho U_z \frac{\partial}{\partial z} U_z = \mu \left[\frac{1}{r} \frac{\partial}{\partial r} \left(r \frac{\partial}{\partial r} U_z \right) + \frac{\partial^2}{\partial z^2} U_z \right] \quad (36)$$

continuity,

$$\frac{\rho}{r} \frac{\partial}{\partial r} (r U_r) + \rho \left(\frac{\partial}{\partial z} U_z \right) = 0 \quad (37)$$

species,

$$\rho \left(U_r \frac{\partial}{\partial r} Y_i \right) + \frac{\rho}{r} \frac{\partial}{\partial r} \left(-rD \frac{\partial}{\partial r} Y_i \right) = \omega_i \quad (38)$$

and energy where viscous dissipation and other minor effects are neglected,

$$\rho C_p \left(U_r \frac{\partial}{\partial r} T \right) = \lambda \left[\frac{1}{r} \frac{\partial}{\partial r} \left(r \frac{\partial}{\partial r} T \right) + \frac{\partial^2}{\partial z^2} T \right] - \left(\sum_{i=1}^N \omega_i \Delta h_f^o \right) \quad (39)$$

The products are assumed to be completely combusted at the outer edge of the main flow where it meets the cavity flow. The pressures and temperatures are equal, and there is a no-slip condition at the interface between the cavity and main flow. Finally, there is cavity air mass entering the main flow area and exiting the exhaust tube. There are products from combustion entering at the perimeter, which also exit the rear to the exhaust tube. Below is a table of the boundary conditions where R_{outer} is the same as R_{inner} from the cavity.

Table 2: Main Flow Boundary Conditions

| | | | | |
|--------------------------|----------------------|-------------|----------------------------|---|
| Main Flow Entrance | $r = R_{outer}$ | $T = 1800K$ | $Y_F = 0$ $Y_O = 0.233$ | $U_r = U_r(cavity)$ $U_\theta = U_\theta(cavity)$ $U_z = U_z(cavity)$ |
| | $r = R_{centerbody}$ | $T = 533K$ | $Y_F = 0$ $Y_O = 0.233$ | $U_r = 0$ $U_\theta = 0$ $U_z = 0$ |
| Main Flow Exit | $r = R_{outer}$ | $T = 1800K$ | $Y_F = 0$ $Y_O = 0.233$ | $U_r = U_r(cavity)$ $U_\theta = U_\theta(cavity)$ $U_z = U_z(cavity)$ |
| | $r = R_{centerbody}$ | $T = 533K$ | $Y_F = 0$ $Y_O = 0.233$ | $U_r = 0$ $U_\theta = 0$ $U_z = 0$ |

II.8 Laser Doppler Velocimetry

Laser Doppler Velocimetry uses the Differential Doppler technique to measure fluid velocities by injecting micron sized particles into the flow and measuring reflected flashes from laser light off these particles. To capture velocity two beams must cross at a point in the flow. Velocity in only one direction can be obtained with two beams.

Additional beam sets must be included to capture more directions. Figure 8 shows the laser set up for forward scatter LDV in relation to the fluid flow. A laser directs light into a beam splitter to create two beams. These two beams go through a convex lens that forces them to cross in the flow field. Scattered light from these beams due to collisions

with particles in the flow are captured with another convex lens that directs the light into a photo detector. This data is then sent to the processor to be analyzed.

According to Drain, micron sized particle (artificial seed) motion represent the fluid flow very accurately due to high drag to inertia ratio (Drain, 1980:191). A sufficient data rate of reflected Doppler probe frequency will be achieved when the concentration of these small particles is at least 10^{10} particles/m³. The light may also be reflected by particles that are already in the fluid such as soot or fuel droplets (Drain, 1980:191). However, these larger particles may not faithfully follow the flow due to their larger size and inertia.

The table below from Drain describes some of the factors involved with choosing the differential Doppler technique (Drain, 1980:5).

Table 3: LDV Advantages and Disadvantages

| Advantages | Disadvantages |
|---|---|
| Does not disturb the flow | Medium must be transparent |
| High Spatial resolution | Needs scattering particles: artificial seeding may be necessary |
| Fast response | Optical access required: windows may have to be installed |
| Response linear and easily calibrated | Expensive signal processing equipment may be required in difficult situations where the signal to noise ratio is poor |
| Directional discrimination possible | Not well suited for measurements of total flow as this requires a tedious integration over a cross section |
| Operation not usually seriously affected by temperature | |

II.8.1 Fringe Pattern and Speed Measurement

A laser beam is split into two equally separate beams that are crossed in the fluid flow. The fluid should be moving parallel to the plane of the crossed beams. A diagram

of the fringe pattern is shown in Fig. 9. At the point where the beams cross an interference fringe pattern is created. The high intensity areas are separated by a distance (S). A photo detector can capture light scattered by the particles as they pass through the high intensity areas and measure frequency (f). The angle between the two beams is α and the distance between fringes is shown here where λ is the wavelength of laser light (Drain, 1980:10).

$$S = \frac{\lambda}{2 \sin\left(\frac{\alpha}{2}\right)} \quad (40)$$

A seed particle that passes through the fringe pattern at a right angle will return the most accurate velocity measurement. Using distance between fringes and flash frequency the receiver is able to calculate speed. Another set of beams at a different wavelength and rotated 90 deg from the first two beams can create a fringe pattern in the same location, but perpendicular to the first set. This allows for calculations of flow speeds in an additional dimension. The following equation is used to determine speed of particles in the flow.

$$V = fS \quad (41)$$

II.8.2 Frequency Shifting

The differential Doppler technique can measure speed, but frequency shifting is required to determine a direction of the flow that will reveal velocity. Velocity is composed of speed and direction and only speed can be calculated without a frequency shift. A slight difference in frequency between laser beams is needed to cause the fringes to move in one direction. Moving the fringes in one direction makes it possible to

determine what direction a particle is moving. Fringe speed must always be faster than the particle speed for an accurate direction of movement and speed determination. When the frequency of flashes is greater than the frequency shift, the overall flow direction can be estimated to be in the opposite direction with respect to the fringes. However, when the frequency is below the shift frequency the flow is moving in the same direction as the fringes. Figure 10 is a diagram of the shift where in the shifted graph a particle with zero velocity will have a specific frequency and any frequencies below are negative velocities and above are positive velocities. A general knowledge of the flow speed must be known to use this technique. When the fringe direction is known the flow direction is also known and velocity is revealed. The following equation shows how to calculate fringe velocity (Drain, 1980:165).

$$V_f = \frac{\Delta \nu \lambda}{2 \sin\left(\frac{\alpha}{2}\right)} \quad (42)$$

Where $\Delta \nu$ is the imposed frequency shift.

II.8.3 Lasers and Optics

The LDV method is based on laser light in or near the visible region. The ultra-violet and infra-red regions may also be included. This puts the light frequencies in approximately the 10^{12} to 10^{16} hertz region. Electromagnetic light involves fluctuations of both electric and magnetic fields, but optical properties are primarily determined by the high frequency dielectric constant and electrical conductivity. A light wave at a specific point in an electric field will vary sinusoidally. One full cycle of a wave

determines the wavelength (λ). The product of these components is the equation for the speed of light given below (Drain, 1980:9).

$$c = \nu\lambda \quad (43)$$

The velocity of light also depends on the medium it is passing through. The speed of light in a vacuum is denoted c_o (2.99776e8 m/s in a vacuum) and the equation below shows how the speed of light is altered by the refractive index (μ) (Drain, 1980:9).

$$c = \frac{c_o}{\mu} \quad (44)$$

II.8.4 Seeding

Seed is necessary to provide the particles in the flow that will reflect laser light. There are two types of seeding called natural and artificial. In this research artificial seeding was used to enhance the natural seed of soot particles and fuel droplets. A micron sized ceramic seed powder of magnesium oxide (MgO) was used in a fluidized bed generator to inject the particles into the combustion chamber. Pressurized air blowing through a fluidized bed of seed allows the seed to become entrained in the gas and sent into the combustion zone. Achieving uniformity of the seed in the test section can be very difficult (Drain, 1980:191).

II.8.5 Velocity Biasing

Velocity biasing is a source of error in the use of Doppler signals to calculate turbulent flow velocities. It would be incorrect to weigh all particles that pass through the test section equally. This is due to the fact that particles moving faster have more influence because more of them can get through the test section than slow particles in a given data collection period. For high turbulence intensities the error can be very large

and a correction is important (Drain, 1980:136). It is essential for counter instruments to measure residence time as well as Doppler frequency to get a more accurate velocity average. The mean density of particles in the fluid is roughly independent of velocity, which means the average fraction of time a particle is present in a given scattering volume is also independent of velocity. This allows the probability distribution of velocity to be measured by the total time for which the Doppler signals in a specific frequency range are present. Therefore, the velocity values should be weighted with their transit residence times. The correct calculation for mean velocity is given below where τ is residence time.

$$\bar{u} = \frac{\sum_n u_n \tau_n}{\sum_n \tau_n} \quad (45)$$

The probability distribution function is given by the following equation (Drain, 1980:137).

$$P(u)du = \frac{\sum_{n(u)} \tau_n(u)}{\sum_n \tau_n} \quad (46)$$

II.9 Combustion

Combustion efficiency determination is essential for analyzing combustor performance. Emission results reveal important information about the nature of the chemical reactions going on in the combustor. The chemical products are a result of the chemical reaction between the fuel and air mixture injected into the combustor. The temperature, pressure, fuel composition, mixing, and residence time in the combustor determine what products will be released to the atmosphere. The world is becoming

more environmentally conscious, and emissions of all types from gas turbine engines are being examined closely and are becoming more tightly regulated.

An emissions index (EI) is often used to compare different combustors. This is calculated as mass of a pollutant in grams over mass of fuel in kilograms as in the equation below.

$$EI = \frac{g_{\text{pollutant}}}{kg_{\text{fuel}}} \quad (47)$$

Pollutant levels are directly related to temperature, time, and fuel concentration (Lefebvre, 1999:317). The method of combustion, such as deflagration or detonation, and the rate of reaction dictate how quickly the reactants are consumed. Only deflagration needs to be considered in the UCC. There are several pollutants that are most notable in the exhaust of a gas turbine engine. The unburned hydrocarbons (UHC), carbon monoxide (CO), nitric oxides (NO_x), and soot are the most harmful to the environment and people. Concentrations of CO and UHC are usually highest at low power conditions and lowest at increased power. Concentrations of NO_x and soot are typically least at low power conditions and greatest at high power conditions. The UCC will minimize the amount of NO_x produced during the combustion process through control of residence time in a short axial distance. Through enhanced mixing from g-loading a more complete combustion can be achieved to reduce harmful emissions such as CO and UHCs.

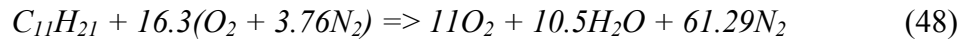
II.9.1 Deflagration

The UCC produces a turbulent non-premixed deflagrating flame whose reaction rate varies with g-loading. The deflagration typically process takes less than 1 ms at

atmospheric pressure to complete 80% of the reaction. The flame propagates through the unburned mixture similar to a diffusion flame that is expanding into the air due to an excess of fuel (Glassman, 1996:267-272). The burned gases are much higher in temperature.

II.9.2 Chemical Reaction

The reaction that occurs with the fuel and air can be represented in a balanced chemical equation. The fuel used in the UCC experiment is JP8, which is a relatively heavy fuel that goes as $C_{11}H_{21}$. The following equation represents the reaction of one mole of fuel with air.



Completeness of this reaction is a function of sufficient residence time and stoichiometry.

If $\phi > 1$ there will not be a complete combustion reaction due to lack of oxygen. Gas turbine engines with conventional combustors run lean overall, which means there is always enough air for the fuel being added in the combustor. The UCC operates very similar to the conventional combustor in this respect.

II.9.3 Reaction Rate

The rate of a global reaction for fuel F can be written as follows.

$$\frac{d[F]}{dt} = -K[F]^a [O]^b \quad (49)$$

The brackets around F and O represent the concentration of each component and the exponents (a and b) are empirically derived reaction orders. The factor K follows Arrhenius' law of reaction rate as shown below (Kanury, 1975:27-29).

$$K = Ae^{-\frac{E}{RT}} \quad (50)$$

Where A is a pre-exponential factor indicating the number of collisions between molecules called the frequency factor and the orientation of the collisions known as the steric factor, E is the activation energy, R is the gas constant and T is temperature. The larger K value will drive a faster reaction rate. Higher temperatures can increase K , which will aid in complete combustion of CO and UHC but will increase NO_x emissions.

II.9.4 Carbon Monoxide

There are three main causes of high CO levels. High levels can come from inadequate burning rates in the primary combustion zone, which can be caused by a low fuel to air ratio or insufficient residence time. Also, inadequate fuel and air mixing can prevent complete combustion and leave pockets of CO that can not reach more oxygen to become CO₂. Finally, quenching of post flame products by entrainment into the liner wall-cooling air can leave many CO molecules. When high temperatures are present (>1000K) the following reaction is fast over a broad temperature range (Glassman, 1996:72-75).



II.9.5 Unburned Hydrocarbons

High concentrations of UHC are generally driven by fuel that exits the combustor in the form of drops or vapor. They can also be products of thermal degradation of the parent fuel into lower molecular weight species. This is usually the result of low burn rates and poor fuel atomization by the injectors. The same factors that affect CO emissions also generally affect UHC emissions (Lefebvre, 1999:320).

II.9.6 Soot

Soot (carbonaceous hydrocarbon) is caused by small particles in fuel-rich regions of the combustion process that are unable to break free to combine with oxygen. Pressure, fuel type, and fuel atomization all play a roll in smoke and soot production. High pressures are associated with more soot production because fuel tends to concentrate in areas just downstream of the fuel nozzle, cone spray angle is decreased, and fuel drop size is increased. The combination of viscosity and volatility can affect droplet size, penetration, and evaporation. Correct fuel atomization is important to reduce soot production because the smaller a fuel droplet the easier it can be evaporated and combusted with the incoming flame. Rink and Lefebvre showed that by decreasing fuel droplet size from 110 to 30 μ m the soot concentration is cut in half. However, if the droplets do not have enough mass to penetrate the flame then poor mixing can actually increase the number of soot particles (Lefebvre, 1999:321-323). A delicate balancing act must be performed with these factors to achieve minimum soot emission. The enhanced mixing provided by the UCC can help reduce soot production.

II.9.7 Nitrogen Oxides

Concentrations of NO and NO₂ can be produced by 4 mechanisms called thermal NO_x, Prompt NO_x, fuel NO_x, and Nitrous Oxide Mechanism. Thermal or Zeldovich NO_x is produced when atmospheric nitrogen is oxidized at higher temperatures usually above 1850 K. The reaction usually follows the Zeldovich mechanism:





NO production usually peaks at stoichiometric conditions where temperature is also high. High flame and air temperatures both contribute to an increase in NO_x. High temperatures are desirable to increase reaction rates, produce more power and increase thermal efficiency. However, if low NO_x are desired the combustor can not operate at peak temperature. A rich-burn, quick-quench, lean-burn (RQL) combustor can provide a path around this situation. Fuel burned in the primary zone has a high equivalence ratio and is generally at a lower temperature. Then, combustion must cease prior to reaching an equivalence ratio of one where temperatures are highest. Finally, a burn is done in the pre-dilution zone when the equivalence ratio drops well below one and the temperatures are again low (Lefebvre, 1999:324-330).

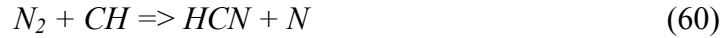
There are certain Nitrous Oxide Mechanisms that create NO_x. The formation begins with the following reaction.



Then, N₂O becomes NO in the following reactions.



NO sometimes occurs early in the combustion process, which is denoted as the Prompt NO mechanism. The following reaction occurs in lean-premixed conditions where HCN finally becomes NO.



There is very little data on this mechanism, but pressure may play a role because prompt NO_x production can be significant in lean-premixed combustion (Lefebvre, 1999:321-323).

Finally, the type of fuel used may contain higher amounts of organically-bonded nitrogen. Light distillate fuels contain 0.06% nitrogen where heavy distillates can contain as much as 1.8% nitrogen. Fuel NO can be a very significant contributor to the total amount of NO_x emitted. For a fuel such as methane which has no fuel NO the NO_x production can be broken down as, 60% thermal NO, 10% nitrous oxide mechanism, and 30% prompt NO when temperatures were around 1900 K. As temperature and equivalence ratio drop to 1500 K and 0.6 respectively the portions change to 5% thermal, 30% nitrous oxide, and 65% prompt. When equivalence ratios are at the lowest from 0.5 to 0.6 the most significant source is due to the nitrous oxide mechanism. Once NO is released into the atmosphere it eventually combines with oxygen and ultraviolet light in the atmosphere to become NO₂ to create the brown haze that is often visible over large cities (Lefebvre, 1999:321-323)

III Experimental Configuration

III.1 Ultra Compact Combustor Setup

The experimental ultra compact combustor is instrumented to observe combustor flow and the emissions associated with the combustion process. The axi-symmetric combustor is made of 316-series stainless steel and is equipped with main and cavity air supply where the main air inlet has a diameter of 3 inches. It has taps for fuel injectors and pressure, temperature, and emissions probes. The main parts of the combustor are the centerbody, liner ring, pressure ring, mounting flange, quartz window, and exhaust tube. Figures 3 and 11 show a diagram of the combustor configuration with all parts labeled.

III.1.1 Centerbody

The centerbody simulates the engine core. It is cylindrical in shape and has a bullet nose at the inlet. Toward the exit it gradually comes to a sharp point in the exhaust section of the combustor. A 7 degree taper to the point is used to prevent separation of the flow. It has a constant diameter of 2.25 inches through the combustion section, which allows for an annulus of 0.375 inches between centerbody and cavity entrance. There are 6 struts each 1.875 inches long and 0.25 inches wide evenly spaced around the centerbody. They extend outward to hold the centerbody in place and are flush with the cavity entrance. They also provide a low pressure zone in the main flow for mass transport from the cavity into the main flow.

III.1.2 Liner Ring

The liner ring shown in Fig. 12 provides the entrance of air and fuel into the combustion cavity. It is 4.63 and 5.5 inches at the inner and outer diameter respectively.

The inner diameter defines the outer wall of the combustion cavity. The ring is 1 inch in axial length, which is the same depth as the combustion cavity. There are 6 fuel injectors centered axially and evenly spaced around the ring. There are also 12 pairs of 4 air holes of 0.2 inches in diameter evenly spaced between the fuel injectors. They are angled 45 deg to a radial and are in pairs with respect to axial depth at 0.25 and 0.75 inches respectively. There are pressure and thermocouple taps as well as a hole for the torch igniter.

III.1.3 Pressure Ring

The pressure ring gives the fuel injectors and air supply a mounting location. The mounting taps for each injector entering the liner ring also has a corresponding tap in the pressure ring. The pressure ring also creates a plenum between the two rings for air entering the combustor. There are four air taps 90 deg apart to provide the pressure to this area. It has an inner and outer diameter of 6.375 and 6.625 inches respectively with a 1 inch depth once it is seated in the flange.

III.1.4 Mounting Flange

The mounting flange shown in Fig. 11 provides the front (upstream) wall of the combustion cavity and pressurized area and all other components are mounted to it. It is attached directly to the main air manifold, which holds it in place.

III.1.5 Quartz Window

The quartz window provides the rear (downstream) wall for the combustion cavity and pressurized area. It also allows the laser beam access to the test section for gathering velocity measurement data. Figure 13 shows a picture of one of the quartz windows after testing. A significant amount of soot is collected on the surface and a

small area where the laser made penetration is shown. It is slightly smaller in diameter than the pressure ring so that it can fit just inside at the edges. High temperature silicone rated at 644K is used to seal the air around the edge between the pressure ring and quartz window.

III.1.6 Exhaust System

The exhaust tube shown in Fig. 11 consists of a quartz tube that is 0.25 inches thick and 3.25 inches in diameter and is placed over the taper section of the centerbody. A steel ring with pressure tap and thermocouples attaches to the end of the tube and three steel rods with springs to allow expansion bolt the assembly to the mounting flange. An emission probe is placed just inside the end of the exhaust tube. This probe is temperature regulated to 436K with a heated oil system. This prevents both damage to the probe and condensation of exhaust gases within the probe. The collected gas is transported to the control room where they are measured by various gas analyzers. Concentrations of CO, CO₂, NO_x, O₂, and UHC are measured.

III.2 Laser Setup

The laser assembly includes a Coherent Innova 300C argon ion laser, TSI Colorburst Multicolor Beam Separator model 9201, TSI Color Link Plus Multicolor Receiver model 9230, Probe model 9253-350, IFA – 755 Digital Burst Correlator, and TSI data collection software. The laser is pointed directly into the beam separator, which separates, shifts and transmits all laser light through fiber optic cables to the probe. The probe projects the laser onto a flat mirror and into the test section. It also receives light flashes from the fringes in the test section so they can be processed into velocity data.

The angle α between the beams is 7.9 deg. The blue (488 nm) and green (514.5 nm) beams were used for the circumferential and radial components respectively. There were 24.2 fringes in the test section and the blue and green beam spacing was 3.54 and 3.73 μ respectively. The system also has a resolution of 0.05% and the blue and green test volumes were 7.16e-3 mm³ and 8.42e-3 mm³ respectively.

The laser requires water for the cooling system so hose lines connect the laser power unit to the building cooling water system and return water lines. A small electric water pump and filter are in series with the incoming water because other tests in the building can bring water pressure down below the laser power unit tolerances. A pressure regulator protects the system from pressure spikes.

The seeding system consists of a ceramic based micron sized powder blown through a 0.25 inch tube into the combustor using shop air and a small seed puffing device. The receiver will also capture flashes from soot particles and fuel droplets. In some cases the application of seed was not necessary for this reason.

III.3 Data Collection Facilities

All data except LDV information is collected through the control room computer, which uses software to process the information from emissions, pressure, and thermocouples. Pressure taps and thermocouples are located at various points on the UCC and connect directly to the test stand. Figure 14 shows a diagram of this setup. This information is hooked directly into the data center in the control room. The room can supply up to 0.453 kg/s of air to the test stand. The air is split into a main air supply and two smaller air supplies, one of which provides air to the cavity. The room can

provide air heated up to 533K. Two different fuel systems provide flow up to 0.0378 kg/s flow rate at 27.22 atm from a fuel farm located outside the building.

III.4 NO_x Measurements

Levels of NO and NO₂ are measured using the ECO Physics CLD 700 EL ht system, which has a two channel chemiluminescence nitric oxide analyzer. The hot gases go directly into the unit and are reduced below atmospheric pressure to prevent condensation from causing inaccuracies in the sampling process. A motorized bypass system reduces errors due to pressure variation (Ehret, 2002: 41-44).

III.5 Hydrocarbon Measurements

Unburned hydrocarbon concentrations are measured using a Beckman Model 402 Hydrocarbon analyzer. The machine imparts an ionization using a hydrogen flame to detect hydrocarbon atoms. When a hydrocarbon molecule comes through the flame it is ionized by the intense heat. An electrode near the flame can measure the small ion current. The amount of current represents the number of carbon atoms in a hydrocarbon and the current is converted into a voltage so that it can be measured (Ehret, 2002: 41-44).

III.6 Carbon Monoxide and Carbon Dioxide Measurements

Carbon Monoxide levels are calculated using the California Analytical Instruments Model ZRF. It is a non-dispersive infrared analyzer that uses a sensitive mass flow detector. A single beam is emitted from a source and is spliced in a rotating, single-point chopper cycling at 9 Hz. The beam is split into two separate beams that pass through a sample cell and a reference cell respectively. The sample cell contains the infrared absorbing components and the reference cell contains a non-absorbing gas. Two

infrared beams fall simultaneously on the micro-flow detector, which converts an intensity differential to a change in resistance. One beam is attenuated by the sample while the other is untouched. The 9 Hz AC signal is then amplified and transformed to a linear 4 to 20 mA DC signal for an output. (Ehret, 2002: 41-44).

IV Results and Discussion

IV.1 Experiment and Models

LDV measurements were acquired and results were compared to a CFD model completed by Ehret. The operating conditions were arranged so the experimental and numerical results of these methods could be correlated. The velocity measurements from LDV and velocity calculations from CFD are compared against one another.

An analytical model of the UCC was also formed with simplified Navier-Stokes equations to include the species and energy equations. However, a successful solution was not obtained. For the analytical model, the UCC was separated into regions for the cavity and main flows as discussed previously. The two regions were then coupled through boundary conditions.

Finally, a chemical kinetics program was used to model the emissions produced in the UCC (Kee and others, 2002:3.7). The CO emissions calculations from this model have been compared with the experimental CO emissions data.

IV.2 Velocity Measurements

Velocity measurements in the circumferential and radial directions were taken with the LDV setup. These measurements were taken at three different positions labeled A, B, and C. All three positions were located at 16 degrees downstream of a fuel injector. Position A was at 0.25 inches in from the quartz window and 0.3 inches toward the centerbody from the liner ring. Position B was located at 0.5 inches in from the quartz window and 0.3 inches from the liner ring. Position C was at 0.25 inches from the quartz window and 0.2 inches from the liner ring. Figure 15 shows a diagram of these positions. A range of cavity and main air mass flows were used to create a data table.

The table below shows the different test conditions and the positions these data points were taken. Some data points could not be recorded because the UCC would not run at the extreme conditions before blowing out.

Table 4: Test Matrix

| | | | | | | | |
|----------------------------------|------------------------------------|---------------|---------------|---------------|---------------|---------------|---------------|
| Main Air Mass flow (kg/s) | 0.1330 | A,B,C | A,B,C | A,B,C | A,B,C | A,B,C | B |
| | 0.1164 | A,B,C | A,B,C | A,B,C | A,B,C | A,B,C | |
| | 0.1035 | A,B,C | A,B,C | A,B,C | A,B,C | | |
| | 0.0937 | | A,B,C | A,B,C | | | |
| | 0.0832 | A,B,C | A,B,C | A,B,C | A,B,C | C | |
| | | 0.0224 | 0.0252 | 0.0289 | 0.0332 | 0.0370 | 0.0408 |
| | Cavity Air Mass Flow (kg/s) | | | | | | |

The CFD model by Ehret takes a 60 deg periodic wedge of the combustion cavity that accounts for four air jets and a single fuel injector. The steady state model was set up so that the mass at the exit of the wedge will enter the front to form a continuous cycle. This reduces process time and still simulates the conditions of a complete 360 deg model.

Data was extracted from the CFD results in two planes, which correspond with the data points taken using LDV. The first plane is aligned with the upstream holes and correlates with experimental positions A and C, which are in-line with the downstream holes. Position B lines up exactly with the plane taken in line with the fuel injector and correlates with the second CFD data plane. Variations in the CFD data is due to the probability density function set in the program to simulate actual measurements.

Figure 16 shows LDV data for position A in the U_θ (circumferential) and U_r (radial) directions. Positive in the circumferential direction is counter-clockwise and positive in the radial direction is toward the center. The coordinate system orientation was done this way to better match the data recording capability of the LDV equipment. Circumferential velocities ranged from 20-45 m/s and radial velocities ranged from 2-12 m/s. Figure 17 shows position C in the U_θ and U_r directions plotted against pressure drop (%dP/P). Circumferential velocities were 23-42 m/s and radial velocities were 3-7 m/s. This data was taken at stoichiometric conditions, mass flow of 22% cavity air, 78% main air and a pressure drop ranging from 1% to 4%. The numerical data taken in-line with the upstream holes from Ehret also fit these conditions and raw data plots for circumferential velocity of the 4% and 2% pressure drop scenarios are shown in Figs. 18 and 19 respectively. Circumferential velocities from the CFD model in the 4% pressure drop scenario ranged from 40-100 m/s and in the 2% pressure drop scenario ranged from 25-60 m/s. Mean radial velocities from CFD not shown in a graph were 15 m/s and 9 m/s in the 4% and 2% scenarios respectively. These velocity measurements agree quite well with the experimental results.

Figure 20 shows the U_θ and U_r velocity measurements with %dP/P for position B, which also fit the 22% cavity air split at stoichiometric conditions. The circumferential results ranged from 20-30 m/s and radial results were 7-10 m/s. This data corresponds to the plane in-line with the fuel injector in the CFD model. The CFD predicts the circumferential velocities (Figs. 21 and 22) in the range of 30-100 m/s and 27-60 m/s for the 4% and 2% pressure drops respectively. The mean radial velocities

were 8 m/s and 6 m/s for the 4% and 2% cases respectively. Again, the velocities agree quite well to the experimental results considering the conditions. The table below shows mean experimental and CFD velocities at each position for the 2% pressure drop case where the data was best correlated.

Table 5: Experimental and CFD Mean Velocities (Positions A, B, C)

| | Experimental | | CFD | |
|------------------------------|------------------|-------------|------------------|-------------|
| | U_θ (m/s) | U_r (m/s) | U_θ (m/s) | U_r (m/s) |
| Positions A and C (Air Jets) | 35 | 8 | 37 | 9 |
| Position B (Fuel Injectors) | 28 | 5 | 36 | 6 |

The velocity measurements taken with the LDV were also used to compare the effect from a range of cavity and main air mass flows. Figures 23 through 28 show the U_θ and U_r velocity measurements for positions A, B, and C respectively compared against the cavity mass flow. Main air mass flows for each point are noted on the charts as well. As expected, the angled flow allows variations in cavity air mass flow to have a direct effect on circumferential velocities. Circumferential velocities increase at about 1 m/s for each 0.001 kg/s of cavity air mass flow. The additional mass flow is also forcing air to exit the cavity (positive radial direction). Figures 29 through 34 show U_θ and U_r measurements for positions A, B, and C respectively against the main air mass flow with cavity air mass flows noted for each point. The main air has little effect on mean radial velocity as shown in Figs. 30, 32 and 34. This is expected because it is not acting directly on the flow in the cavity like the cavity air mass flow. Additionally, there is a

fair amount of scatter in the data. This is believed to be due to a portion of the velocity measurements being recorded on light scattered from unburned fuel particles. Fuel particles are larger than the micron sized artificial seed and will not follow the flow as faithfully. The fuel particles were also different sizes due to the different cavity air pressures. This would change the degree to which the particles are able to follow the flow and return various velocities.

Numerical calculations done by Ehret show that 20-30% of the main air is entrained in the cavity. Figure 35 shows the CFD plot of main air entrainment into the cavity. There is also little effect of main air mass flow on mean circumferential velocity according to the LDV measurements in Figs. 29, 31 and 33. This is expected because the main air mass flow is acting perpendicular to the circumferential direction. Flow turbulence in the radial and circumferential directions was also measured and is related to main air entrainment. The equation below shows the relation for Turbulence Intensity (TI).

$$TI\% = \frac{V_{std.dev.}}{V_{mean}} \times 100 \quad (61)$$

Turbulence Intensities are relatively high (40%-180%) in the radial direction. The high TI values are most likely due to main air entrainment into the cavity. Figures 36, 37, and 38 have TI using radial velocity plotted against main air mass flow for a range of cavity air mass flows. There is a general trend of decreasing TI in the radial direction with increasing cavity air mass flow. This means the higher mass flows are increasing the mean velocity while the standard deviation of velocity is either remaining constant or decreasing. Figures 39, 40, and 41 show TI using circumferential velocity plotted against

main air mass flow for a range of cavity air mass flows. The TI is much less (20%-60%) than in the radial direction indicating less impact in the circumferential direction due to main air entrainment. TI is also an indicator of enhanced mixing, however high (~100%) TI indicates large scale vortex shedding that could transport fuel and air out of the cavity before combustion occurs. Additionally, these shedding vortices can cause large vibrations and noise, which lead to engine damage. The UCC saw vibrations and created loud noise at all operating conditions, but the largest vibrations occurred at high main air mass flows. Combustors are typically very loud with large vibrations and the UCC is very similar to conventional combustors in this area.

A comparison of circumferential and radial velocities at the different positions can also be made. Figures 42, 43, 44 and 45 show both U_θ and U_r velocities for each position, where Figs. 42 and 44 are plotted against main air mass flow and Figs. 43 and 45 are plotted against cavity air mass flow. It is clear that positions A and C have higher circumferential velocities than position B. Circumferential velocities near the quartz window appear greater than in the center of the cavity. However, this is expected because positions A and C are in line with an air jet. CFD results also show a higher circumferential velocity average in-line with the air jets than with the fuel injectors as seen in Figs. 18 and 21 respectively. The enhancing effect of increased cavity air mass flow on both U_θ and U_r is also visible in Figs. 43 and 45.

IV.3 Combustion Efficiency

Combustion efficiency is a way to measure the quality of combustion in the cavity. Efficiency is impacted by changes in mixing and residence time. Flame speed can be enhanced by centripetal force effects (g-loading) as demonstrated by Lewis in

equation 27 (Lewis, 1973:418). Efficiency was calculated using the following equation (SAE ARP1533, 1996:16).

$$\eta_b = \left[1.00 - 10109 \frac{EI_{CO}}{H_C} - \frac{EI_{C_xH_y}}{1000} \right] 100 \quad (62)$$

CO and unburned hydrocarbons emissions will reduce the efficiency of the combustion process.

In the UCC increased g-loading also enhances flame speed and has a similar effect on mixing by reducing mixing time, which improves combustion efficiency. The goal of the UCC is to use the g-loading phenomenon to maintain complete combustion in a severely reduced axial length. The swirling nature of the UCC, which is caused by the cavity air mass flow at a 45 degree inlet angle, creates the g-loading needed to bring mixing to a heightened level. Figures 46, 47, and 48 show the LDV results between changes in cavity air mass flow and g-loading for positions A, B, and C respectively. Data at equivalence ratios from 0.8 to 1.5 are represented on each graph. Equivalence ratio appears to have very little effect on the results in any of the experiments. At each position there is a definite positive relationship that shows increased cavity air improves g-loading. Figure 49 shows the relationship between g-loading and combustion efficiency for position A and a range of equivalence ratios are also represented. Position A shows a very positive direct relationship between g-loading and combustion efficiency. As emissions were sampled from the aggregate exhaust at the exit of the combustor it is expected that the position in which velocity measurements were taken should not affect emissions measurements. For this reason all three positions are not plotted on the same graph, but results from the other positions are very similar.

Combustion efficiency also depends on residence time. The nature of Longwell Loading Parameter (LLP) is related to residence time. LLP is used instead of residence time because it can be used to compare different combustors and different operating conditions with one another. The equation for LLP is shown below (Anthenien and others, 2001:2).

$$LLP = \frac{VP^{1.75} e^{\frac{T}{300}}}{\dot{m}} \quad (63)$$

Figure 50 shows a plot of efficiency against LLP. The efficiency decreases with increasing LLP. The UCC has better efficiency with shorter residence times. At first this would seem counter-intuitive, but increasing mass flow will increase g-loading and mixing. However, more mass flow decreases residence time. These plots indicate that increased g-loading for better mixing has a more significant effect on efficiency than increasing residence time.

IV.4 CO Emissions

CO emissions are one indicator of complete combustion. The CO emissions data taken concurrent with LDV measurements show g-loading having little effect on CO emission index (EI). Figure 51 shows g-loading plotted against CO EI and scatter makes it difficult to determine the effect of g-loading. CO EI is not affected by position, but g-loading is calculated using velocity which is dependent on position. As with the efficiency results discussed earlier only position A is shown because the other positions cannot be plotted on the same graph, but their results are similar. During testing it was observed that the pressure inside the plenum was enough to slightly lift the quartz window from the UCC. When the window lifts off blow-out often occurs because the

volume of the cavity changes. This caused some data points to be inaccurate until the problem was corrected and those data points were thrown out of the results. CO EI was also plotted against LLP (residence time) in Figure 52. There is a definite decrease in CO EI as LLP increases. This is expected because longer residence time allows CO reactants to combine with other oxygen molecules to form CO₂. The cluster of data points above the main group were recorded at the far corners of the operating range. These points were run at a main air mass flow of 0.1330 kg/s and cavity air mass flow of 0.0224 kg/s. The high main air mass flow caused an increase in entrainment into the cavity and forced unburned fuel and CO into the exhaust stream. These points were taken to observe this effect and should not be weighted with the other recorded data points.

IV.4.1 Chemical Kinetics

A chemical kinetics program was used to create a model of the UCC to compare numerical emissions results with the experimental emissions measurements. The UCC was modeled according to the diagram in Fig. 53. The diagram describes how mass will move through the combustor. The program uses conditions at three different reactor positions to make calculations. The UCC is divided into three separate reactors that have their own inlet temperature, volume, mass flow rate, surface area, and heat of reaction values. These parameters were calculated using UCC dimensions and actual measurements taken during experimental testing. Six different sets of cavity and main air mass flow points were run through the program while holding equivalence ratio constant ($\phi = 1$) to create the results.

The first reactor is formulated after the cavity where mass flow of fuel and air enter and a total mass flow leaves to the second reactor. The second reactor is formed

after the main flow where air mass flow enters and 20% is released back into first reactor to simulate main air entrainment into the cavity. Finally, the second reactor empties mass flow into the third reactor, which is formed after the exhaust section. Just before the third reactor releases all mass flow into the atmosphere the emissions are calculated. The program models a premixed reactor and therefore will show far less CO EI than the experimental measurements because the UCC is similar to a partially stirred reactor with a plug flow reactor for the exhaust. A partially stirred model with a plug flow exhaust was attempted but was never able to converge. Figure 54 shows a plot of CO EI compared with LLP. The trend in the data is similar to those taken experimentally. The major difference being far less CO EI produced in the numerical simulation. Experimental data ranged from 1 to 8 in EI while numerical results showed 0.12 to 0.18. These calculations can serve as a goal for the UCC in future configurations.

IV.5 Error Analysis

Experimental error exists in the velocity, CO, and efficiency measurements. The LDV statistical error is calculated using the following equation (Boutier, 1991:5).

$$\bar{u} \pm \frac{Z\sqrt{u'^2}}{\sqrt{N}} \quad (64)$$

Where Z is 1.645 for 90% confidence, \bar{u} is mean velocity, $\sqrt{u'^2}$ is standard deviation of velocity, and N is the number of points (typically 3000-5000). Circumferential errors in velocity on average were 0.85% at a 90% confidence level and radial errors were 5.79% with 90% confidence. Error in turbulence intensity can be calculated using the following equation.

$$TI\% \pm \left(\frac{Z\sqrt{u'^2}}{\bar{u}\sqrt{2N}} \right) 100 \quad (65)$$

Errors in circumferential turbulence intensity on average were $\pm 0.65\%$ at 90% confidence and radial turbulence intensity errors were $\pm 4.7\%$ at 90% confidence. Errors in CO and efficiency were calculated using an error analysis program developed at Wright Patterson AFB (Heneghan and Frayne, 2000:2-9). Average errors in CO measurements were 5% and average errors in efficiency measurements were 0.05%.

IV.6 CFD Temperature Calculations

In Chapter 2 the argument was made that cold products are forced to the outer edge of the cavity due to centripetal acceleration. As the relatively cold products become warmer and as more reactants are forced into the volume they eventually exit the cavity as relatively hot products. Figures 55, 56, 57, and 58 are CFD contour plots of the 60 deg slice of the UCC from the rear view. These plots all represent the 22% cavity air configuration in-line with the air jets and in line with the fuel injectors at 2% and 4% pressure drops respectively. In each graph the highest temperatures (2000 K) are very near the exit of the cavity and the relatively cooler temperatures (1000 K) are close to the entrance or outer radius of the cavity. These plots support the hypothesis of g-loading in the cavity leading to separation of unburned reactants and burned products. Cold reactants are thrust into the center of the cavity by momentum and subsequently thrown to the outside from high g-loading. Then after becoming hot from reaction they are also carried toward the exit by buoyancy. This action greatly increases mixing inside the cavity and ultimately leads to higher combustion efficiencies. These plots support the g-

loading effect on combustion efficiency that was determined through the LDV experiments shown in Fig. 49.

IV.7 Analytical Analysis

An analytical model of the UCC was created to support the numerical and experimental findings. This model was divided into two separate regions. The two regions are cavity and main flow, which are linked by boundary conditions. The Navier-Stokes equations to include the species and energy equations were arranged using several assumptions for each region. A solution to the model has not been achieved and currently requires numerical analysis to solve. At this point CFD must be used to analyze flow characteristics inside the UCC.

IV.7.1 Cavity Flow

The following assumptions were made to simplify the Navier-Stokes equations.

Table 6: Cavity Flow Assumptions

| | | | | | | |
|--|---|--|--|--|--|--|
| $\frac{\partial}{\partial t} U_r = 0$ | $\frac{\partial}{\partial t} U_\theta = 0$ | $\frac{\partial}{\partial t} U_z = 0$ | $\frac{\partial}{\partial t} Y_i = 0$ | $\frac{\partial}{\partial t} T = 0$ | $\frac{\partial}{\partial t} P = 0$ | $\frac{\partial}{\partial t} \rho = 0$ |
| | | $U_z = 0$ | | | | |
| $\frac{\partial}{\partial \theta} U_r = 0$ | $\frac{\partial}{\partial \theta} U_\theta = 0$ | $\frac{\partial}{\partial \theta} U_z = 0$ | $\frac{\partial}{\partial \theta} Y_i = 0$ | $\frac{\partial}{\partial \theta} T = 0$ | $\frac{\partial}{\partial \theta} P = 0$ | |
| $\frac{\partial}{\partial z} U_r = 0$ | $\frac{\partial}{\partial z} U_\theta = 0$ | $\frac{\partial}{\partial z} U_z = 0$ | $\frac{\partial}{\partial z} Y_i = 0$ | $\frac{\partial}{\partial z} T = 0$ | $\frac{\partial}{\partial z} P = 0$ | |

Below is the momentum equation for the r and θ directions respectively.

$$\rho \left(U_r \frac{\partial}{\partial r} U_r - \frac{U_\theta^2}{r} \right) = -\frac{\partial P}{\partial r} + \mu \left[\frac{\partial}{\partial r} \left[\frac{1}{r} \frac{\partial}{\partial r} (r U_r) \right] \right] \quad (66)$$

$$\rho \left(U_r \frac{\partial}{\partial r} U_\theta + \frac{U_\theta U_r}{r} \right) = \mu \left[\frac{\partial}{\partial r} \left[\frac{1}{r} \frac{\partial}{\partial r} (r U_\theta) \right] \right] \quad (67)$$

Continuity,

$$\frac{\rho}{r} \frac{\partial}{\partial r} (r U_r) = 0 \quad (68)$$

Species,

$$\rho \left(U_r \frac{\partial}{\partial r} Y_i \right) + \frac{\rho}{r} \frac{\partial}{\partial r} \left(-r D \frac{\partial}{\partial r} Y_i \right) = \omega_i \quad (69)$$

Energy,

$$\rho C_p \left(U_r \frac{\partial}{\partial r} T \right) - \left(U_r \frac{\partial}{\partial r} P \right) = \lambda \left[\frac{1}{r} \frac{\partial}{\partial r} \left(r \frac{\partial}{\partial r} T \right) \right] - \left(\sum_{i=1}^N \omega_i \Delta h_f^o \right) \quad (70)$$

The variables are non-dimensionalized as shown below.

Table 7: Cavity Flow Non-Dimensionalization

| | | | | |
|--------------------------|------------------------------------|--------------------------|--------------------|--------------------|
| $U_r = U_R \mathbf{U}_r$ | $U_\theta = U_R \mathbf{U}_\theta$ | $U_z = U_R \mathbf{U}_z$ | $r = R \mathbf{r}$ | $z = R \mathbf{z}$ |
|--------------------------|------------------------------------|--------------------------|--------------------|--------------------|

The cavity is considered incompressible so the continuity equation is solved for U_r as follows.

$$\mathbf{U}_r = \frac{U_R R}{\mathbf{r}} \quad (71)$$

The cavity was determined to be incompressible because density and pressure changes in the radial direction are very small. In addition, because mixing time ($50 \mu s$) is 20 times

faster than reaction time (1 ms) we can assume that the temperature gradient in the radial direction is also very small (Ehret, 2002:Ch 2).

Through the Zeldovich formulation the species and energy equations are coupled to form the following equation.

$$\mathbf{U} \mathbf{r} \frac{\partial}{\partial \mathbf{r}} \xi = \frac{1}{Pe \mathbf{r}} \frac{\partial}{\partial \mathbf{r}} \left(\mathbf{r} \frac{\partial}{\partial \mathbf{r}} \xi \right) \quad (72)$$

With the continuity equation this differential equation is solved to reveal the solution in Appendix B. The boundary conditions are shown in the table below.

Table 8: Cavity Flow Similarity Boundary Conditions

| | | |
|--|--------------------------|-----------|
| Interface between cavity and main flow | $\mathbf{r} = R_{inner}$ | $\xi = 0$ |
| Outer wall of the cavity | $\mathbf{r} = R_{outer}$ | $\xi = 1$ |

The full derivation can be found in Appendix B.

IV.7.2 Main Flow

The following assumptions were made to simplify the Navier-Stokes equations.

Table 9: Main Flow Assumptions

| | | | | | | |
|--|---|--|--|--|--|--|
| $\frac{\partial}{\partial t} U_r = 0$ | $\frac{\partial}{\partial t} U_\theta = 0$ | $\frac{\partial}{\partial t} U_z = 0$ | $\frac{\partial}{\partial t} Y_i = 0$ | $\frac{\partial}{\partial t} T = 0$ | $\frac{\partial}{\partial t} P = 0$ | $\frac{\partial}{\partial t} \rho = 0$ |
| | | $\frac{\partial}{\partial r} U_z = 0$ | | | $\frac{\partial}{\partial r} P = 0$ | |
| $\frac{\partial}{\partial \theta} U_r = 0$ | $\frac{\partial}{\partial \theta} U_\theta = 0$ | $\frac{\partial}{\partial \theta} U_z = 0$ | $\frac{\partial}{\partial \theta} Y_i = 0$ | $\frac{\partial}{\partial \theta} T = 0$ | $\frac{\partial}{\partial \theta} P = 0$ | |
| $\frac{\partial}{\partial z} U_r = 0$ | $\frac{\partial}{\partial z} U_\theta = 0$ | | $\frac{\partial}{\partial z} Y_i = 0$ | | | |

Below is the momentum equation for the r, θ and z directions respectively.

$$\rho \left(U_r \frac{\partial}{\partial r} U_r - \frac{U_\theta^2}{r} + U_z \frac{\partial}{\partial z} U_r \right) = -\frac{\partial}{\partial r} P + \mu \left[\frac{\partial}{\partial r} \left[\frac{1}{r} \frac{\partial}{\partial r} (r U_r) \right] + \frac{\partial^2}{\partial z^2} U_r \right] \quad (73)$$

$$\rho \left(U_r \frac{\partial}{\partial r} U_\theta + \frac{U_\theta U_r}{r} + U_z \frac{\partial}{\partial z} U_\theta \right) = \mu \left[\frac{\partial}{\partial r} \left[\frac{1}{r} \frac{\partial}{\partial r} (r U_\theta) \right] + \frac{\partial^2}{\partial z^2} U_\theta \right] \quad (74)$$

$$\rho U_z \frac{\partial}{\partial z} U_z = \mu \left[\frac{1}{r} \frac{\partial}{\partial r} \left(r \frac{\partial}{\partial r} U_z \right) + \frac{\partial^2}{\partial z^2} U_z \right] - \frac{\partial}{\partial z} P \quad (75)$$

Continuity,

$$\frac{\rho}{r} \frac{\partial}{\partial r} (r U_r) + \rho \left(\frac{\partial}{\partial z} U_z \right) = 0 \quad (76)$$

Species,

$$\rho \left(U_r \frac{\partial}{\partial r} Y_i \right) + \frac{\rho}{r} \frac{\partial}{\partial r} \left(-r D \frac{\partial}{\partial r} Y_i \right) = \omega_i \quad (77)$$

Energy,

$$\rho C_p \left(U_r \frac{\partial T}{\partial r} \right) = \lambda \left[\frac{1}{r} \frac{\partial}{\partial r} \left(r \frac{\partial T}{\partial r} \right) + \frac{\partial^2}{\partial z^2} T \right] - \left(\sum_{i=1}^N \omega_i \Delta h_f^o \right) \quad (78)$$

The variables are non-dimensionalized as shown below.

Table 10: Main Flow Non-Dimensionalization

| | | | | |
|--------------------------|------------------------------------|--------------------------|--------------------|--------------------|
| $U_r = U_R \mathbf{U}_r$ | $U_\theta = U_R \mathbf{U}_\theta$ | $U_z = U_R \mathbf{U}_z$ | $r = R \mathbf{r}$ | $z = R \mathbf{z}$ |
|--------------------------|------------------------------------|--------------------------|--------------------|--------------------|

If the main flow is considered incompressible like the cavity flow a relation for U_r as a function of r and z may be obtained. Through the use of the Zeldovich formulation the species and energy equations are coupled to form the following equation.

$$\mathbf{U}_r \frac{\partial \xi}{\partial \mathbf{r}} = \frac{1}{Pe \mathbf{r}} \frac{\partial}{\partial \mathbf{r}} \left(\mathbf{r} \frac{\partial \xi}{\partial \mathbf{r}} \right) \quad (79)$$

The boundary conditions for the main flow are shown in the table below.

Table 11: Main Flow Similarity Boundary Conditions

| | | | |
|--------------------|--|-------------------------------|-----------|
| Main Flow Entrance | Surface of the centerbody | $\mathbf{r} = R_{centerbody}$ | $\xi = 1$ |
| | Interface between cavity and main flow | $\mathbf{r} = R_{outer}$ | $\xi = 0$ |
| Main Flow Exit | Surface of the centerbody | $\mathbf{r} = R_{centerbody}$ | $\xi = 1$ |
| | Interface between cavity and main flow | $\mathbf{r} = R_{outer}$ | $\xi = 0$ |

There is a fundamental problem with the approach for the cavity and main flow derivation. The UCC does not act like a diffusion flame because the cavity is a partially premixed region. Therefore, the Zeldovich formulation would not work to solve the equations and the cavity and main flow models could not be successfully coupled through boundary conditions to form a solution. Another method should be investigated to solve

this problem when time permits. The full derivation to this point can be found in Appendix B.

V Conclusion

V.1 Conclusions

UCC applications are far reaching in aviation where thrust to weight ratio is crucial. Decreased engine weight from shorter axial length and power gain through the addition of one or more ITBs make the UCC an attractive option in any type of aircraft engine. The UCC has many advantages over a conventional combustor and can perform as well or better. Many combinations of improvements can be made through use of the UCC. A more powerful engine of the same size can be fabricated for use in more demanding applications. A smaller engine can be designed to perform the same functions as a larger engine. Finally, an engine can be designed for greater MTBM through lower temperatures on turbine blades.

The data gathered through LDV testing and CFD calculations have shown exceptional performance in terms of efficiency. Although the UCC is atmospheric, values over 99.6% efficiency have been recorded when high g-loading is present. This supports the efforts of high swirl to enhance mixing in a short axial length. Combustion efficiencies continued to increase up through the g-loading range (1000g-4500g).

LDV and CFD data have proven to match very close at the 2% cavity pressure drop condition. The UCC experimental data showed mean circumferential velocities in-line with air jets of 35 m/s counterclockwise and mean radial velocities of 8 m/s toward the centerbody. Mean velocities of 28 m/s and 5 m/s were measured at the fuel injector plane for the circumferential and radial directions respectively. These velocities showed a very direct relationship to changes in cavity air mass flows, but showed no definite relationship with main air mass flows. The circumferential velocities were used to

calculate g-loading values from 1000g to 4500g. These experimental results support CFD allowing the loop to be closed on velocity inside the UCC. The mean CFD circumferential velocity in the air jet plane was 37 m/s and mean radial velocity was 9 m/s. In the fuel injector plane circumferential and radial velocities of 36 m/s and 6 m/s respectively were calculated. These velocities are well within 20% of the velocities measured using the LDV system and provide great confidence in the CFD model for design and analysis of future UCC configurations. Additionally, turbulence intensities in the circumferential and radial directions have been measured at 30% and 122% respectively. These numbers support the 20-30% entrainment predicted by CFD. As a vortex is shed from the cavity the main air mass must fill the space. The UCC will most likely be a trapped vortex in the future to eliminate vortex shedding and the possibility of CO and unburned fuel particles from escaping the cavity. However, high turbulence intensities can also be associated with improved mixing, which has a positive effect on combustion efficiency. A balance between these factors needs to be discovered before steps can be made toward use in a gas turbine engine.

The UCC concept can be useful in any application where a gas turbine engine is involved. However, the UCC would be most effective where more power in a small unit is required. Unmanned Air Vehicles (UAV) and missiles are prime candidates for the UCC. These aircraft are becoming more compact to provide better stealth, maneuverability, and loading onto other aircraft. However, they still require an excess of power and speed to perform their mission. The UCC can also be used in large commercial and military aircraft where better T/W can increase fuel efficiency through a reduction in engine size and weight. The structure to mount and support these engines

would also be reduced with a smaller engine and further decrease aircraft weight. The drag associated with a larger engine can also be mitigated with the decrease in cross sectional area. Engine blade MTBM can also be reduced in military and commercial applications where reduction in maintenance is most desirable. Engine turbine blades must be pulled from aircraft and refurbished due to high temperatures and damaging combustion particles. If the energy put into these engines is distributed to more stages through the use of an ITB the MTBM for turbines could be increased. Costs associated with maintenance could be reduced dramatically while increasing the availability of assets at the same time.

V.2 UCC Future

The UCC is a small but crucial step toward compact, more efficient gas turbine engines. Increasing environmental awareness and decreasing oil reserves make improvements such as the UCC essential. The UCC can be used in any type of gas turbine, but will be most useful in high performance applications. The Air Force has numerous platforms where this technology can be integrated to improve performance. Virtually every aircraft could eventually have an engine with a UCC. The savings in fuel consumption alone would be worth the conversion to an engine with this technology. The Air Force has always been a leader in technological advances and the civilian world will follow. The UCC can have the same impact on the commercial sector as well where savings in fuel consumption is critical to the bottom line.

Appendix A: Figures

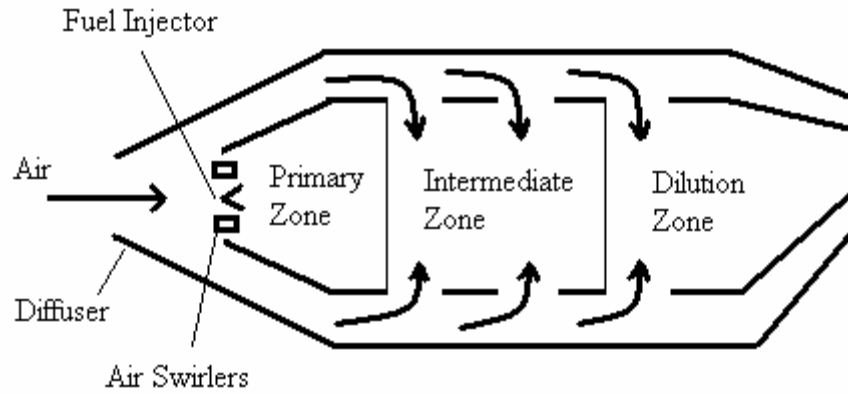


Figure 1: Conventional Combustor (adapted from Lefebvre, 1999:17)

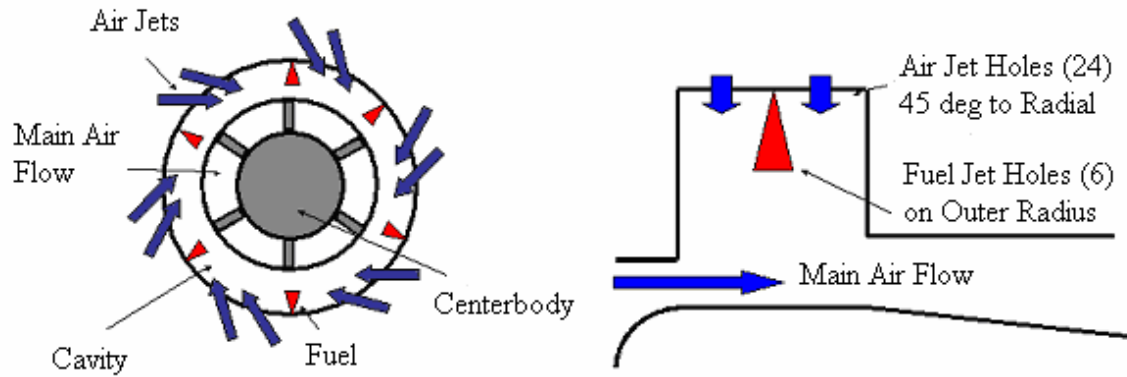


Figure 2: UCC Rear View and UCC Cavity Side View (used with permission from Anthenien, 2001:6)

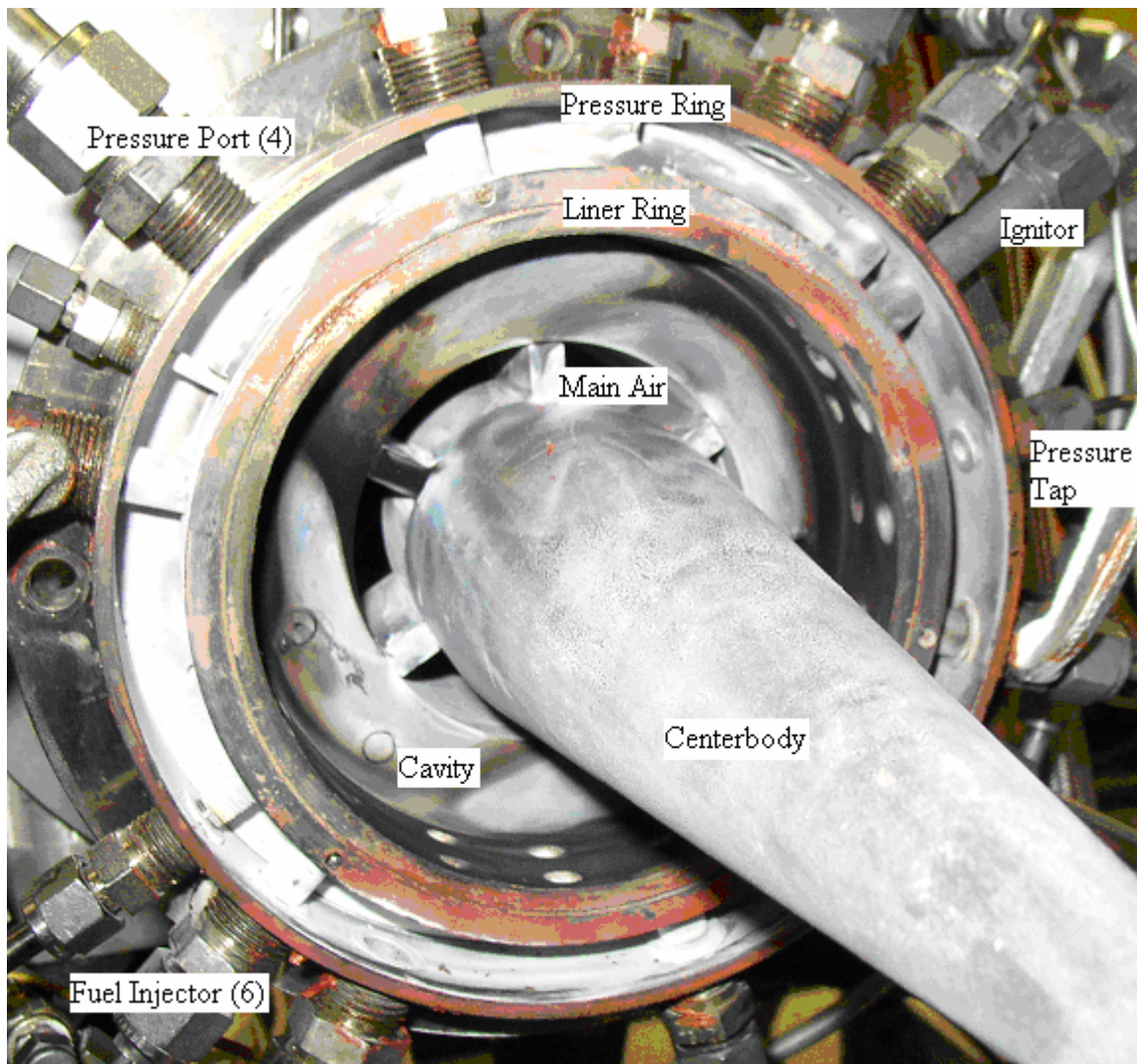


Figure 3: UCC Partially Disassembled Rear View Picture

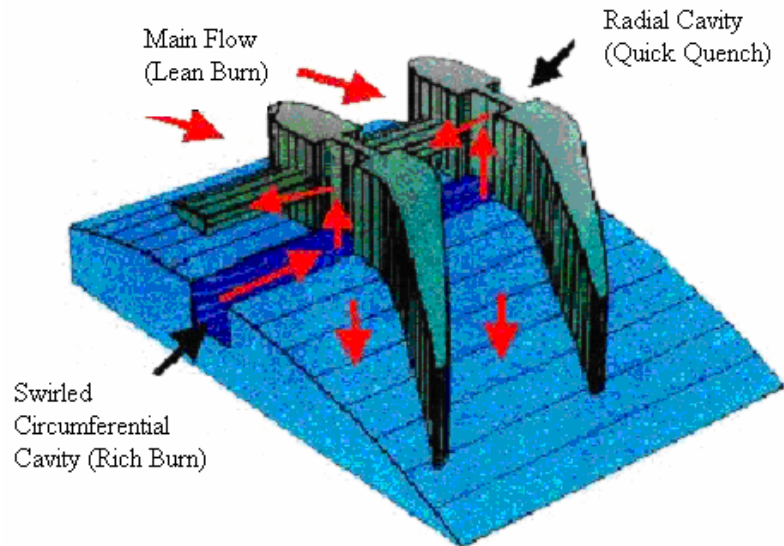


Figure 4: Integration of the UCC and Turning Vanes (used with permission from Anthenien, 2001:6)

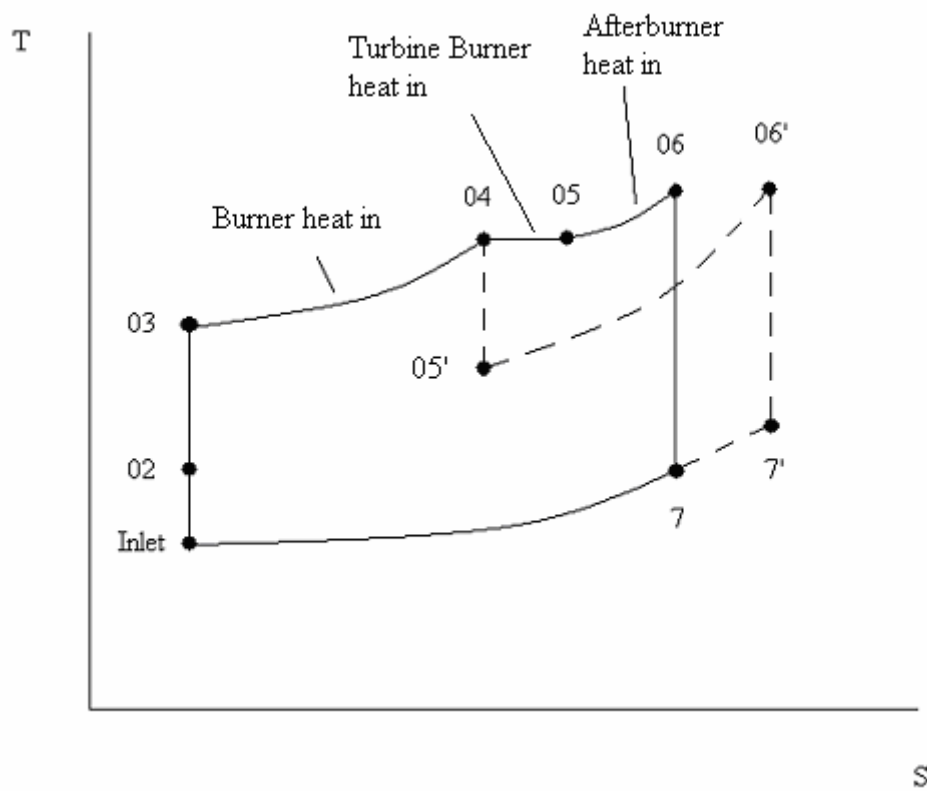


Figure 5: Conventional (dashed line) and ITB Cycle (solid line) T-s Diagram (adapted from Sirignano and Liu, 2001:2)

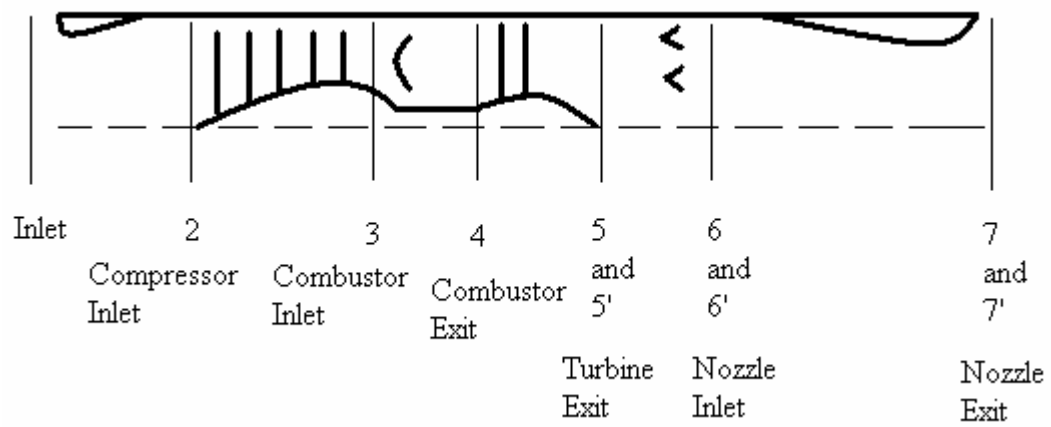


Figure 6: Engine Stations (adapted from Sirignano and Liu, 2001:2)

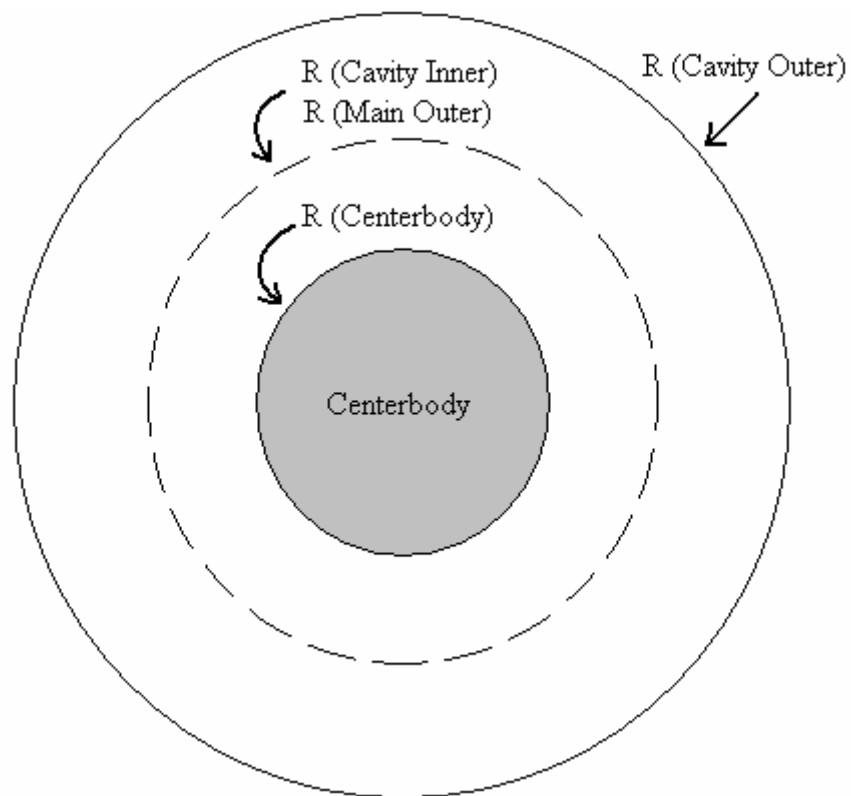


Figure 7: UCC Boundary Condition Locations (rear view not to scale)

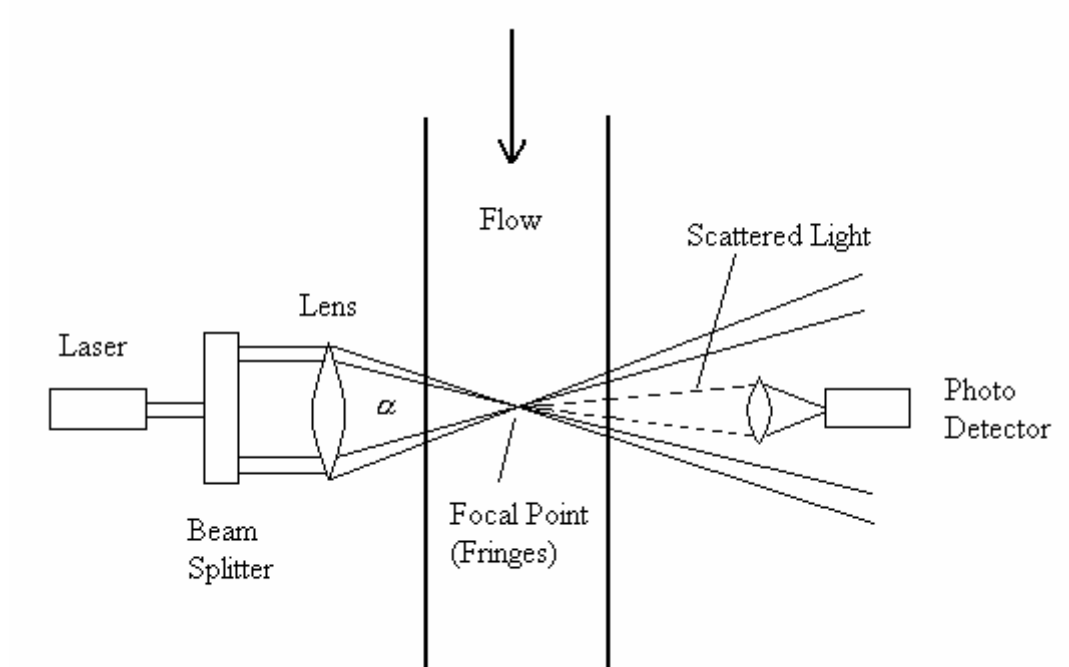


Figure 8: LDV Laser Setup Diagram for Forward Scatter (adapted from Wheeler and Ganji, 1996:311)

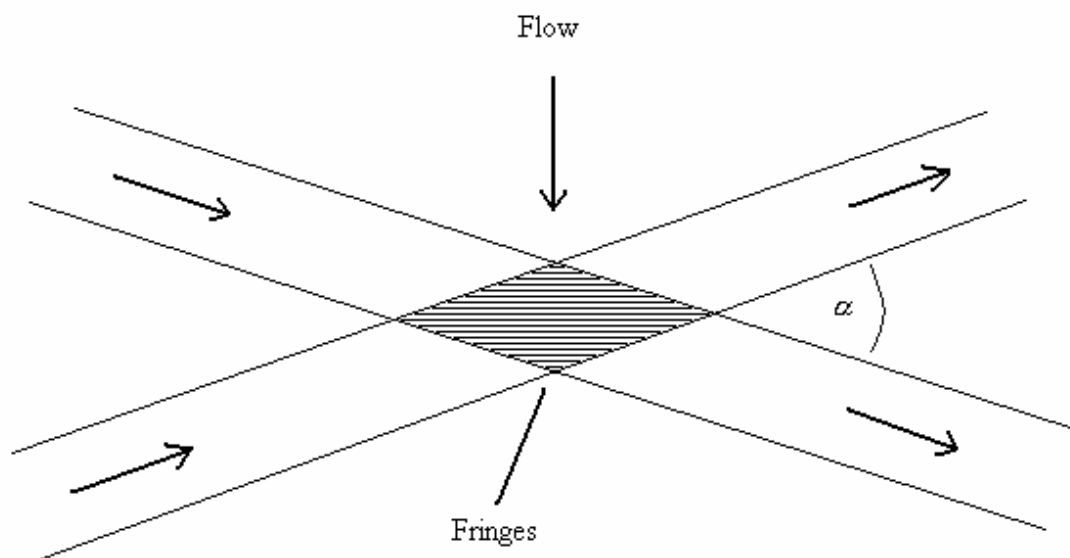


Figure 9: Fringe Diagram for LDV (adapted from Drain, 1980:86)

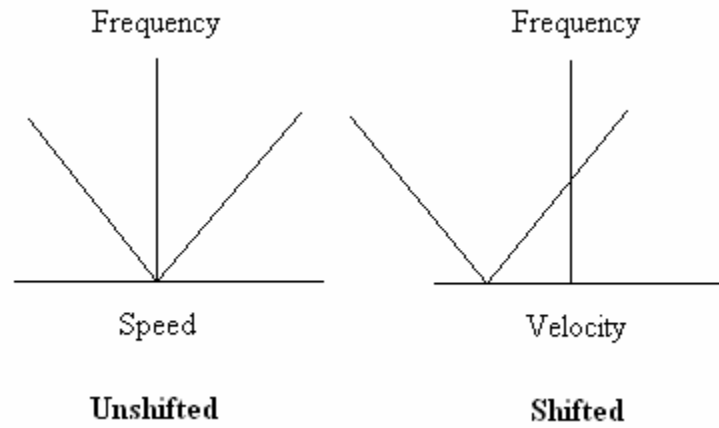


Figure 10: Frequency Shift for Velocity Determination

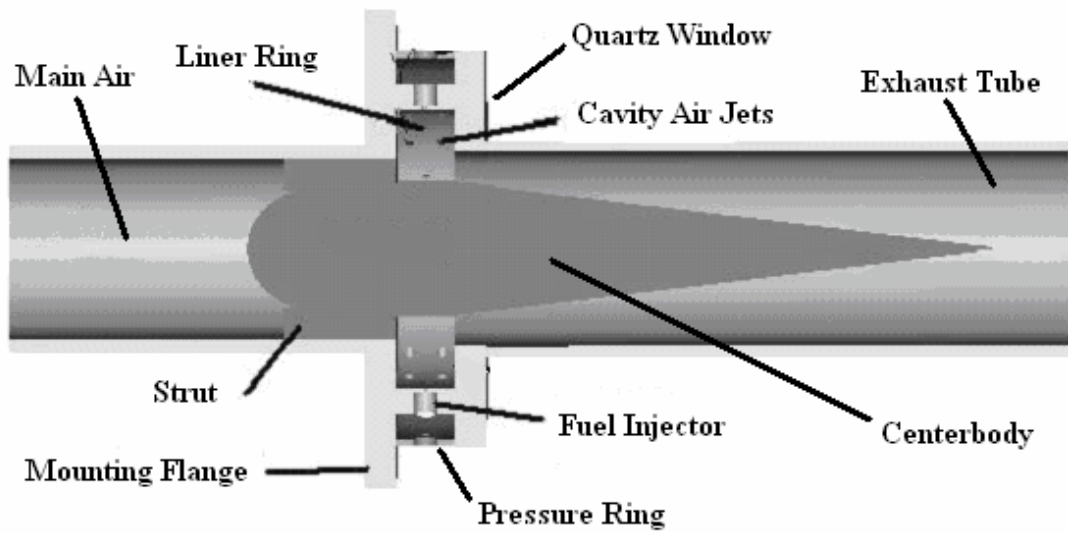


Figure 11: Experimental UCC Cross Section

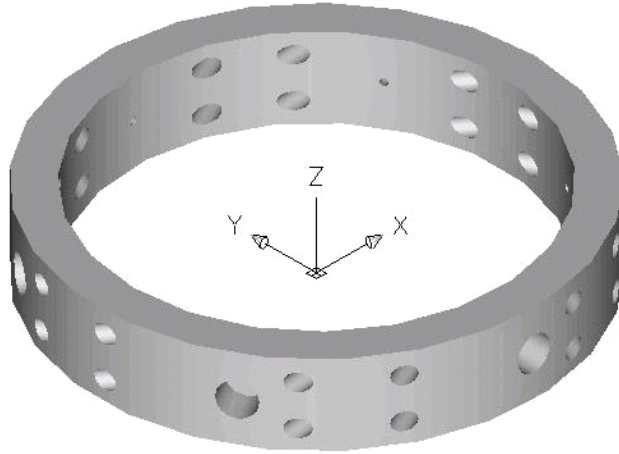


Figure 12: Liner Ring (used with permission from Ehret, 2002: Appendix A)



Figure 13: Quartz Window Picture Following Testing

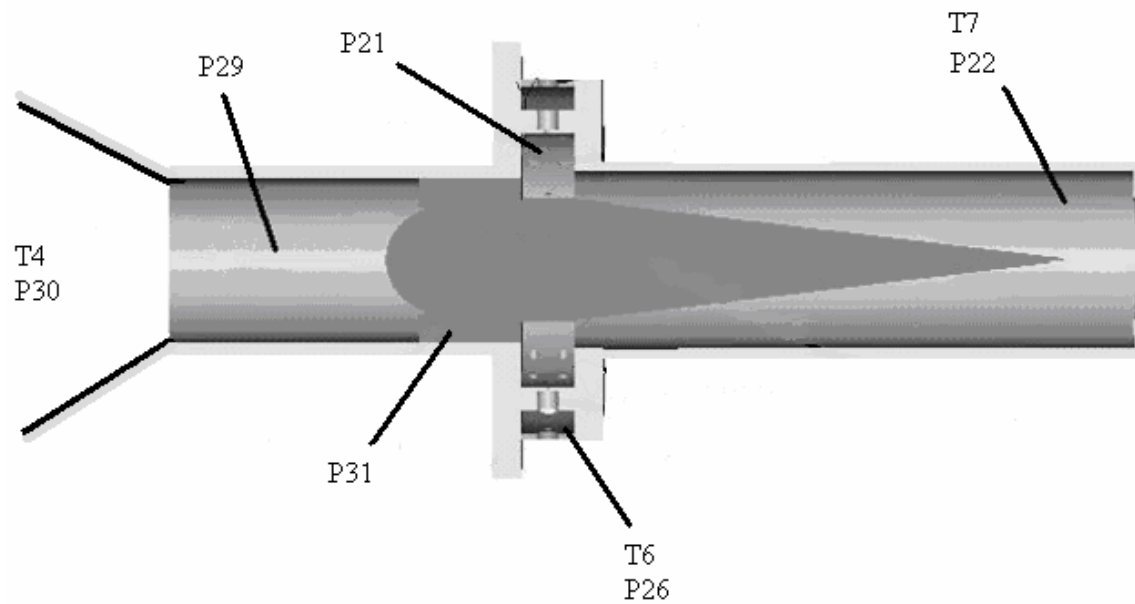


Figure 14: Pressure and Temperature Tap Locations

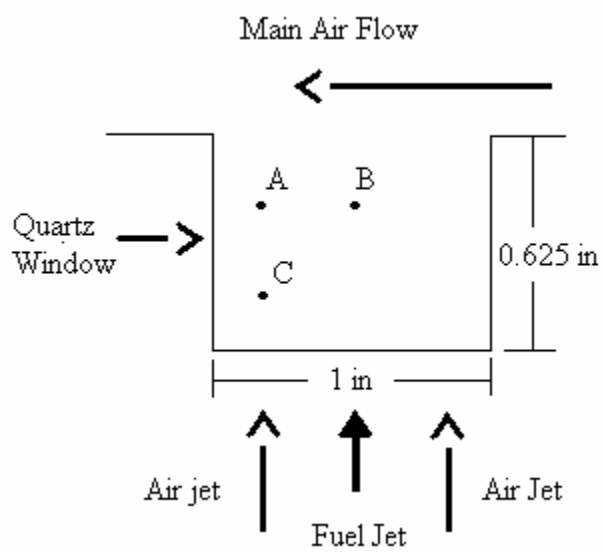


Figure 15: Diagram of LDV Measurement Positions A, B and C

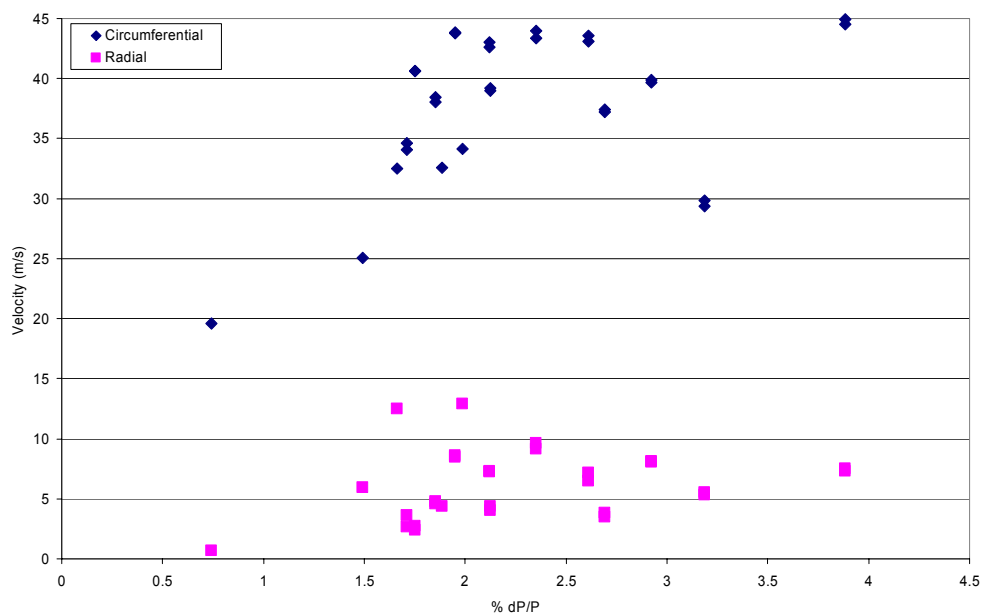


Figure 16: Circumferential and Radial Velocities at ~22% Cavity Air Mass Flow For All Equivalence Ratios (Position A)

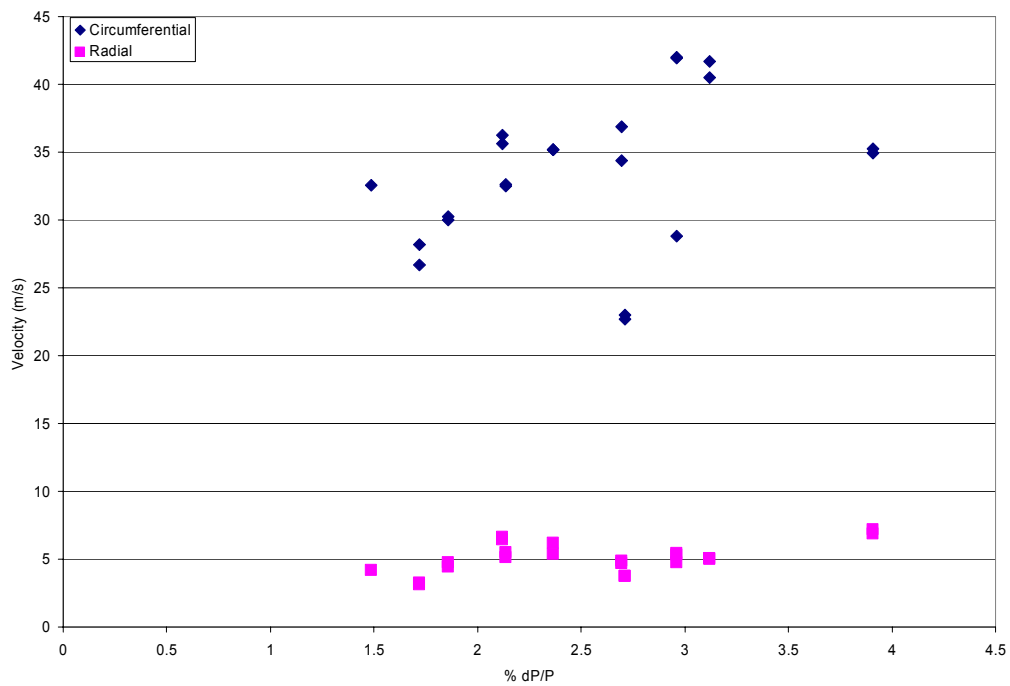


Figure 17: Circumferential and Radial Velocities at ~22% Cavity Air Mass Flow For All Equivalence Ratios (Position C)

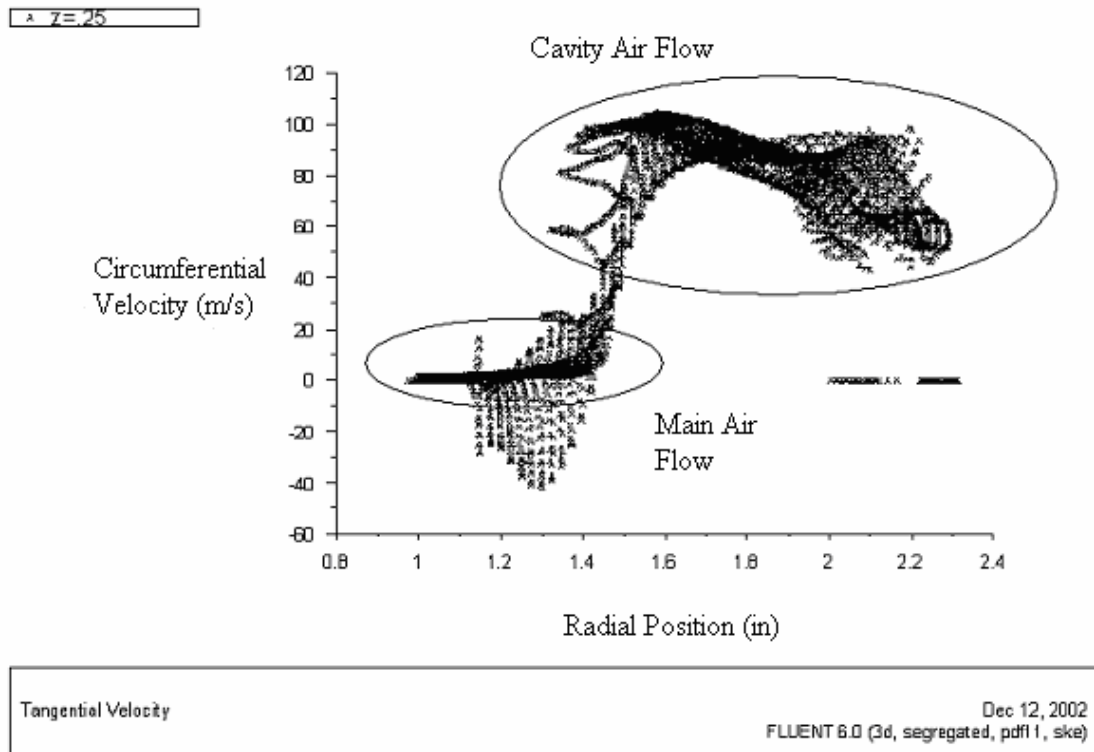


Figure 18: CFD Raw Data Plot of Circumferential Velocity at 4% Pressure Drop In Line with Upstream Air Jets (used with permission from Ehret)

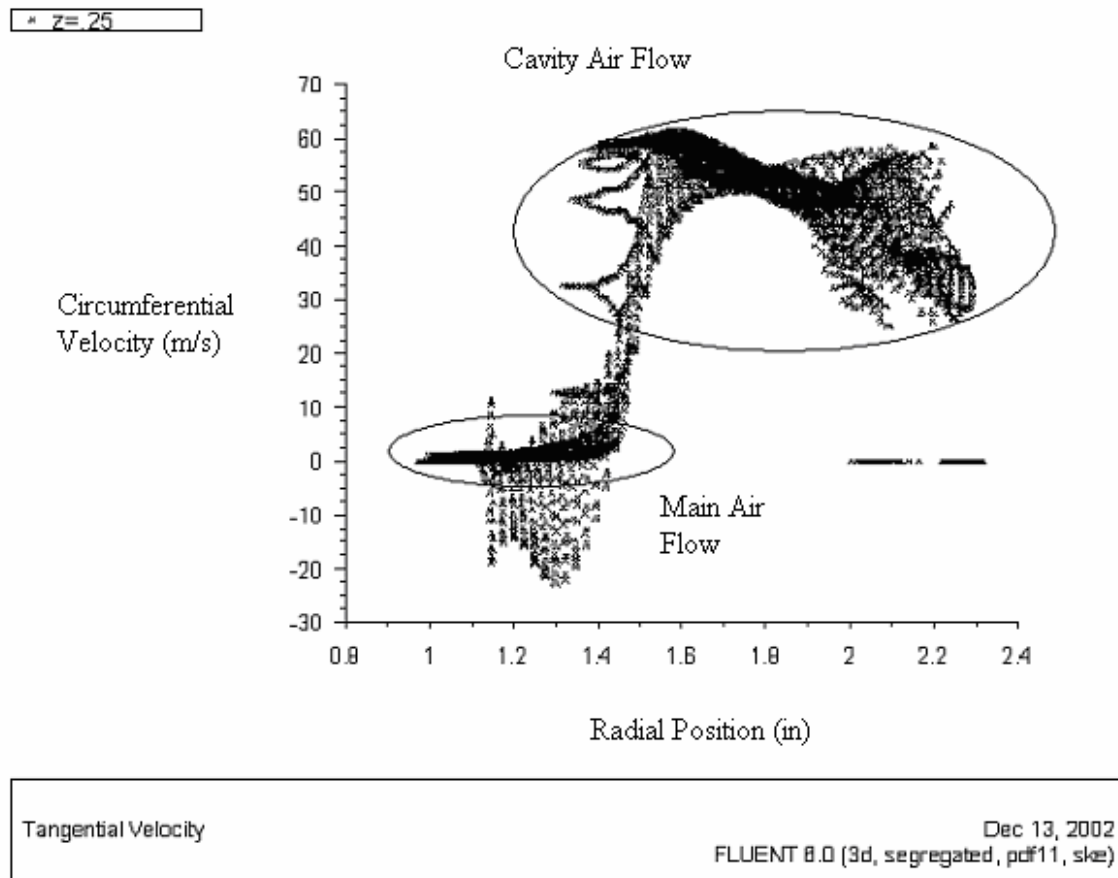


Figure 19: CFD Raw Data Plot of Circumferential Velocity at 2% Pressure Drop In Line with Upstream Air Jets (used with permission from Ehret)

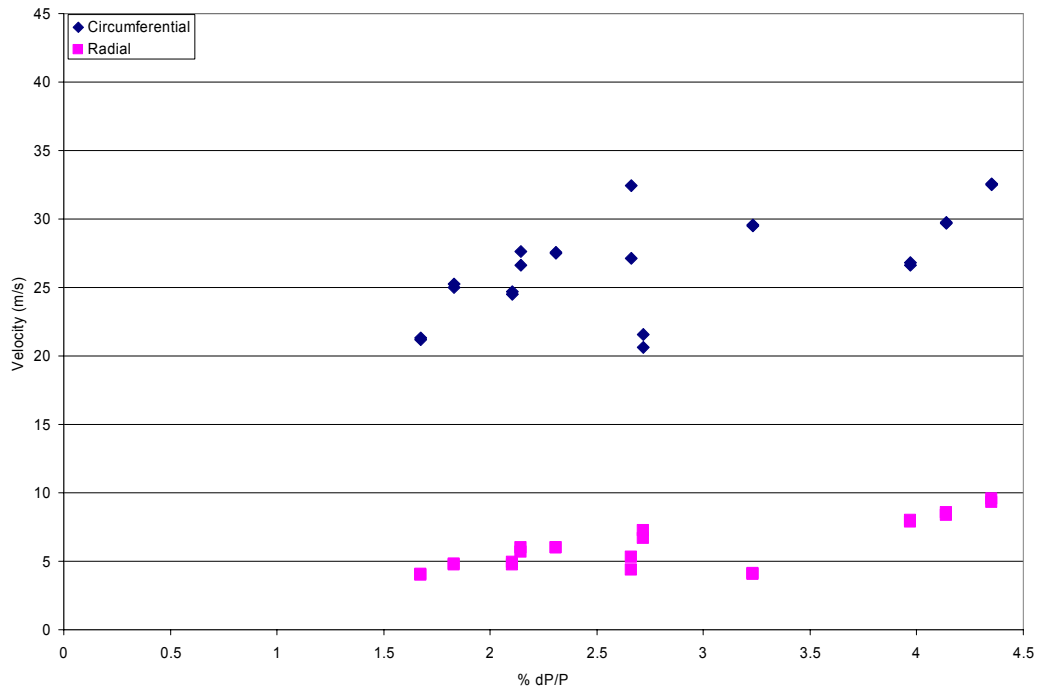


Figure 20: Circumferential and Radial Velocities at ~22% Cavity Air Mass Flow For All Equivalence Ratios (Position B)

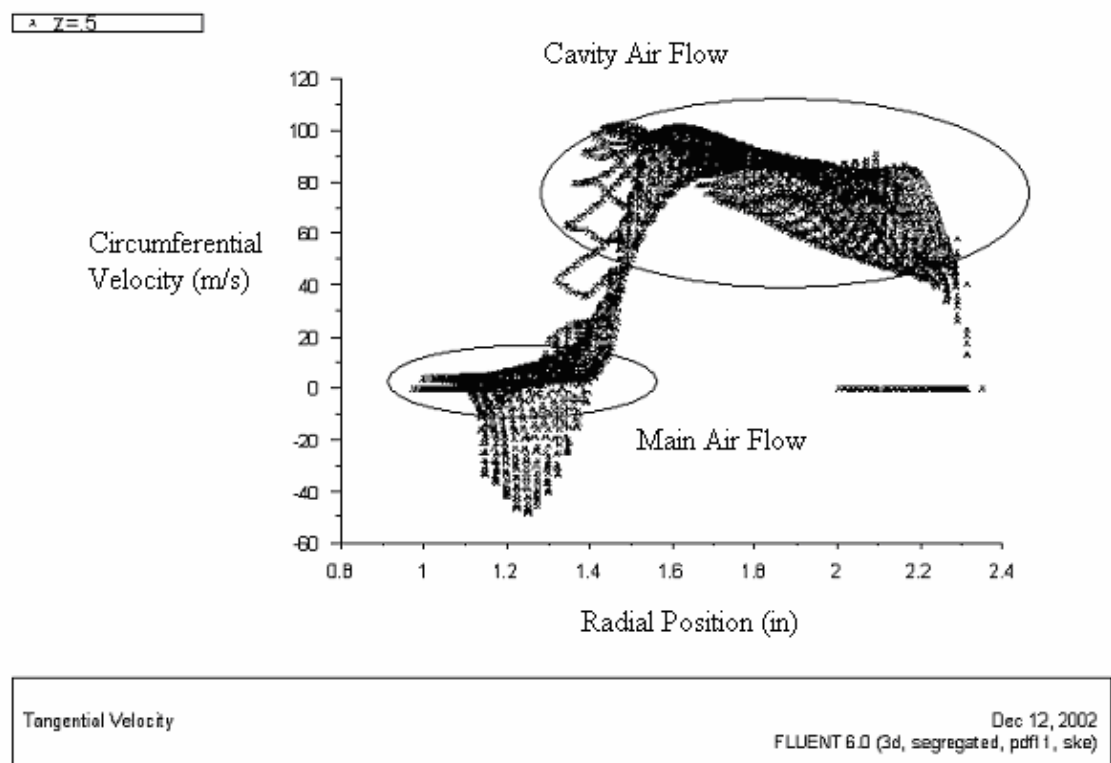


Figure 21: CFD Raw Data Plot of Circumferential Velocity at 4% Pressure Drop In Line with Fuel Injector (used with permission from Ehret)

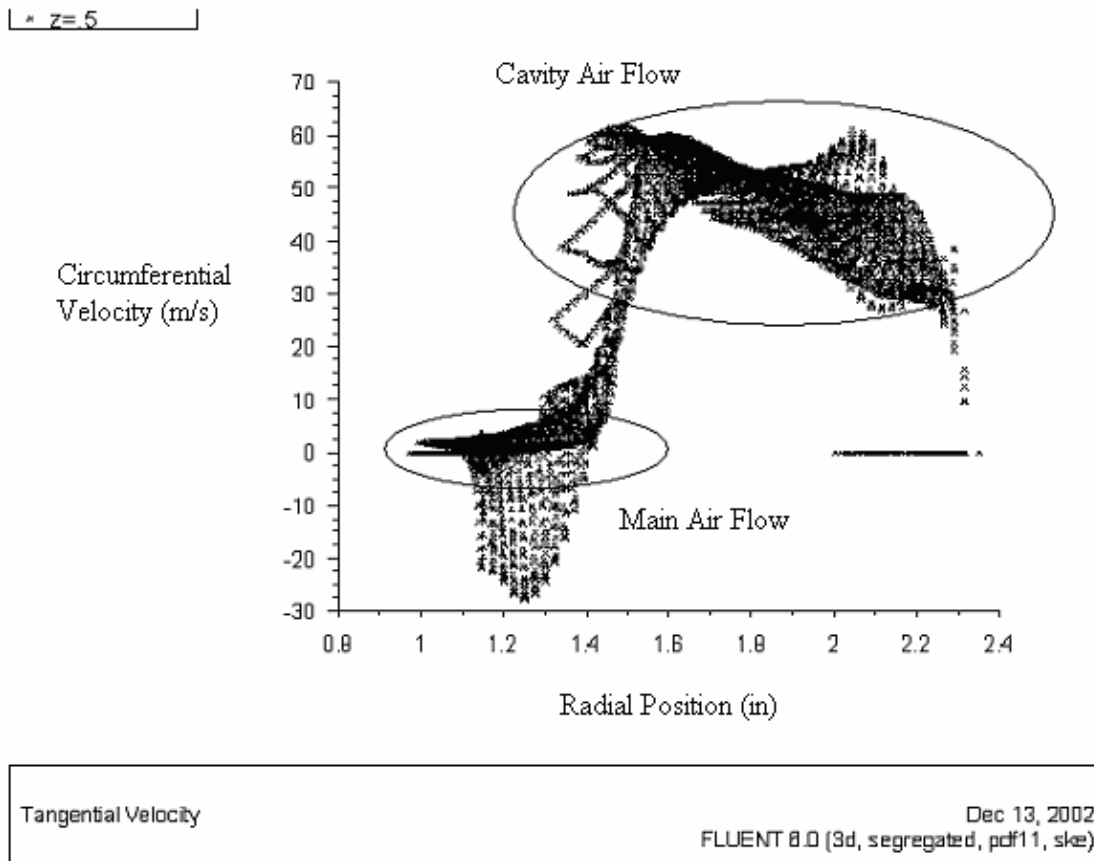


Figure 22: CFD Raw Data Plot of Circumferential Velocity at 2% Pressure Drop In Line with Fuel Injector (used with permission from Ehret)

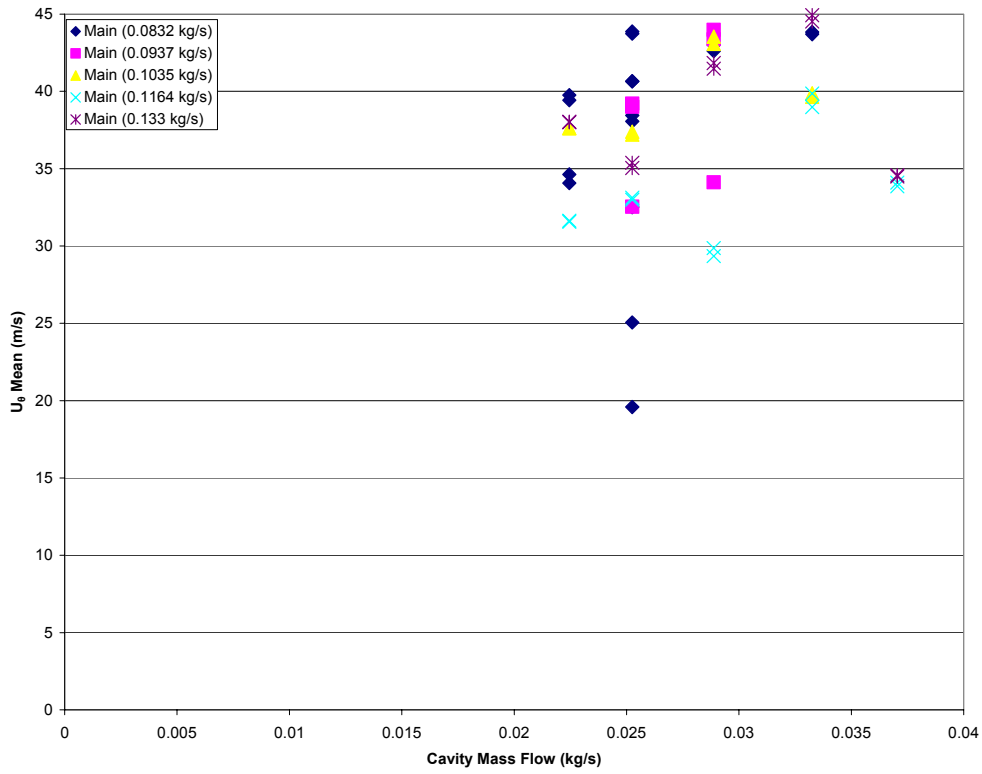


Figure 23: U_θ Mean for All Equivalence Ratios (Position A)

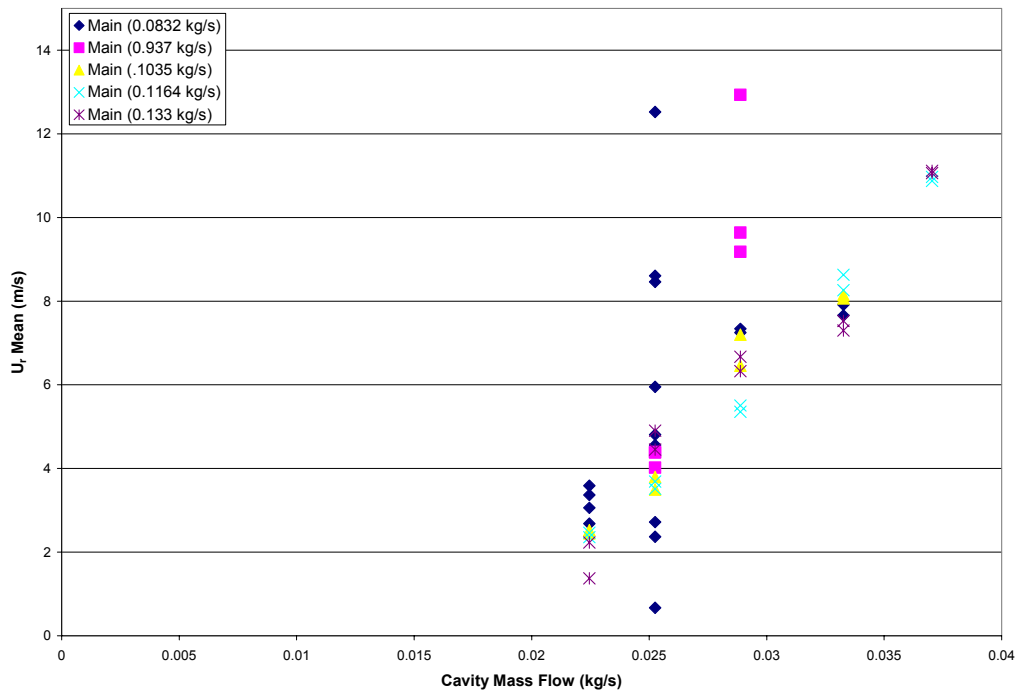


Figure 24: U_r Mean for All Equivalence Ratios (Position A)

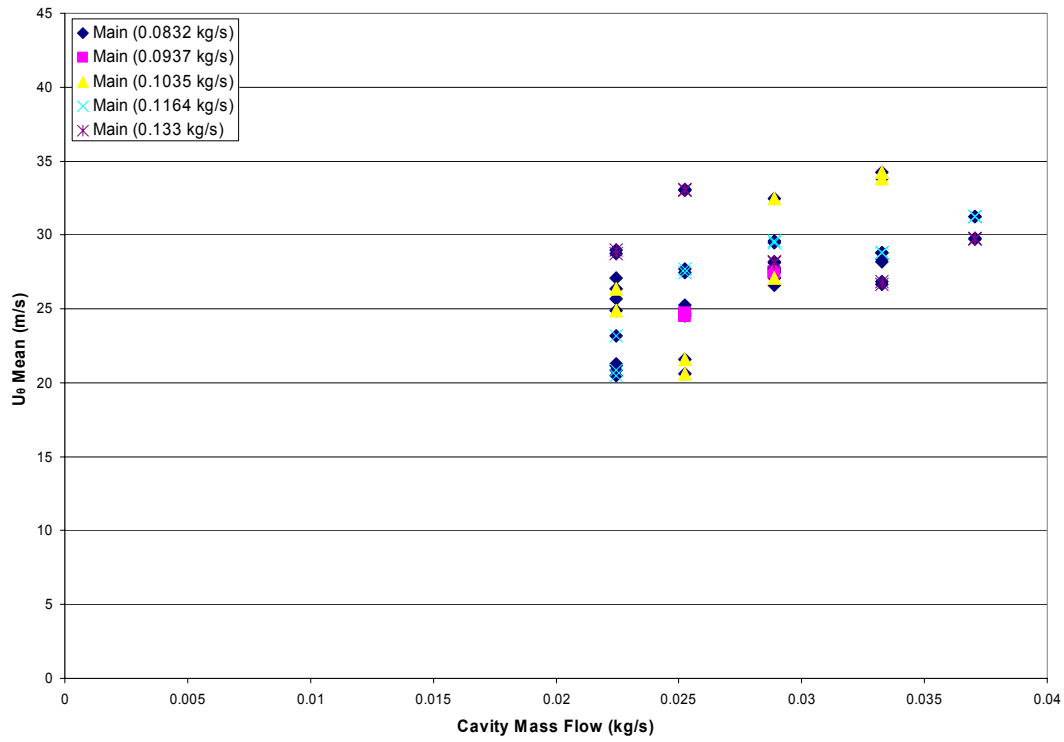


Figure 25: U_θ Mean for All Equivalence Ratios (Position B)

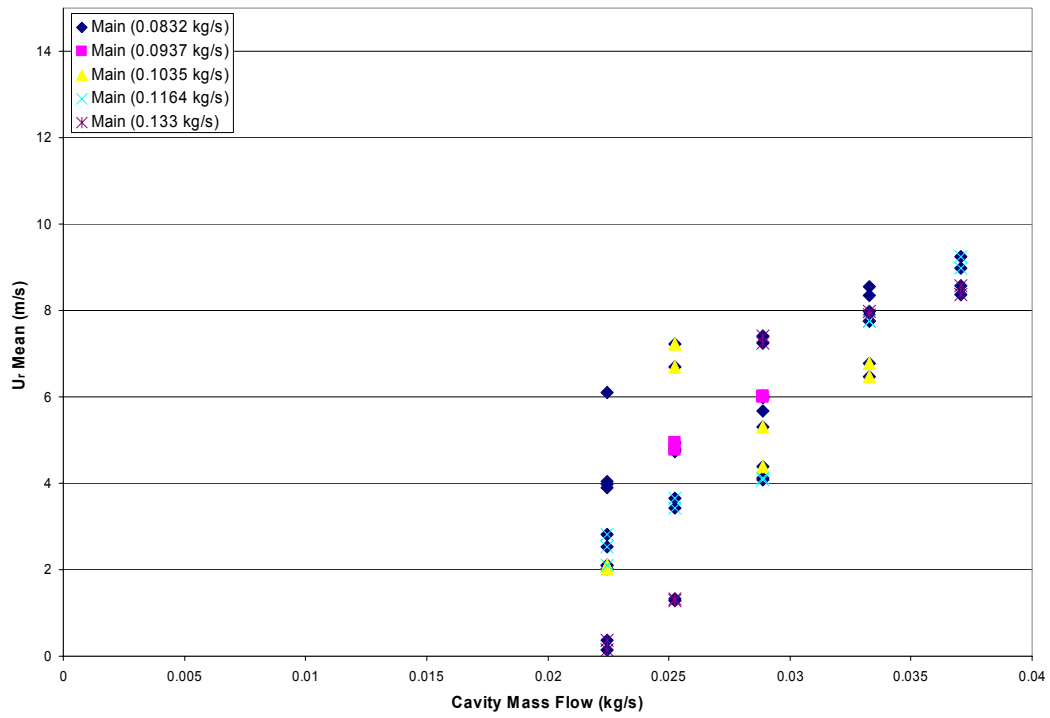


Figure 26: U_r Mean for All Equivalence Ratios (Position B)

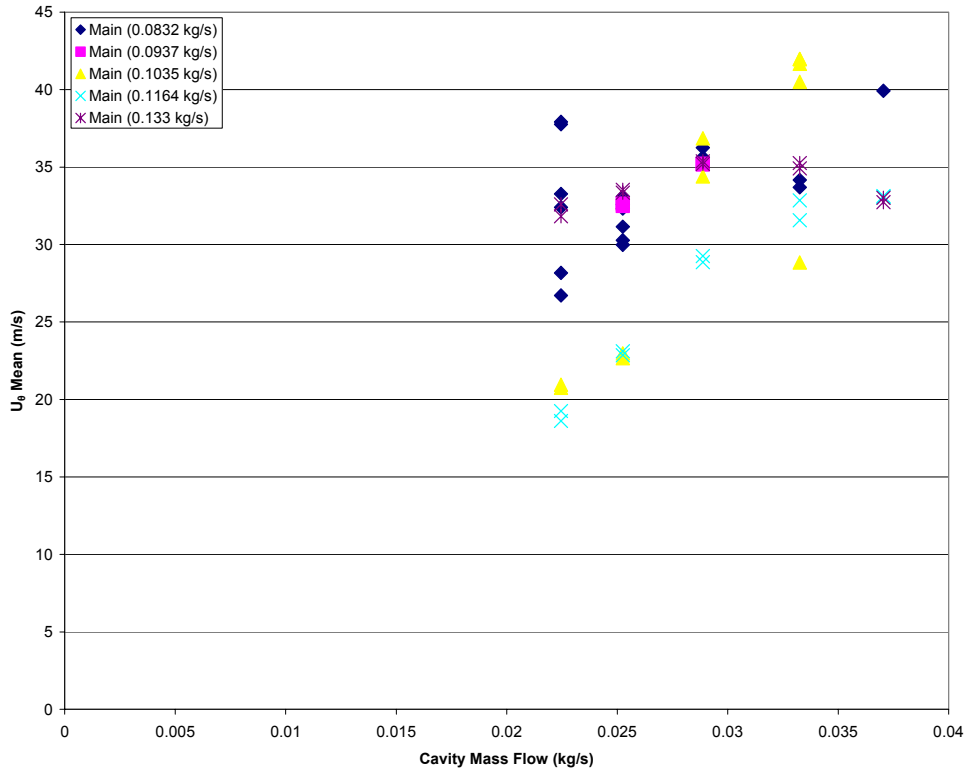


Figure 27: U_θ Mean for All Equivalence Ratios (Position C)

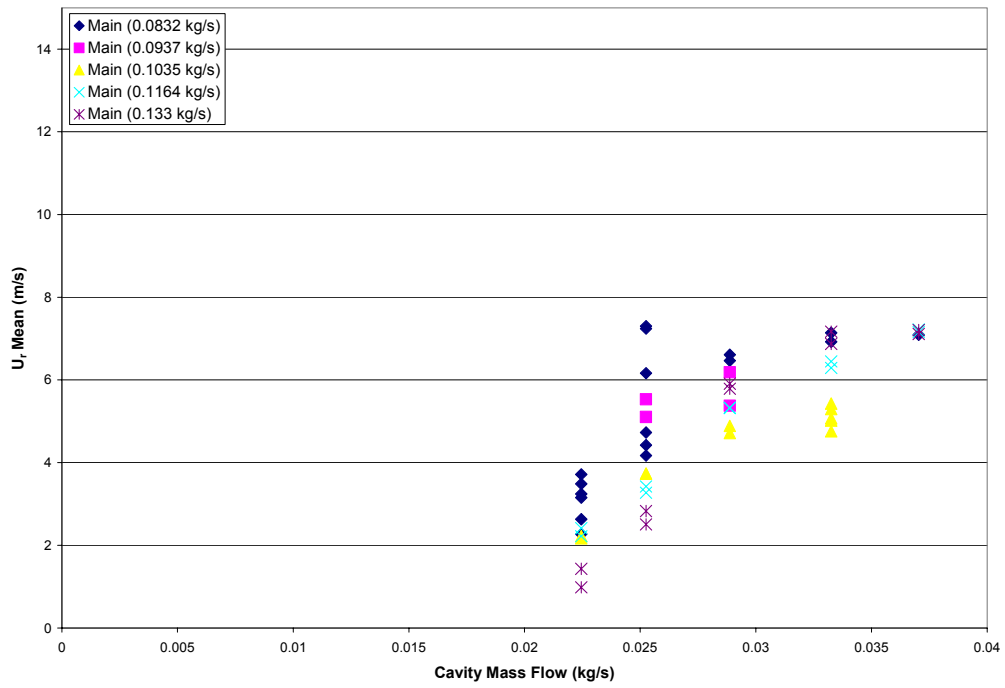


Figure 28: U_r Mean for All Equivalence Ratios (Position C)

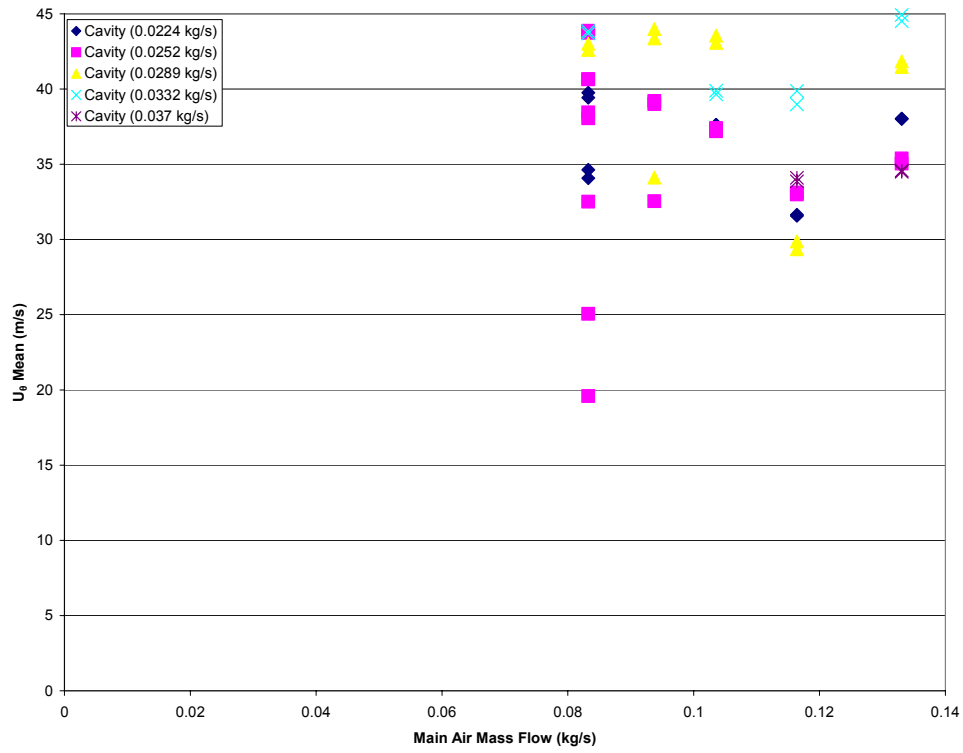


Figure 29: Main Air Effect on U_θ Mean for All Equivalence Ratios (Position A)

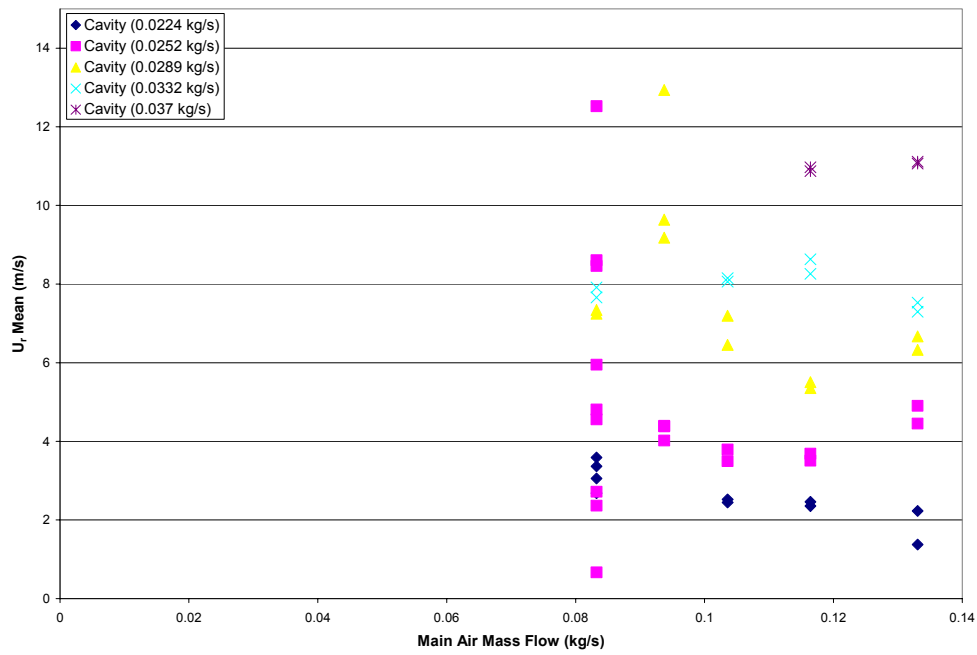


Figure 30: Main Air Effect on U_r Mean for All Equivalence Ratios (Position A)

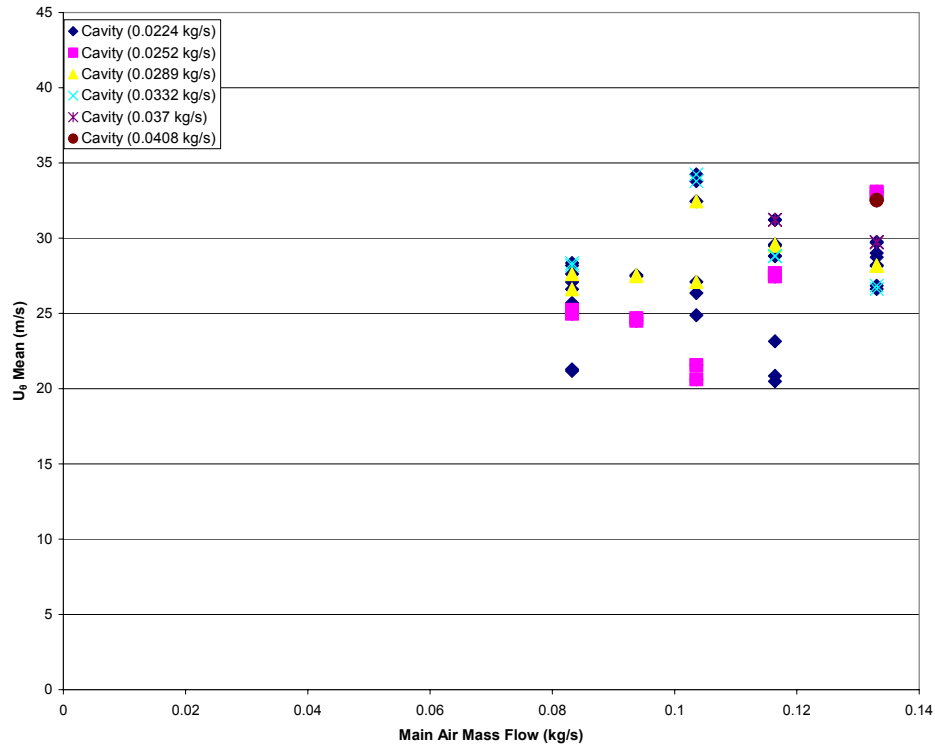


Figure 31: Main Air Effect on U_0 Mean for All Equivalence Ratios (Position B)

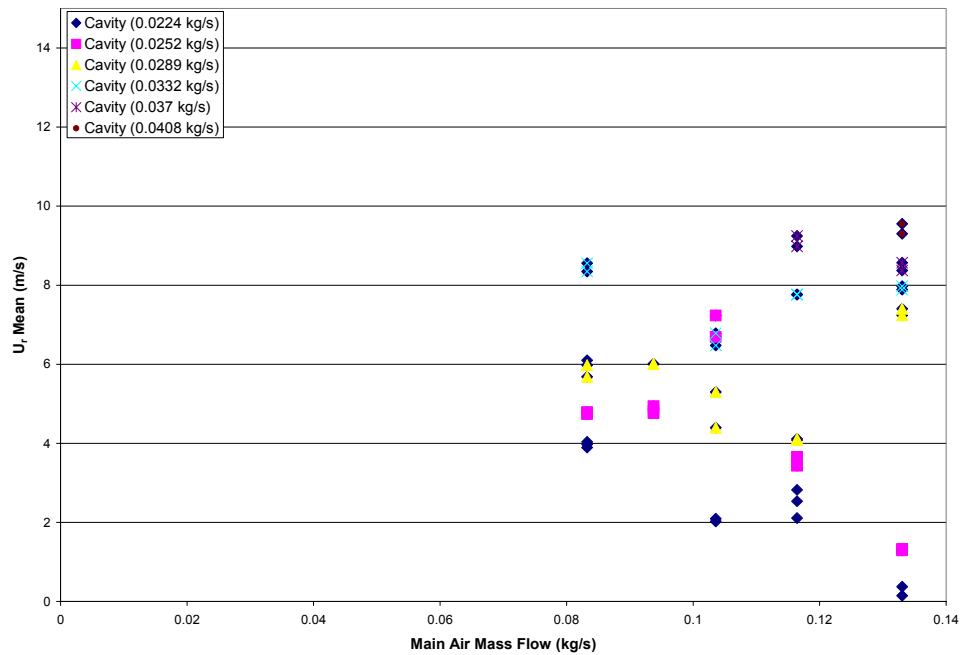


Figure 32: Main Air Effect on U_r Mean for All Equivalence Ratios (Position B)

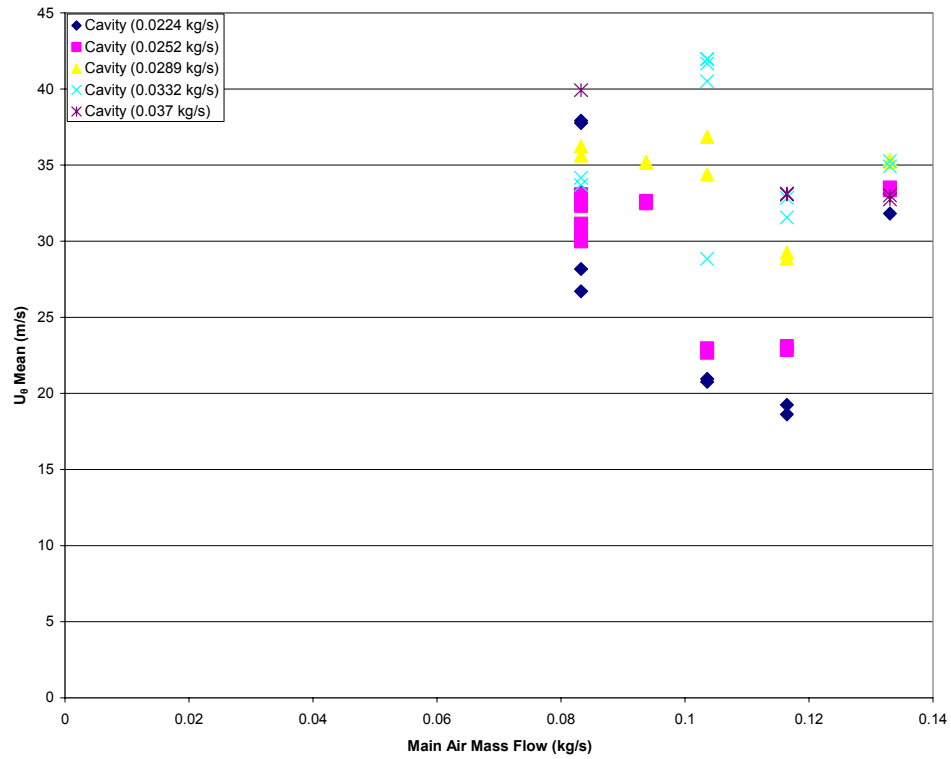


Figure 33: Main Air Effect on U_0 Mean for All Equivalence Ratios (Position C)

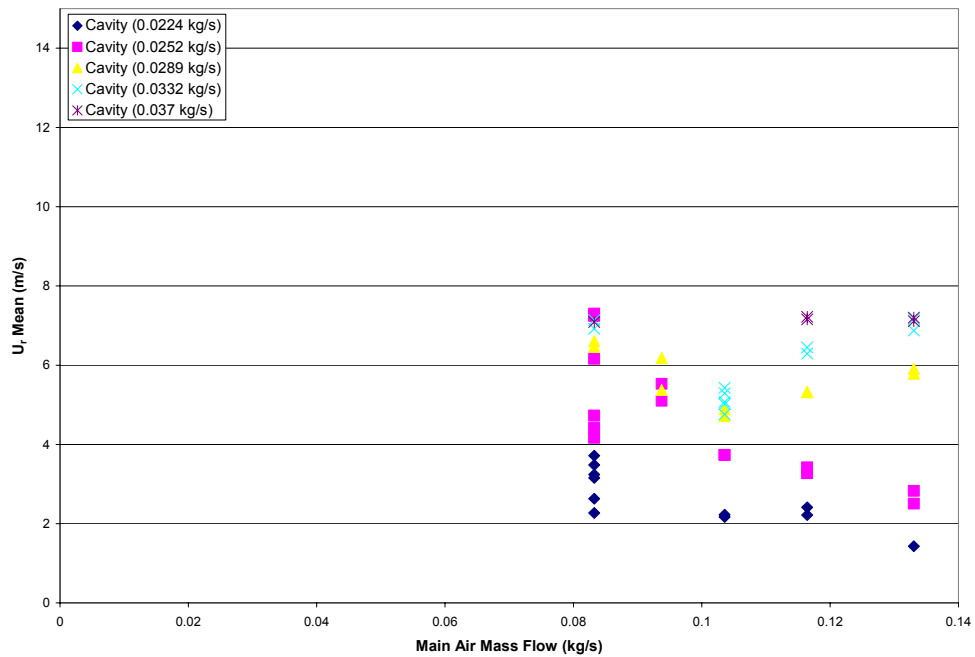


Figure 34: Main Air Effect on U_r Mean for All Equivalence Ratios (Position C)

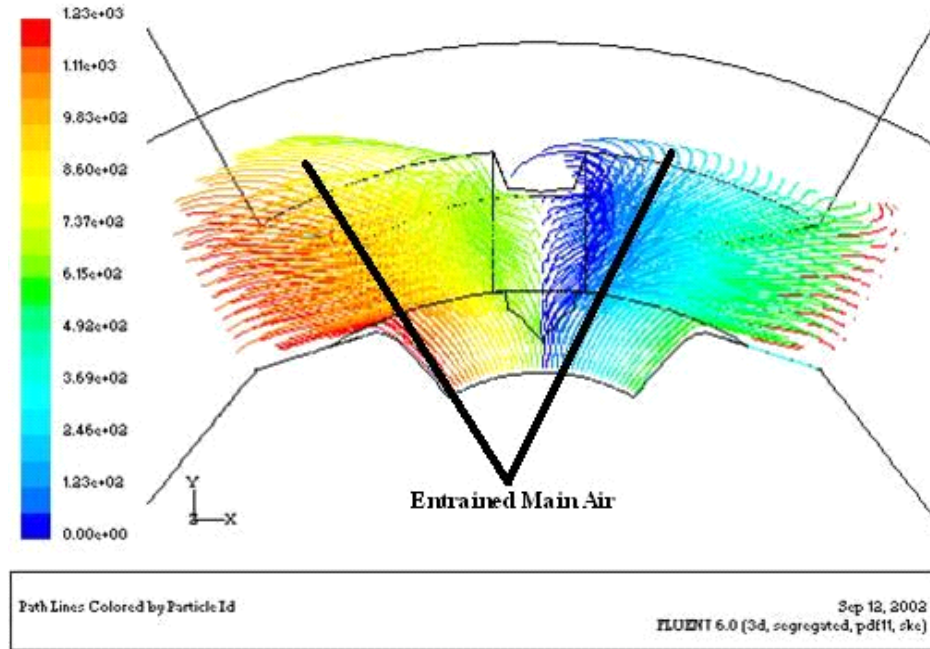


Figure 35: Front View of Main Air Entrainment at 4% Pressure Drop and 22% Cavity Air Mass Flow (used with permission from Ehret, 2002: Appendix A)

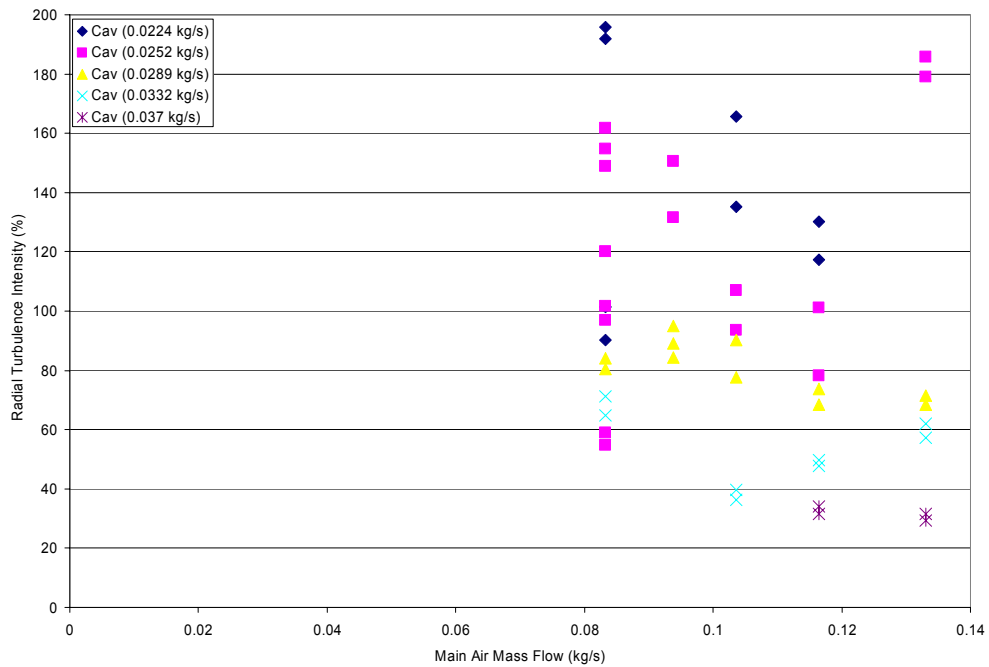


Figure 36: Effect of Main and Cavity Air Mass Flow on Radial Turbulence Intensity (Position A)

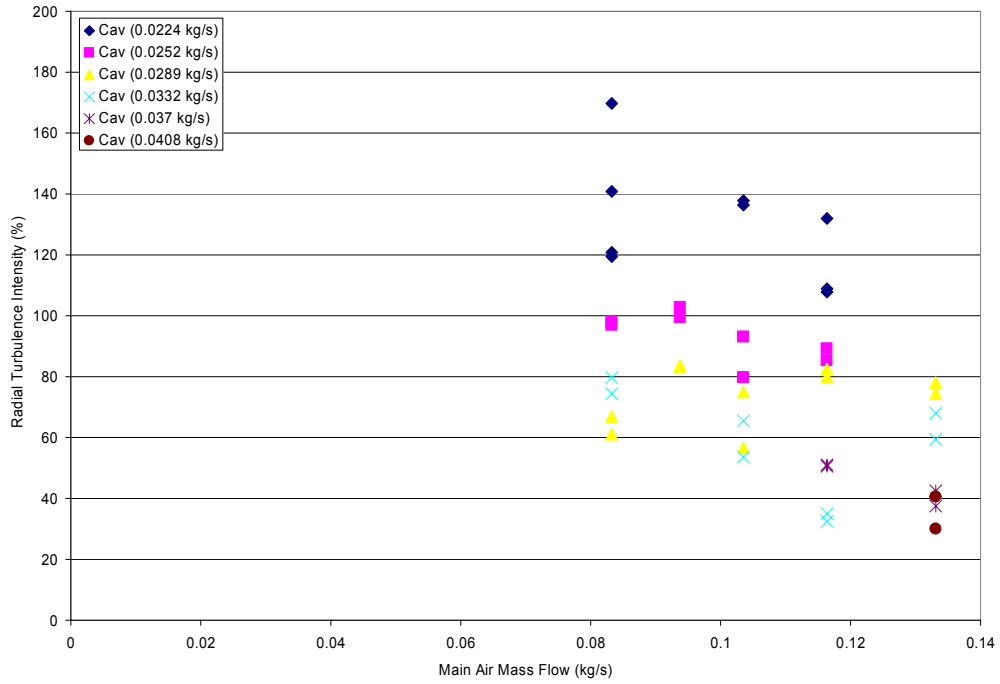


Figure 37: Effect of Main and Cavity Air Mass Flow on Radial Turbulence Intensity (Position B)

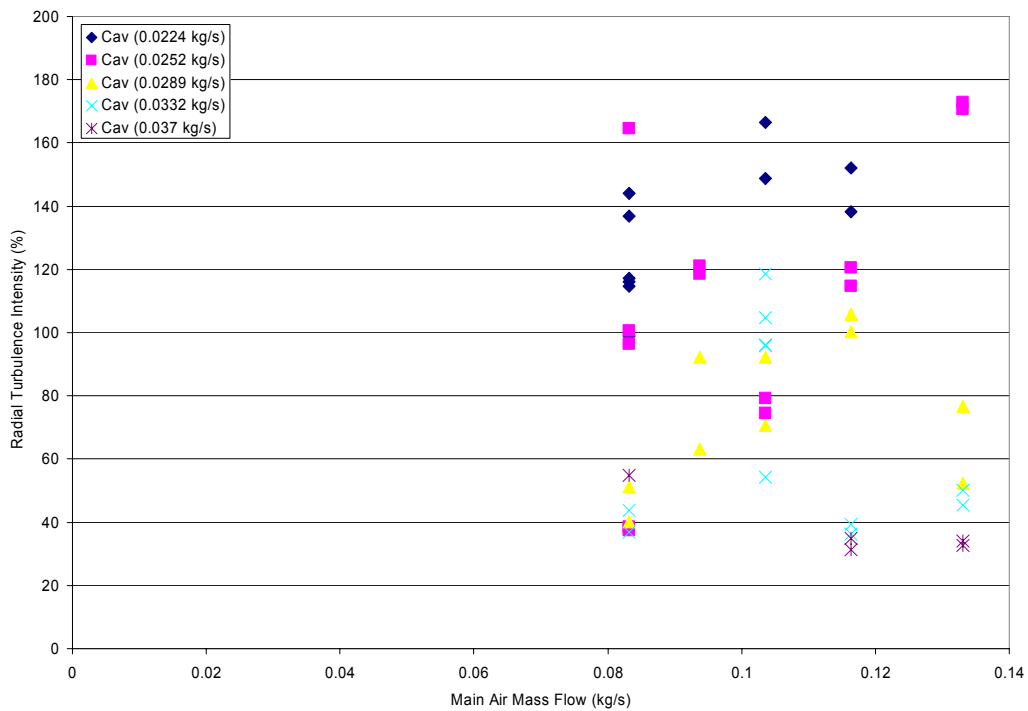


Figure 38: Effect of Main and Cavity Air Mass Flow on Radial Turbulence Intensity (Position C)

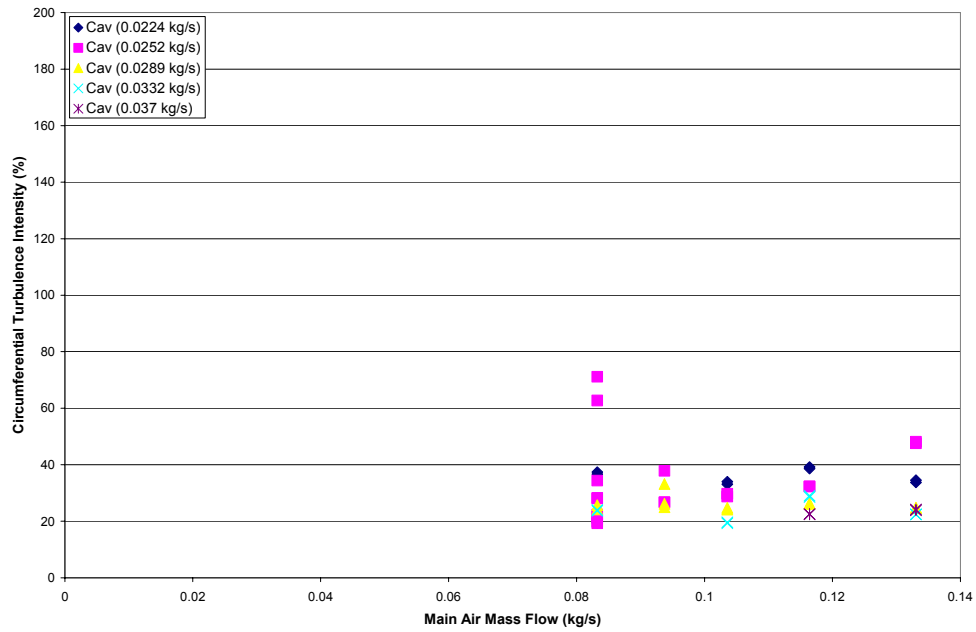


Figure 39: Effect of Main and Cavity Air Mass Flow on Circumferential Turbulence Intensity (Position A)

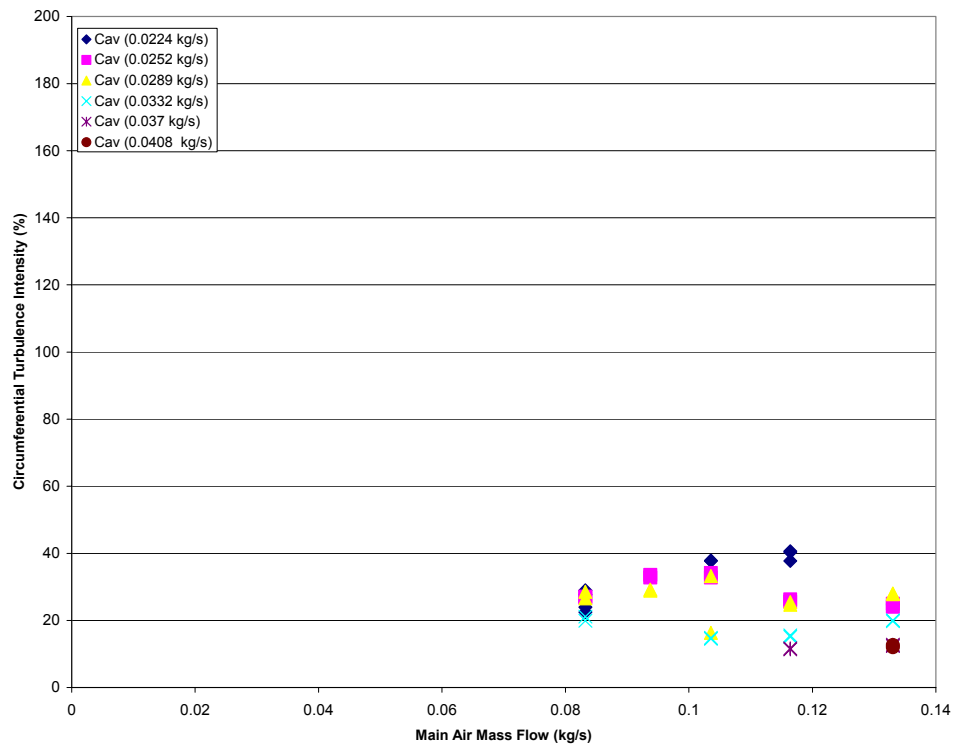


Figure 40: Effect of Main and Cavity Air Mass Flow on Circumferential Turbulence Intensity (Position B)

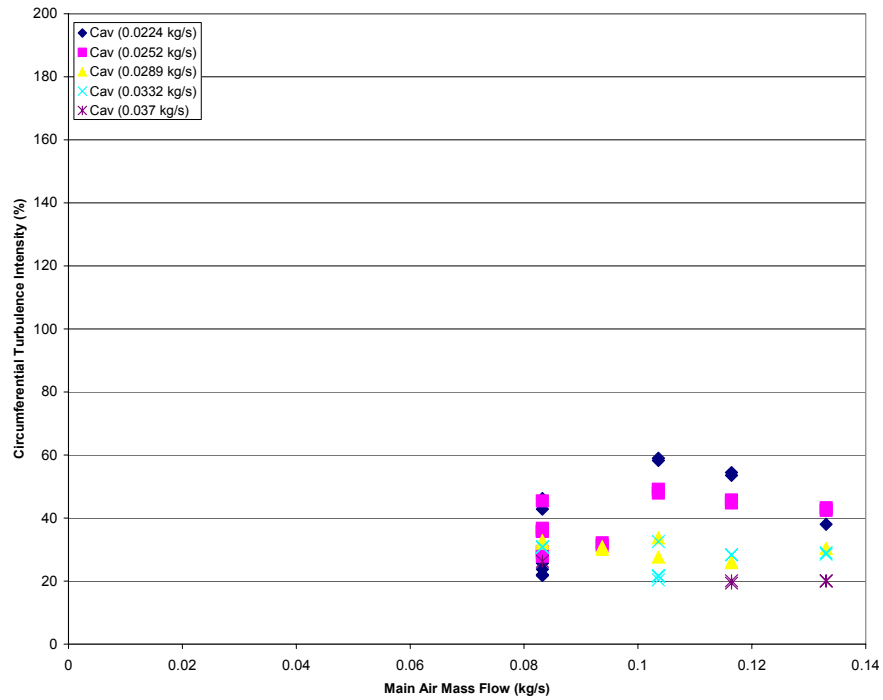


Figure 41: Effect of Main and Cavity Air Mass Flow on Circumferential Turbulence Intensity (Position C)

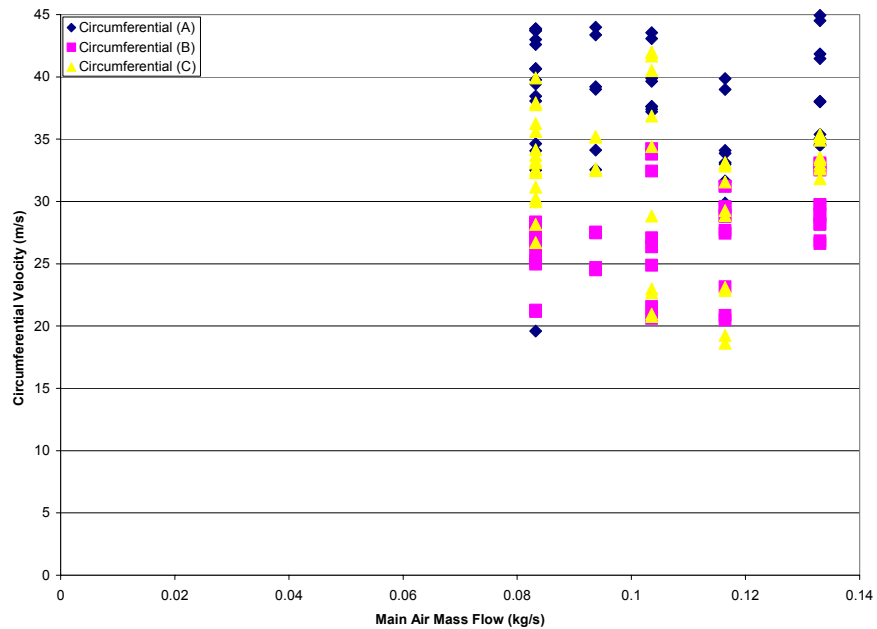


Figure 42: Circumferential Velocities for Positions A, B and C with Main Air Mass Flow

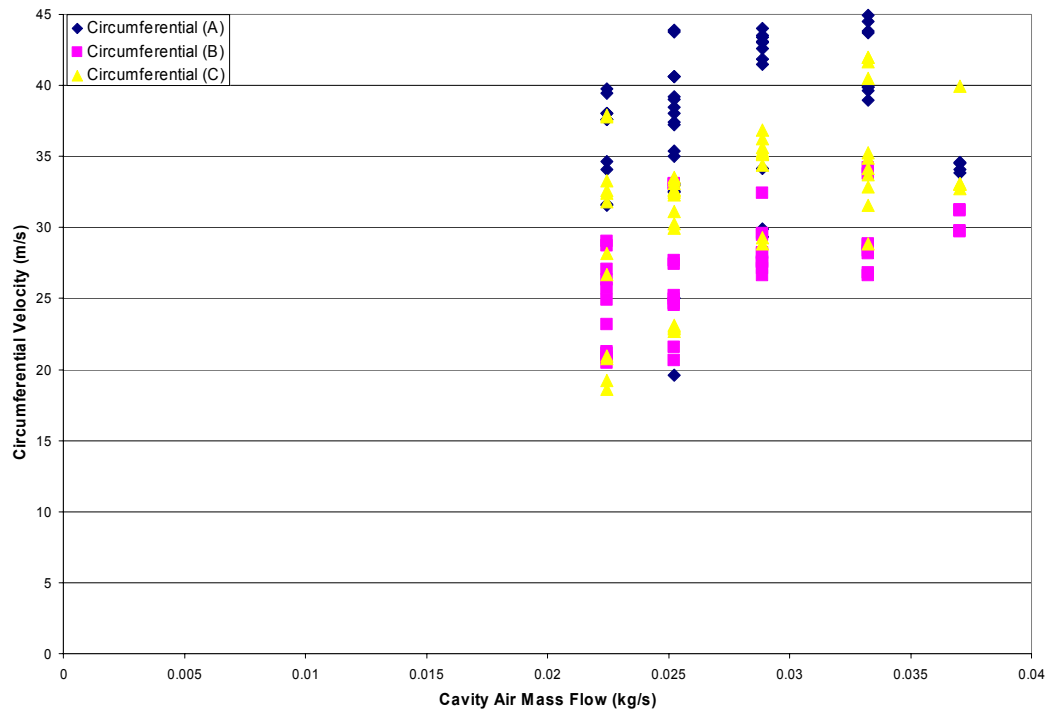


Figure 43: Circumferential Velocities for Positions A, B and C with Cavity Air Mass Flow

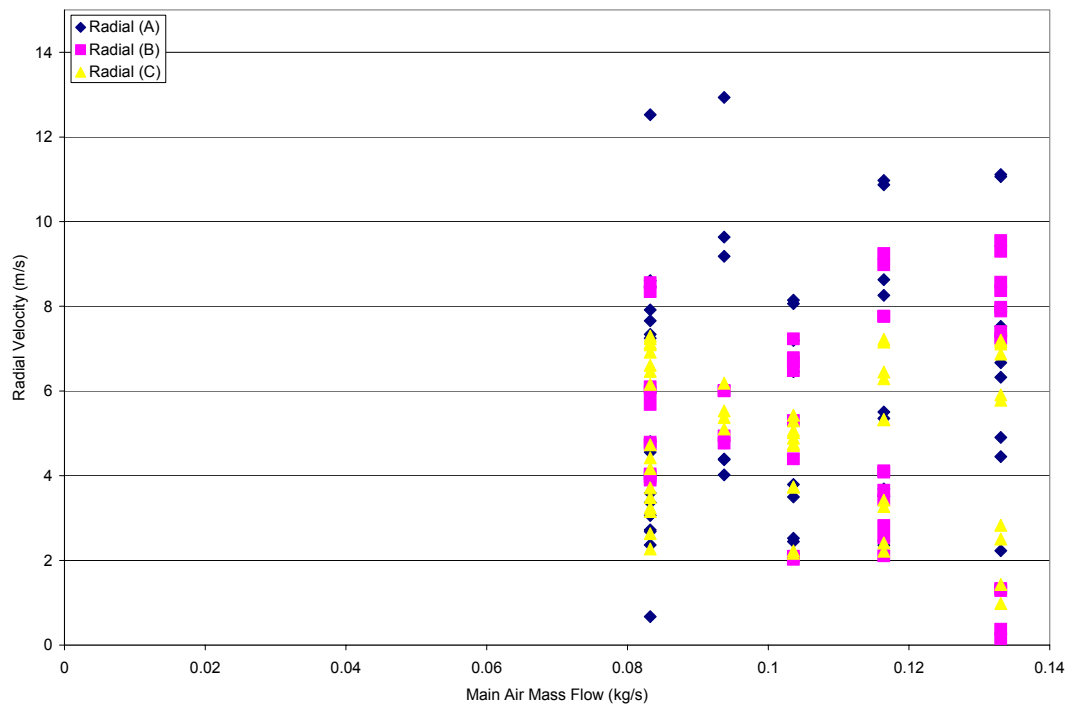


Figure 44: Radial Velocities for Positions A, B and C with Main Air Mass Flow

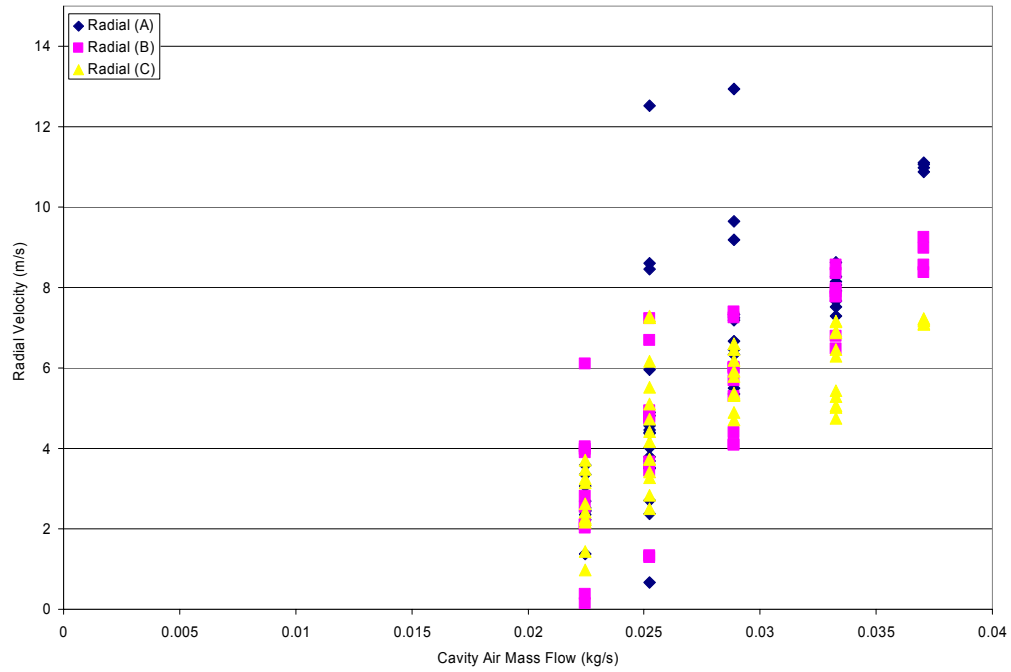


Figure 45: Radial Velocities for Positions A, B and C with Cavity Air Mass Flow

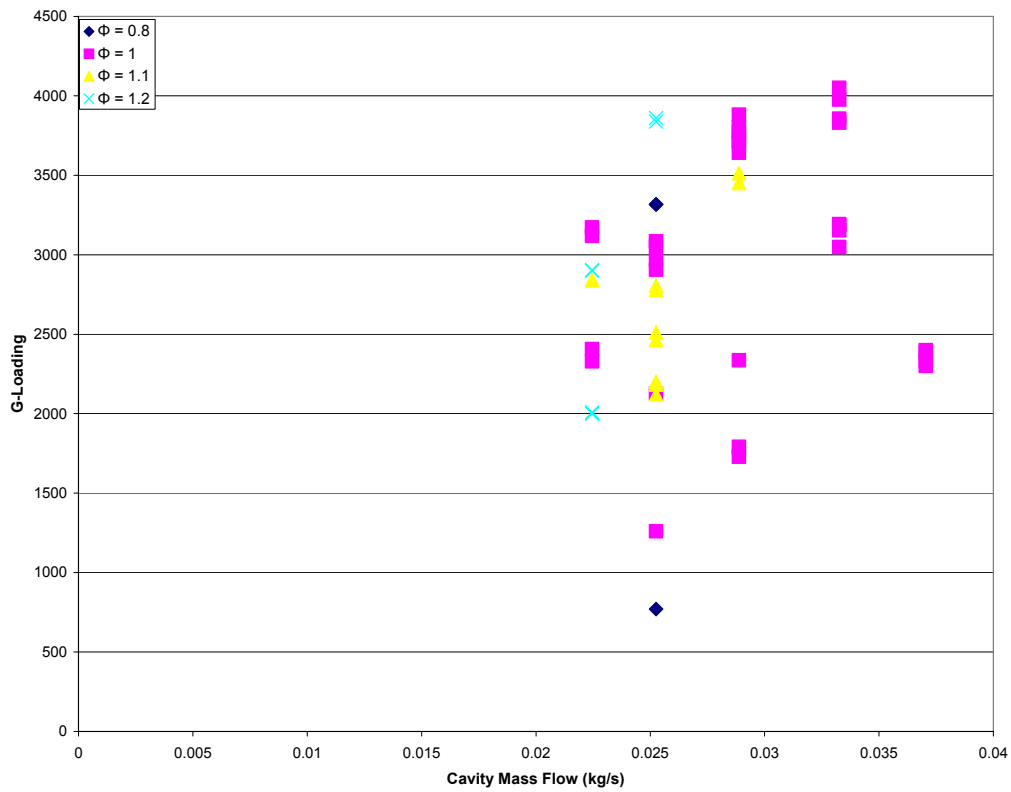


Figure 46: Impact of Φ on G-Loading and Cavity Mass Flow (Position A)

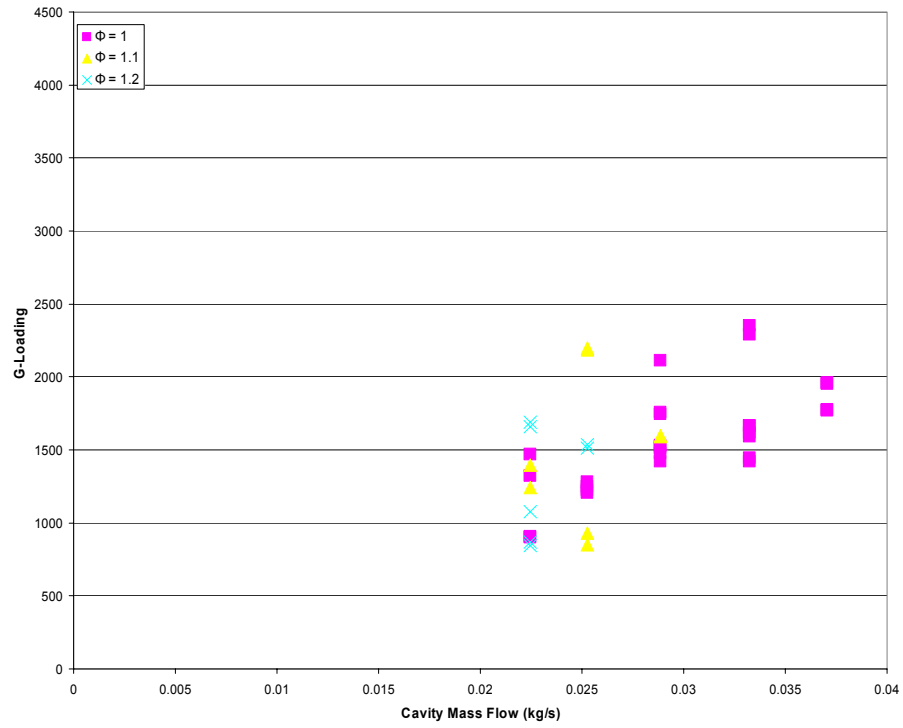


Figure 47: Impact of Φ on G-Loading and Cavity Mass Flow (Position B)

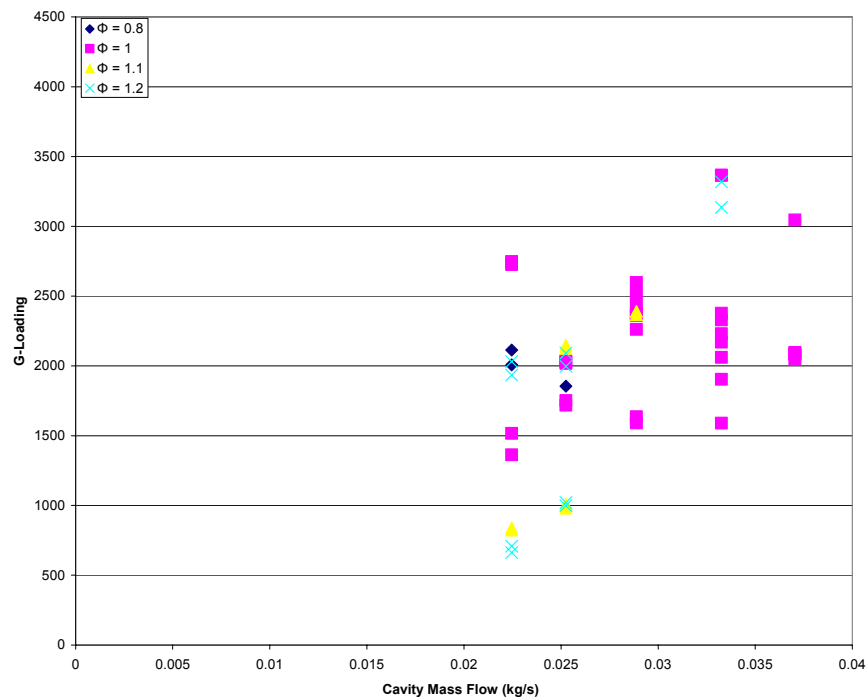


Figure 48: Impact of Φ on G-Loading and Cavity Mass Flow (Position C)

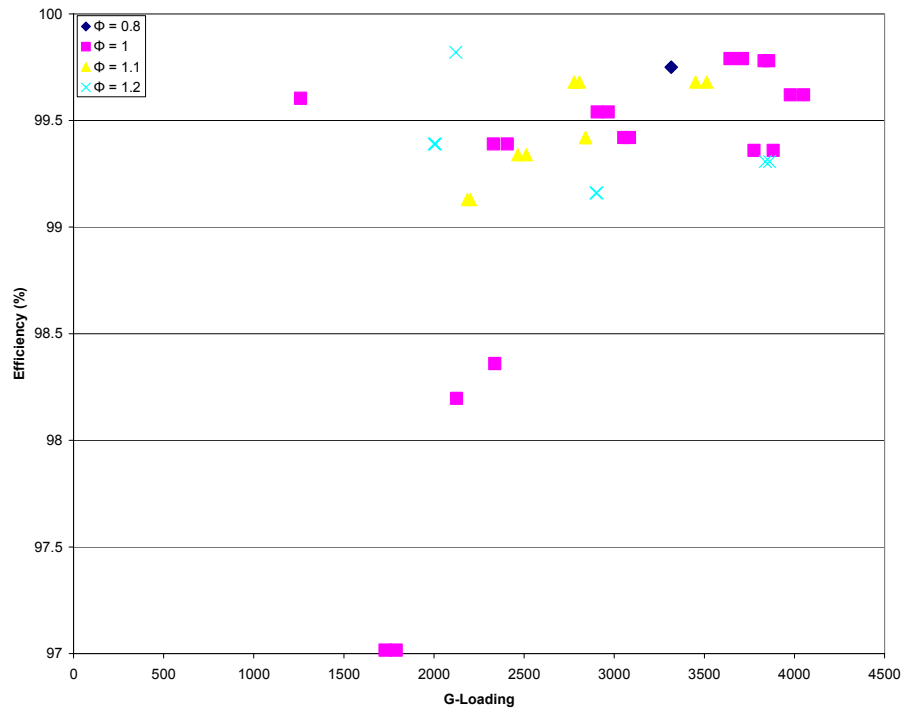


Figure 49: Impact of Φ on Efficiency and G-Loading (Position A)

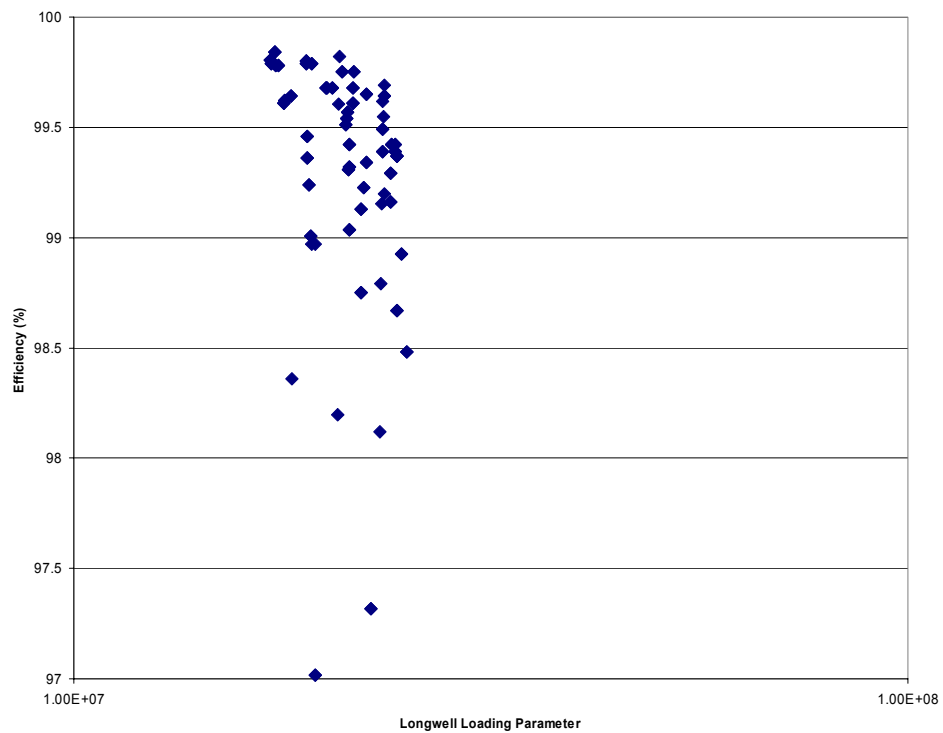


Figure 50: Efficiency with changes in Longwell Loading Parameter

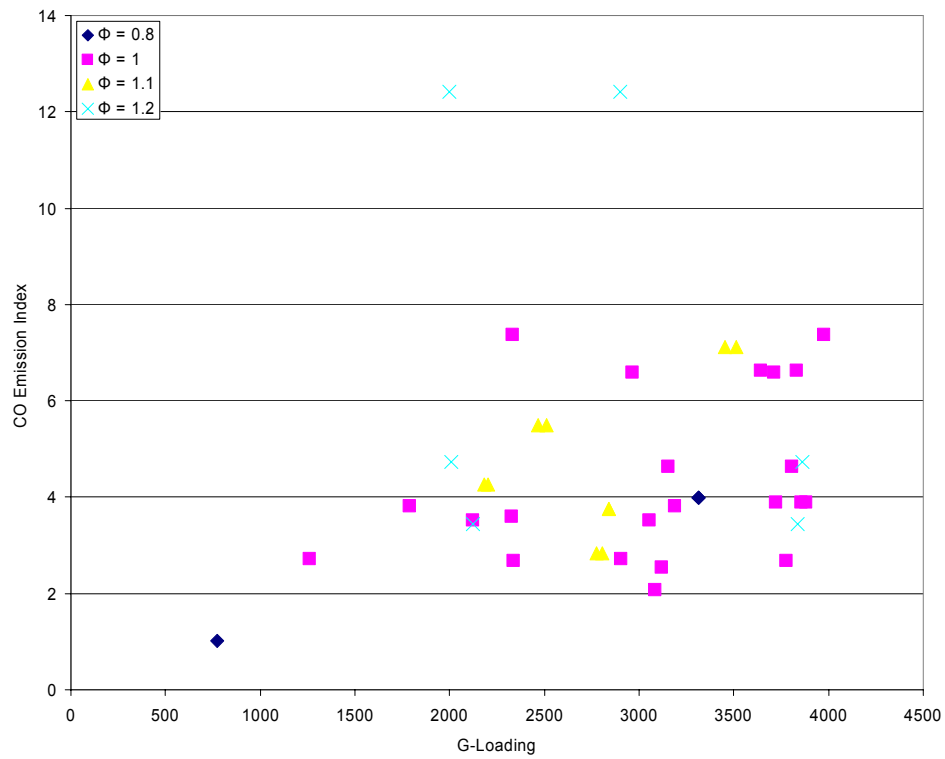


Figure 51: Changes in CO Emission Index with G-Loading (Position A)

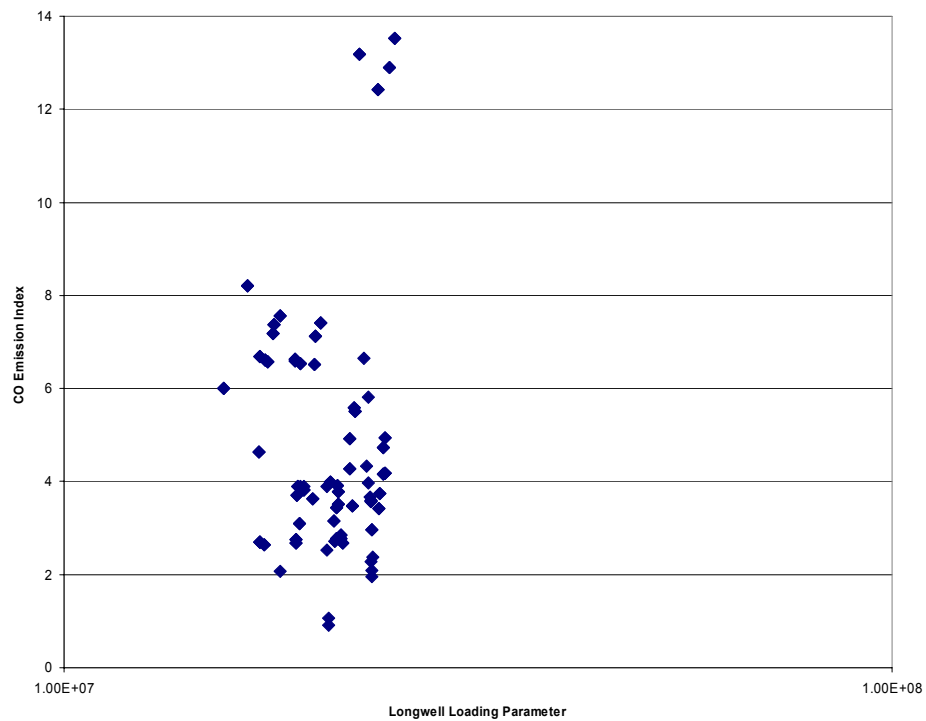


Figure 52: Longwell Loading Parameter and CO Emission Index

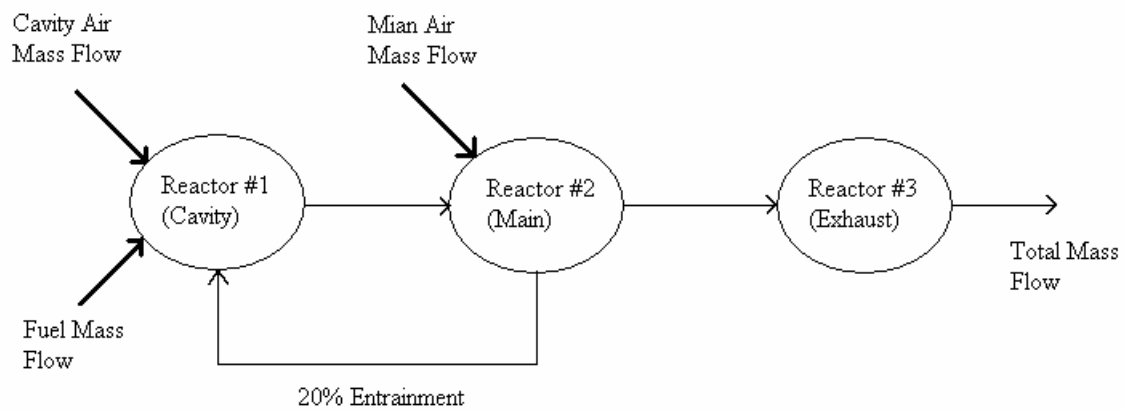


Figure 53: Diagram of Chemical Kinetics Model for the UCC

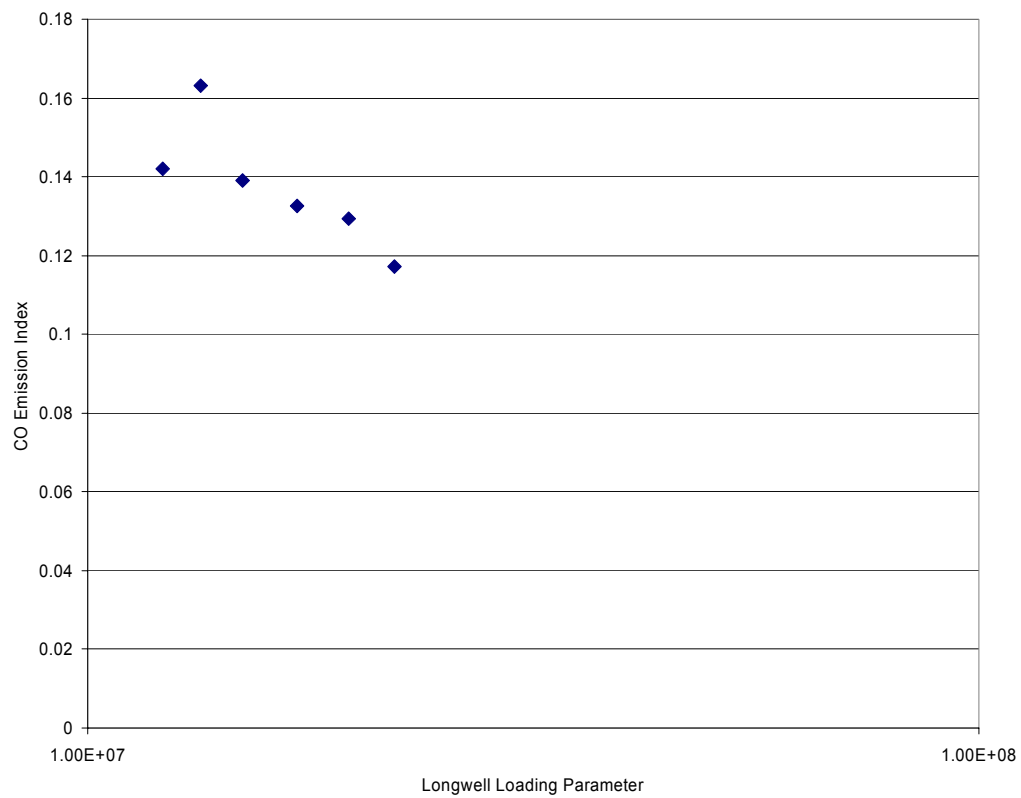


Figure 54: Chemical Kinetics Numerical Results for CO Emission Index with Longwell Loading Parameter

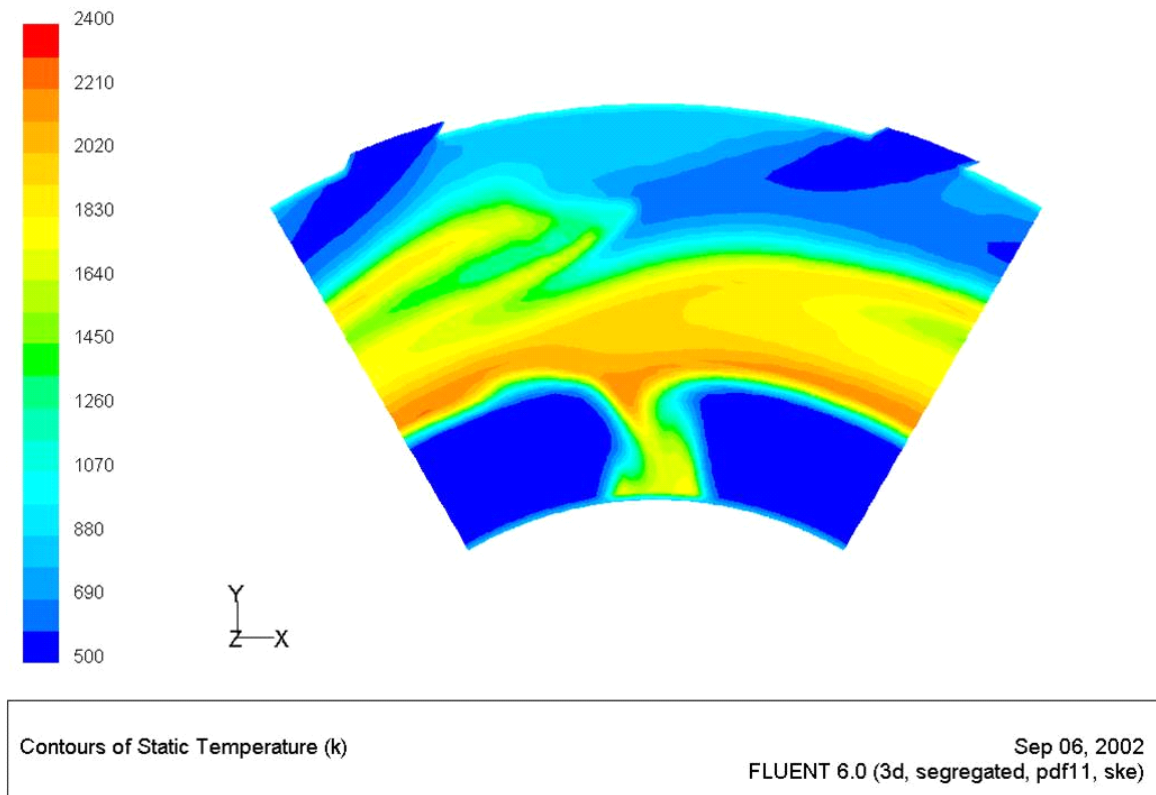


Figure 55: CFD Temperature Plot In Line With the Upstream Pilot Air Jets For 2% Pressure Drop at 22% Cavity Air Mass Flow (used with permission from Ehret, 2002: Appendix A)

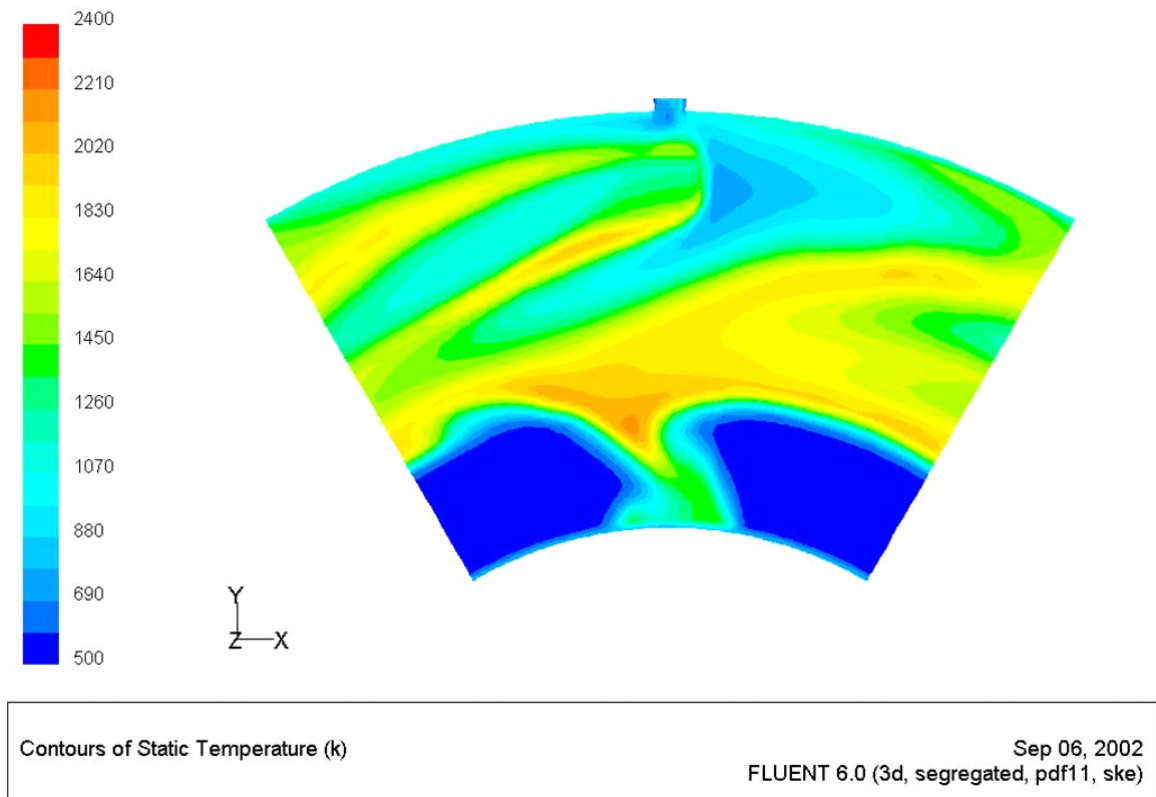
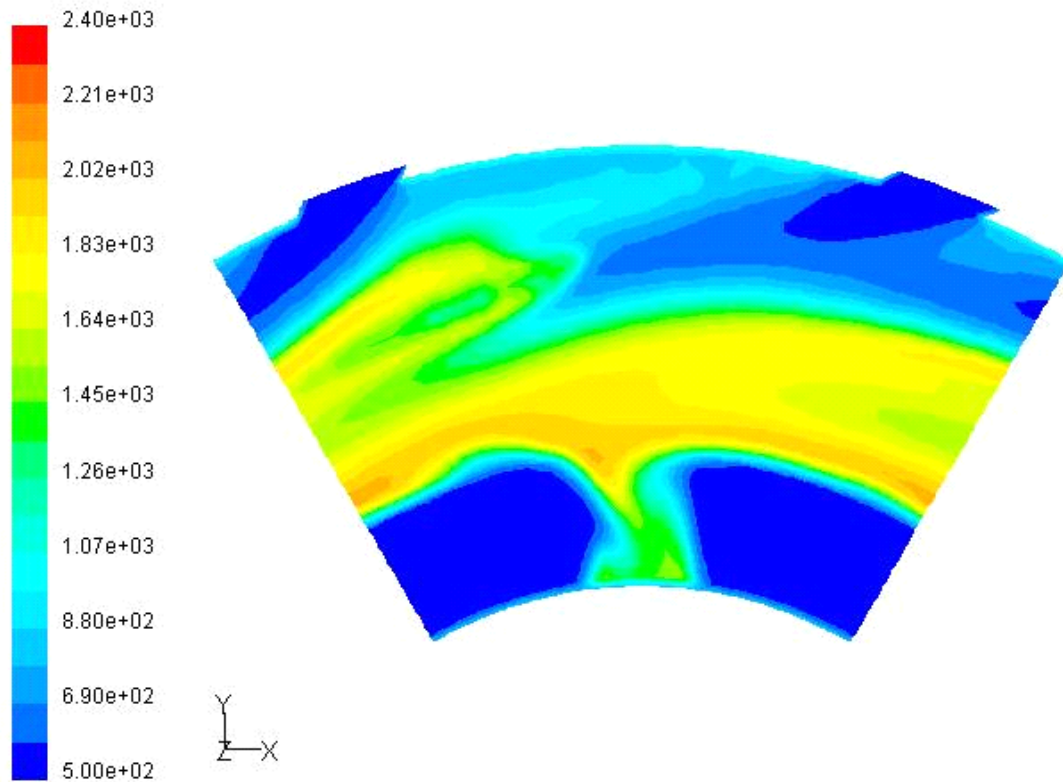


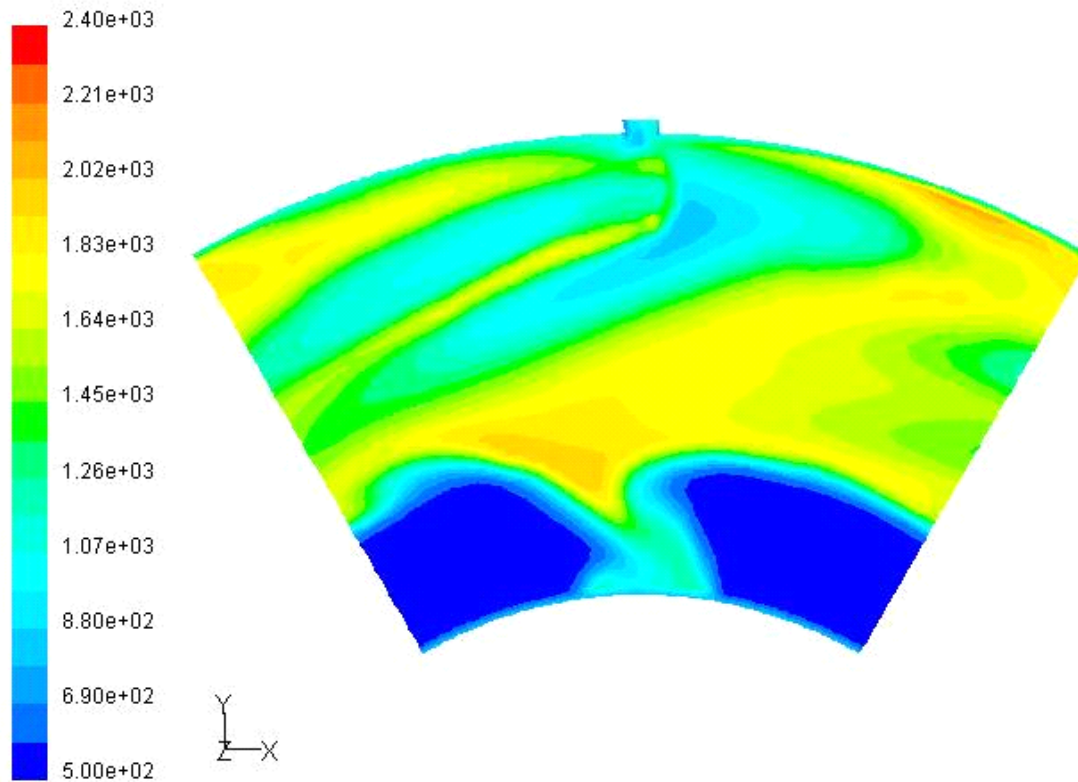
Figure 56: CFD Temperature Plot In Line With the Fuel Injector For 2% Pressure Drop at 22% Cavity Air Mass Flow (used with permission from Ehret, 2002: Appendix A)



Contours of Static Temperature (K)

Sep 06, 2002
FLUENT 6.0 (3d, segregated, pdf11, ske)

Figure 57: CFD Temperature Plot In Line With the Upstream Pilot Air Jets For 4% Pressure Drop at 22% Cavity Air Mass Flow (used with permission from Ehret, 2002: Appendix A)



Contours of Static Temperature (k)

Sep 06, 2002
FLUENT 6.0 (3d, segregated, pdf11, ske)

Figure 58: CFD Temperature Plot In Line With the Fuel Injector For 4% Pressure Drop at 22% Cavity Air Mass Flow (used with permission from Ehret, 2002: Appendix A)

Appendix B: Analytical Derivation

Cavity Air Mass Flow Derivation

Assumptions

$$U_z = 0$$

$$\frac{\partial}{\partial \alpha} U_r = 0 \quad \frac{\partial}{\partial \alpha} U_\theta = 0 \quad \frac{\partial}{\partial \alpha} U_z = 0 \quad \frac{\partial}{\partial \alpha} Y_i = 0 \quad \frac{\partial}{\partial \alpha} T = 0 \quad \frac{\partial}{\partial \alpha} P = 0 \quad \frac{\partial}{\partial \alpha} \rho = 0$$

$$\frac{\partial}{\partial r} U_z = 0$$

$$\frac{\partial}{\partial \theta} U_r = 0 \quad \frac{\partial}{\partial \theta} U_\theta = 0 \quad \frac{\partial}{\partial \theta} U_z = 0 \quad \frac{\partial}{\partial \theta} Y_i = 0 \quad \frac{\partial}{\partial \theta} T = 0 \quad \frac{\partial}{\partial \theta} P = 0$$

$$\frac{\partial}{\partial z} U_r = 0 \quad \frac{\partial}{\partial z} U_\theta = 0 \quad \frac{\partial}{\partial z} U_z = 0 \quad \frac{\partial}{\partial z} Y_i = 0 \quad \frac{\partial}{\partial z} T = 0 \quad \frac{\partial}{\partial z} P = 0$$

Momentum

$$\rho \left(U_r \frac{\partial}{\partial r} U_r - \frac{U_\theta^2}{r} \right) = -\frac{\partial}{\partial r} P + \mu \left[\frac{\partial}{\partial r} \left[\frac{1}{r} \frac{\partial}{\partial r} (r U_r) \right] \right]$$

$$\rho \left(U_r \frac{\partial}{\partial r} U_\theta + \frac{U_\theta U_r}{r} \right) = \mu \left[\frac{\partial}{\partial r} \left[\frac{1}{r} \frac{\partial}{\partial r} (r U_\theta) \right] \right]$$

Continuity

$$\frac{\rho}{r} \frac{\partial}{\partial r} (r U_r) = 0$$

Species

$$\rho \left(U_r \frac{\partial}{\partial r} Y_i \right) + \frac{\rho}{r} \frac{\partial}{\partial r} \left(-r D \frac{\partial}{\partial r} Y_i \right) = \omega_i$$

Energy

$$\rho C_p \left(U_r \frac{\partial}{\partial r} T \right) - \left(U_r \frac{\partial}{\partial r} P \right) = \lambda \left[\frac{1}{r} \frac{\partial}{\partial r} \left(r \frac{\partial}{\partial r} T \right) \right] - \left(\sum_{i=1}^N \omega_i \Delta h_f^o \right)$$

Non - Dimensionalization

$$U_r = U_R \mathbf{U}_r \quad r = R \mathbf{r} \quad U_\theta = U_R \mathbf{U}_\theta \quad z = R \mathbf{z} \quad U_z = U_R \mathbf{U}_z$$

r - component Momentum Non-Dimensionalized then expanded

$$\rho \left[\frac{U_R^2 \mathbf{U}_r}{R} \frac{\partial}{\partial \mathbf{r}} \mathbf{U}_r - \frac{U_R^2 (\mathbf{U}_\theta)^2}{R \mathbf{r}} \right] = \frac{\partial}{\partial \mathbf{r}} P + \frac{\mu U_R}{R^2} \left[\frac{\partial}{\partial \mathbf{r}} \left[\frac{1}{\mathbf{r}} \frac{\partial}{\partial \mathbf{r}} (\mathbf{r} \mathbf{U}_r) \right] \right]$$

$$\frac{U_R^2}{R} \left[\mathbf{U}_r \frac{\partial}{\partial \mathbf{r}} \mathbf{U}_r - \frac{(\mathbf{U}_r)^2}{\mathbf{r}} \right] = \frac{-1}{R \rho} \frac{\partial}{\partial \mathbf{r}} P + \frac{\nu U_R}{R^2} \left[\frac{\partial}{\partial \mathbf{r}} \left(\frac{\mathbf{U}_r}{\mathbf{r}} + \frac{\partial}{\partial \mathbf{r}} \mathbf{U}_r \right) \right]$$

$$U_R \left[\mathbf{U}_r \frac{\partial}{\partial \mathbf{r}} \mathbf{U}_r - \frac{(\mathbf{U}_r)^2}{\mathbf{r}} \right] = \frac{-1}{U_R \rho} \frac{\partial}{\partial \mathbf{r}} P + \frac{\nu}{R} \left[\frac{\partial}{\partial \mathbf{r}} \left(\frac{\mathbf{U}_r}{\mathbf{r}} + \frac{\partial}{\partial \mathbf{r}} \mathbf{U}_r \right) \right]$$

θ - component Momentum Non-Dimensionalized then expanded

$$\rho \left(\frac{U_R^2 \mathbf{u}_r}{R} \frac{\partial}{\partial \mathbf{r}} \mathbf{u}_\theta - \frac{U_R^2 \mathbf{u}_\theta \mathbf{u}_r}{R \mathbf{r}} \right) = \frac{\mu U_R}{R^2} \left[\frac{\partial}{\partial \mathbf{r}} \left[\frac{1}{\mathbf{r}} \frac{\partial}{\partial \mathbf{r}} (\mathbf{r} \mathbf{u}_\theta) \right] \right]$$

$$\frac{U_R^2}{R} \left(\mathbf{u}_r \frac{\partial}{\partial \mathbf{r}} \mathbf{u}_\theta - \frac{\mathbf{u}_\theta \mathbf{u}_r}{\mathbf{r}} \right) = \frac{\nu U_R}{R^2} \left[\frac{\partial}{\partial \mathbf{r}} \left(\frac{\mathbf{u}_\theta}{\mathbf{r}} + \frac{\partial}{\partial \mathbf{r}} \mathbf{u}_\theta \right) \right]$$

$$U_R \left(\mathbf{u}_r \frac{\partial}{\partial \mathbf{r}} \mathbf{u}_\theta - \frac{\mathbf{u}_\theta \mathbf{u}_r}{\mathbf{r}} \right) = \frac{\nu}{R} \left[\frac{\partial}{\partial \mathbf{r}} \left(\frac{\mathbf{u}_\theta}{\mathbf{r}} + \frac{\partial}{\partial \mathbf{r}} \mathbf{u}_\theta \right) \right]$$

Continuity Non-Dimensionalized and expanded

$$\begin{aligned} \frac{\rho U_R}{R \mathbf{r}} \frac{\partial}{\partial \mathbf{r}} (\mathbf{r} \mathbf{u}_r) &= 0 & \frac{\partial}{\partial \mathbf{r}} \mathbf{u}_r &= \frac{-\mathbf{u}_r}{\mathbf{r}} & \frac{1}{\mathbf{u}_r} &= A \mathbf{r} \\ & & -\ln(\mathbf{u}_r) &= \ln(\mathbf{r}) + C & A &= U_R R \\ \frac{\partial}{\partial \mathbf{r}} \mathbf{u}_r + \frac{\mathbf{u}_r}{\mathbf{r}} &= 0 & \frac{1}{e^{\ln(\mathbf{u}_r)}} &= A \mathbf{r} & \mathbf{u}_r &= \frac{U_R R}{\mathbf{r}} \end{aligned}$$

Species and Energy Combined

Species

$$\mathbf{u}_r \frac{\partial}{\partial \mathbf{r}} \mathbf{Y}_i = \frac{D}{R U_R \mathbf{r}} \frac{\partial}{\partial \mathbf{r}} \left(\mathbf{r} \frac{\partial}{\partial \mathbf{r}} \mathbf{Y}_i \right) + \frac{\omega_i R}{U_R \rho}$$

$$\eta_i = \frac{\nu_F}{\nu_i} \mathbf{Y}_i$$

$$\mathbf{u}_r \frac{\partial}{\partial \mathbf{r}} \eta_i = \frac{1}{Pe \mathbf{r}} \frac{\partial}{\partial \mathbf{r}} \left(\mathbf{r} \frac{\partial}{\partial \mathbf{r}} \eta_i \right) + Da$$

Energy

$$\rho C_p U_r \frac{\partial T}{\partial r} = \left[\frac{\lambda}{r} \frac{\partial}{\partial r} \left(r \frac{\partial T}{\partial r} \right) \right] - \omega_F \Delta H_R$$

$$U_r \frac{\partial T}{\partial r} = \frac{\alpha}{U_R R r} \frac{\partial}{\partial r} \left(r \frac{\partial T}{\partial r} \right) - \frac{\omega_F \Delta H_R R}{U_R C_p T_o \rho}$$

$$\eta_T = \frac{-C_p T_o T}{\Delta H_R}$$

$$U_r \frac{\partial \eta_T}{\partial r} = \frac{1}{Pe r} \frac{\partial}{\partial r} \left(r \frac{\partial \eta_T}{\partial r} \right) + Da$$

$$\beta_T = \eta_T - \eta_F$$

$$\beta_O = \eta_O - \eta_F$$

$$\beta_P = \eta_P - \eta_F$$

$$\xi = \frac{\beta_i - \beta_{ii}}{\beta_{io} - \beta_{ii}}$$

Combined

$$U_r \frac{\partial \xi}{\partial r} = \frac{1}{Pe r} \frac{\partial}{\partial r} \left(r \frac{\partial \xi}{\partial r} \right)$$

Boundary Conditions

$$r = R_{inner}$$

$$\xi = 0$$

$$R_{inner} = 1.625in$$

$$r = R_{outer}$$

$$\xi = 1$$

$$R_{outer} = 2.3in$$

Solution

$$\mathbf{U_r} \frac{\partial}{\partial \mathbf{r}} \xi = \frac{1}{Pe} \mathbf{r} \left(\mathbf{r} \frac{\partial^2}{\partial \mathbf{r}^2} \xi + \frac{\partial}{\partial \mathbf{r}} \xi \right)$$

$$Pe \mathbf{U_r} \frac{\partial}{\partial \mathbf{r}} \xi = \frac{\partial^2}{\partial \mathbf{r}^2} \xi + \frac{1}{\mathbf{r}} \frac{\partial}{\partial \mathbf{r}} \xi$$

$$Pe \frac{1}{\mathbf{r}} \frac{\partial}{\partial \mathbf{r}} \xi = \frac{\partial^2}{\partial \mathbf{r}^2} \xi + \frac{1}{\mathbf{r}} \frac{\partial}{\partial \mathbf{r}} \xi$$

$$f = \frac{\partial}{\partial \mathbf{r}} \xi$$

$$Pe \frac{1}{\mathbf{r}} f - \frac{1}{\mathbf{r}} f = \frac{\partial}{\partial \mathbf{r}} f$$

$$\frac{1}{\mathbf{r}} f (Pe - 1) = \frac{\partial}{\partial \mathbf{r}} f$$

$$\frac{1}{\mathbf{r}} (Pe - 1) = \frac{1}{f} \left(\frac{\partial}{\partial \mathbf{r}} f \right)$$

Separate Variables and Integrate

$$\ln(\mathbf{r}) (Pe - 1) + C = \ln(f)$$

$$B \mathbf{r}^{(Pe-1)} = \frac{\partial}{\partial \mathbf{r}} \xi$$

$$\xi = \frac{D}{Pe} \mathbf{r}^{Pe} + E$$

Apply Boundary Conditions

$$1 = \frac{D}{Pe} R_{outer}^{Pe} + E$$

$$0 = \frac{D}{Pe} R_{inner}^{Pe} + E$$

$$1 = \frac{D}{Pe} \left(R_{outer}^{Pe} - R_{inner}^{Pe} \right)$$

$$D = \frac{Pe}{R_{outer}^{Pe} - R_{inner}^{Pe}}$$

$$E = \frac{-D}{Pe} R_{inner}^{Pe}$$

$$E = \frac{R_{inner}^{Pe}}{R_{inner}^{Pe} - R_{outer}^{Pe}}$$

$$Pe = \frac{\mathbf{U_r} R_{outer}}{\alpha}$$

Main Air Mass Flow Derivation

Assumptions

$$\frac{\partial}{\partial t} U_r = 0 \quad \frac{\partial}{\partial t} U_\theta = 0 \quad \frac{\partial}{\partial t} U_z = 0 \quad \frac{\partial}{\partial t} Y_i = 0 \quad \frac{\partial}{\partial t} T = 0 \quad \frac{\partial}{\partial t} P = 0 \quad \frac{\partial}{\partial t} \rho = 0$$

$$\frac{\partial}{\partial r} U_z = 0 \quad \frac{\partial}{\partial r} P = 0$$

$$\frac{\partial}{\partial \theta} U_r = 0 \quad \frac{\partial}{\partial \theta} U_\theta = 0 \quad \frac{\partial}{\partial \theta} U_z = 0 \quad \frac{\partial}{\partial \theta} Y_i = 0 \quad \frac{\partial}{\partial \theta} T = 0 \quad \frac{\partial}{\partial \theta} P = 0$$

$$\frac{\partial}{\partial z} U_r = 0 \quad \frac{\partial}{\partial z} U_\theta = 0 \quad \frac{\partial}{\partial z} Y_i = 0$$

Momentum

$$\rho \left(U_r \frac{\partial}{\partial r} U_r - \frac{U_\theta^2}{r} + U_z \frac{\partial}{\partial z} U_r \right) = -\frac{\partial}{\partial r} P + \mu \left[\frac{\partial}{\partial r} \left[\frac{1}{r} \frac{\partial}{\partial r} (r U_r) \right] + \frac{\partial^2}{\partial z^2} U_r \right]$$

$$\rho \left(U_r \frac{\partial}{\partial r} U_\theta + \frac{U_\theta U_r}{r} + U_z \frac{\partial}{\partial z} U_\theta \right) = \mu \left[\frac{\partial}{\partial r} \left[\frac{1}{r} \frac{\partial}{\partial r} (r U_\theta) \right] + \frac{\partial^2}{\partial z^2} U_\theta \right]$$

$$\rho U_z \frac{\partial}{\partial z} U_z = \mu \left[\frac{1}{r} \frac{\partial}{\partial r} \left(r \frac{\partial}{\partial r} U_z \right) + \frac{\partial^2}{\partial z^2} U_z \right] - \frac{\partial}{\partial z} P$$

Continuity

$$\frac{\rho}{r} \frac{\partial}{\partial r} (r U_r) + \rho \left(\frac{\partial}{\partial z} U_z \right) = 0$$

Species

$$\rho \left(U_r \frac{\partial}{\partial r} Y_i \right) + \frac{\rho}{r} \frac{\partial}{\partial r} \left(-r D \frac{\partial}{\partial r} Y_i \right) = \omega_i$$

Energy

$$\rho C_p \left(U_r \frac{\partial}{\partial r} T \right) = \lambda \left[\frac{1}{r} \frac{\partial}{\partial r} \left(r \frac{\partial}{\partial r} T \right) + \frac{\partial^2}{\partial z^2} T \right] - \left(\sum_{i=1}^N \omega_i \Delta h_f^o \right)$$

Non - Dimensionalization

$$U_r = \mathbf{U}_r U_R \quad r = \mathbf{r} R \quad U_\theta = \mathbf{U}_\theta U_R \quad z = \mathbf{z} R \quad U_z = \mathbf{U}_z U_R$$

r - component Momentum Non-Dimensionalized then expanded

$$\rho \left[\frac{U_R^2 \mathbf{U}_r}{R} \frac{\partial}{\partial \mathbf{r}} \mathbf{U}_r - \frac{U_R^2 (\mathbf{U}_\theta)^2}{R \mathbf{r}} + \frac{U_R^2 \mathbf{U}_z}{R} \frac{\partial}{\partial \mathbf{z}} \mathbf{U}_r \right] = \frac{\mu U_R}{R^2} \left[\frac{\partial}{\partial \mathbf{r}} \left[\frac{1}{\mathbf{r}} \frac{\partial}{\partial \mathbf{r}} (\mathbf{r} \mathbf{U}_r) \right] + \frac{\partial^2}{\partial \mathbf{z}^2} \mathbf{U}_r \right]$$

$$\frac{U_R^2}{R} \left[\mathbf{U}_r \frac{\partial}{\partial \mathbf{r}} \mathbf{U}_r - \frac{(\mathbf{U}_\theta)^2}{\mathbf{r}} + \mathbf{U}_z \frac{\partial}{\partial \mathbf{z}} \mathbf{U}_r \right] = \frac{\nu U_R}{R^2} \left[\frac{\partial}{\partial \mathbf{r}} \left(\frac{\mathbf{U}_r}{\mathbf{r}} + \frac{\partial}{\partial \mathbf{r}} \mathbf{U}_r \right) + \frac{\partial^2}{\partial \mathbf{z}^2} \mathbf{U}_r \right]$$

$$U_R \left[\mathbf{U}_r \frac{\partial}{\partial \mathbf{r}} \mathbf{U}_r - \frac{(\mathbf{U}_\theta)^2}{\mathbf{r}} + \mathbf{U}_z \frac{\partial}{\partial \mathbf{z}} \mathbf{U}_r \right] = \frac{\nu}{R} \left[\frac{\partial}{\partial \mathbf{r}} \left(\frac{\mathbf{U}_r}{\mathbf{r}} + \frac{\partial}{\partial \mathbf{r}} \mathbf{U}_r \right) + \frac{\partial^2}{\partial \mathbf{z}^2} \mathbf{U}_r \right]$$

$$\mathbf{U}_r \frac{\partial}{\partial \mathbf{r}} \mathbf{U}_r - \frac{(\mathbf{U}_\theta)^2}{\mathbf{r}} + \mathbf{U}_z \frac{\partial}{\partial \mathbf{z}} \mathbf{U}_r = \frac{1}{Re} \left[\frac{\partial}{\partial \mathbf{r}} \left(\frac{\mathbf{U}_r}{\mathbf{r}} + \frac{\partial}{\partial \mathbf{r}} \mathbf{U}_r \right) + \frac{\partial^2}{\partial \mathbf{z}^2} \mathbf{U}_r \right]$$

θ - component Momentum Non-Dimensionalized then expanded

$$\rho \left(\frac{U_R^2 \mathbf{u}_r}{R} \frac{\partial}{\partial r} \mathbf{u}_\theta - \frac{U_R^2 \mathbf{u}_\theta \mathbf{u}_r}{R r} + \frac{U_R^2 \mathbf{u}_z}{R} \frac{\partial}{\partial z} \mathbf{u}_\theta \right) = \frac{\mu U_R}{R^2} \left[\frac{\partial}{\partial r} \left[\frac{1}{r} \frac{\partial}{\partial r} (r \mathbf{u}_\theta) \right] + \frac{\partial^2}{\partial z^2} \right]$$

$$\frac{U_R^2}{R} \left(\mathbf{u}_r \frac{\partial}{\partial r} \mathbf{u}_\theta - \frac{\mathbf{u}_\theta \mathbf{u}_r}{r} + \mathbf{u}_z \frac{\partial}{\partial z} \mathbf{u}_\theta \right) = \frac{\nu U_R}{R^2} \left[\frac{\partial}{\partial r} \left(\frac{\mathbf{u}_\theta}{r} + \frac{\partial}{\partial r} \mathbf{u}_\theta \right) + \frac{\partial^2}{\partial z^2} \mathbf{u}_\theta \right]$$

$$U_R \left(\mathbf{u}_r \frac{\partial}{\partial r} \mathbf{u}_\theta - \frac{\mathbf{u}_\theta \mathbf{u}_r}{r} + \mathbf{u}_z \frac{\partial}{\partial z} \mathbf{u}_\theta \right) = \frac{\nu}{R} \left[\frac{\partial}{\partial r} \left(\frac{\mathbf{u}_\theta}{r} + \frac{\partial}{\partial r} \mathbf{u}_\theta \right) + \frac{\partial^2}{\partial z^2} \mathbf{u}_\theta \right]$$

$$\mathbf{u}_r \frac{\partial}{\partial r} \mathbf{u}_\theta - \frac{\mathbf{u}_\theta \mathbf{u}_r}{r} + \mathbf{u}_z \frac{\partial}{\partial z} \mathbf{u}_\theta = \frac{1}{Re} \left[\frac{\partial}{\partial r} \left(\frac{\mathbf{u}_\theta}{r} + \frac{\partial}{\partial r} \mathbf{u}_\theta \right) + \frac{\partial^2}{\partial z^2} \mathbf{u}_\theta \right]$$

z - component Momentum Non-Dimensionalized then expanded

$$\rho \left(\frac{U_R^2 \mathbf{u}_z}{R} \frac{\partial}{\partial z} \mathbf{u}_z + \frac{U_R^2 \mathbf{u}_r}{R} \frac{\partial}{\partial r} \mathbf{u}_z \right) = -\frac{\partial P}{\partial z} + \frac{\mu U_R}{R^2} \left[\frac{1}{r} \frac{\partial}{\partial r} \left(r \frac{\partial}{\partial r} \mathbf{u}_z \right) + \frac{\partial^2}{\partial z^2} \mathbf{u}_z \right]$$

$$\frac{U_R^2}{R} \left(\mathbf{u}_z \frac{\partial}{\partial z} \mathbf{u}_z + \mathbf{u}_r \frac{\partial}{\partial r} \mathbf{u}_z \right) = \frac{-1}{R \rho} \frac{\partial P}{\partial z} + \frac{\nu U_R}{R^2} \left[\frac{1}{r} \frac{\partial}{\partial r} \left(r \frac{\partial}{\partial r} \mathbf{u}_z \right) + \frac{\partial^2}{\partial z^2} \mathbf{u}_z \right]$$

$$U_R \left(\mathbf{u}_z \frac{\partial}{\partial z} \mathbf{u}_z + \mathbf{u}_r \frac{\partial}{\partial r} \mathbf{u}_z \right) = \frac{-1}{\rho U_R} \frac{\partial P}{\partial z} + \frac{\nu}{R} \left[\frac{1}{r} \frac{\partial}{\partial r} \left(r \frac{\partial}{\partial r} \mathbf{u}_z \right) + \frac{\partial^2}{\partial z^2} \mathbf{u}_z \right]$$

$$\mathbf{u}_z \frac{\partial}{\partial z} \mathbf{u}_z + \mathbf{u}_r \frac{\partial}{\partial r} \mathbf{u}_z = \frac{-1}{\rho U_R^2} \frac{\partial P}{\partial z} + \frac{1}{Re} \left[\frac{1}{r} \frac{\partial}{\partial r} \left(r \frac{\partial}{\partial r} \mathbf{u}_z \right) + \frac{\partial^2}{\partial z^2} \mathbf{u}_z \right]$$

$$\frac{\rho}{R} \frac{U_R}{r} \frac{\partial}{\partial r} (r \mathbf{u}_r) + \frac{\rho}{R} \frac{U_R}{r} \frac{\partial}{\partial z} (\mathbf{u}_z) = 0$$

$$\frac{\partial}{\partial r} \mathbf{u}_r + \frac{\mathbf{u}_r}{r} + \frac{\partial}{\partial z} \mathbf{u}_z = 0$$

Species and Energy Combined

Species

$$\mathbf{u}_r \frac{\partial}{\partial r} Y_i = \frac{D}{R U_R} \frac{\partial}{\partial r} \left(r \frac{\partial}{\partial r} Y_i \right) + \frac{\omega_i R}{U_R \rho}$$

$$\eta_i = \frac{v_F}{v_i} Y_i$$

$$\mathbf{u}_r \frac{\partial}{\partial r} \eta_i = \frac{1}{Pe} \frac{\partial}{\partial r} \left(r \frac{\partial}{\partial r} \eta_i \right) + Da$$

Energy

$$\rho C_p U_r \frac{\partial}{\partial r} T = \left[\frac{\lambda}{r} \frac{\partial}{\partial r} \left(r \frac{\partial}{\partial r} T \right) \right] - \omega_F \Delta H_R$$

$$\mathbf{u}_r \frac{\partial}{\partial r} T = \frac{\alpha}{U_R R} \frac{\partial}{\partial r} \left(r \frac{\partial}{\partial r} T \right) - \frac{\omega_F \Delta H_R R}{U_R C_p T_o \rho}$$

$$\eta_T = \frac{-C_p T_o T}{\Delta H_R}$$

$$\mathbf{u}_r \frac{\partial}{\partial r} \eta_T = \frac{1}{Pe} \frac{\partial}{\partial r} \left(r \frac{\partial}{\partial r} \eta_T \right) + Da$$

$$\beta_{TO} = \eta_T - \eta_O$$

$$\beta_T = \eta_T - \eta_F$$

$$\beta_O = \eta_O - \eta_F$$

$$\beta_P = \eta_P - \eta_F$$

$$\xi = \frac{\beta_i - \beta_{io}}{\beta_{ii} - \beta_{io}}$$

Combined

$$\mathbf{U}_r \frac{\partial}{\partial \mathbf{r}} \xi = \frac{1}{Pe} \frac{\partial}{\partial \mathbf{r}} \left(\mathbf{r} \frac{\partial}{\partial \mathbf{r}} \xi \right)$$

Boundary Conditions

| | | |
|-------------------------------|-----------|---------------------------|
| $\mathbf{r} = R_{centerbody}$ | $\xi = 1$ | $R_{centerbody} = 1.25in$ |
| $\mathbf{r} = R_{outer}$ | $\xi = 0$ | $R_{outer} = 1.625in$ |

Appendix C: Recommendations

Numerous complications and problems arose in the process of capturing the experimental data. One of the major obstacles was keeping the quartz window clear of soot and seed to allow the laser to penetrate and light scatter to escape. A hole was drilled in the mounting flange across from the test section to allow shop air supply for blowing seed off the quartz window. The quartz window also rested on a thin piece of aluminum shaped like a “C” mounted on top of the liner ring. This aluminum piece created a gap for a small amount of air from the pressurized cavity (plenum) to blow across the window in the test section for removing excess seed. Taking data from soot particles and the remaining artificial seed in the tubes produced the fewest complications. During cold flow testing fuel particles were a relatively reliable method of seeding as well. However, it must be noted that soot and fuel particles may not follow the flow as well as artificial seed.

Fastening and sealing the quartz window to the UCC structure was also difficult. Each time a test was completed the silicone sealant around the edges was replaced because it eventually deteriorated from the high combustion temperatures. Although the combustor was atmospheric there was enough pressure to force the quartz window off the UCC when the fuel and air were ignited. The bolts and spring structure holding the quartz window had to be tightened completely to keep the flame from blowing out. Through this process the quartz window was shattered each time either from the static or thermal load and had to be replaced. A better apparatus to view LDV data should be investigated to reduce testing cost and tear down time.

The major time consuming obstacle was a complication with the laser power unit. The power unit requires water in and out capability for cooling purposes. The water attachments on the unit are in very close proximity to all the electrical equipment and circuit boards. Other testing in the building required a tremendous amount of water so an additional pump was added in line with the unit to provide the required pressure to cool the unit. When the other tests were completed the pressure spiked and caused a leak on the fittings going into the power unit. There is no water resistant cover on the unit so a circuit board was destroyed. Future testing should incorporate an extremely robust hose and fitting system. A steel tubing configuration that bends the hose fittings away from the unit would be more effective.

Bibliography

- Anderson J.D. Jr., *Modern Compressible Flow*, McGraw-Hill Book Company, New York NY, 1990.
- Anthenien, R.A., Mantz, R.A., Roquemore, W.M., and Sturgess, G.J., “Experimental Results for a Novel, High Swirl, Ultra Compact Combustor for Gas Turbine Engines,” Presented at the Western States Section Combustion Institute Meeting, Berkely CA, April, 2001.
- Boutier, A., “Accuracy of Laser Velocimetry,” von Karman Institute for Fluid Dynamics, Onera France, Lecture Series 1991-05.
- Drain, L.E., *The Laser Doppler Technique*, John Wiley & Sons Ltd., Norwich Great Britain, 1980.
- Ehret, J., “Design Optimization of a High-G Loaded Ultra-Compact Combustor,” *M.S. Thesis, Wright State University*, Dayton OH, 2002.
- Glassman I., *Combustion*, American Press Inc., London NW1 7DX, UK, 1996.
- Heneghan, S.P. and Frayne, C.W., “Propagation of Errors for Combustion Analysis Using Emission Analyzer Data,” 38th AIAA Aerospace Sciences Meeting & Exhibit, Reno NV, AIAA-2000-0955, 2000.
- Kanury, A.M., *Introduction to Combustion Phenomena*, Gordon and Breach, Inc., New York NY, 1975.
- Kee, R. J., Rupley, F. M., Miller, J. A., Coltrin, M. E., Grcar, J. F., Meeks, E., Moffat, H. K., Lutz, A. E., Dixon-Lewis, G., Smooke, M. D., Warnatz, J., Evans, G. H., Larson, R. S., Mitchell, R. E., Petzold, L. R., Reynolds, W. C., Caracotsios, M., Stewart, W. E., Glarborg, P., Wang, C., Adigun, O., Houf, W., Chou, C. P., and Miller, S. F., Chemkin Collection, Release 3.7, Reaction Design, Inc., San Diego, CA (2002).
- Kundu P.K., Cohen I.M., *Fluid Mechanics*, Academic Press Inc., London NW1 7BY, UK 2002.
- Kuo K.K., *Principles of Combustion*, John Wiley & Sons Ltd., Norwich Great Britain, 1986.
- Lefebvre, A.H., *Gas Turbine Combustion*, Hemisphere Publishing Corporation, McGraw-Hill Book Company, New York NY, 1999.

- Lewis, G.D., "Centrifugal-Force Effects on Combustion," *Fourteenth Symposium (International) on Combustion*, The Combustion Institute, pp.413-419, 1973.
- . "Swirling Flow Combustion – Fundamentals and Application," AIAA/SAE 9th Propulsion Conference, Las Vegas NV, AIAA-73-1250, 1973.
- Liu, F., Sirignano, W.A., "Turbojet and Turbofan Engine Performance Increases Through Turbine Burners," 38th Aerospace Sciences Meeting & Exhibit, Reno NV, AIAA-2000-0741, 2000.
- Mattingly, J.D., *Elements of Gas Turbine Propulsion*, McGraw-Hill, Inc., New York NY, 1996.
- Roquemore, W.M., Shouse, D., Burrus, D., Johnson, A., Cooper, C., Duncan, B., Hsu, K.-Y., Katta, V.R., Sturgess, G.J., and Vihinen, I., "Trapped Vortex Combustor Concept for Gas Turbine Engines," 39th AIAA Aerospace Sciences Meeting & Exhibit, Reno NV, AIAA-2001-0483, 2001.
- Sherman, F.S., *Viscous Flow*, McGraw-Hill, Inc., New York NY, 1990.
- Sirignano, W.A., Liu, F., "Performance Increases for Gas-Turbine Engines Through Combustion Inside the Turbine," *Journal of Propulsion and Power*, Vol. 15:1, pp.111-118, 1999.
- . Delplanque, J.P., and Liu, F., "Selected Challenges in Jet and Rocket Engine Combustion Research," 33rd AIAA/ASME/SAE/ASEE Joint Propulsion Conference & Exhibit, Seattle WA, AIAA-97-2701, 1997.
- Society of Automotive Engineers (SAE). Procedures for the Calculation of Gaseous Emissions From Aircraft Turbine Engines. ARP1533, Warrendale, PA: 1996-01
- Warantz J., Maas U., Dibble R.W., *Combustion: Physical and Chemical Fundamentals, Modeling and Simulation, Experiments, Pollutant Formation*, Springer-Verlag, Berlin Heidelberg NY, 2001.
- Wheeler, A.J., Ganji, A.R., *Introduction to Engineering Experimentation*, Prentice Hall Inc., Simon & Schuster, Upper Saddle River NJ, 1996.
- White F.M., *Viscous Fluid Flow*, McGraw-Hill Book Company, New York NY, 1991.
- Yonezawa, Y., Toh, H., Goto, S. and Obata, M., "Development of the Jet-Swirl High Loading Combustor," AIAA/SAE/ASME/ASEE 26th Joint Propulsion Conference, Orlando FL, AIAA-90-2451, 1990.

Zelina, J., "Combustion Studies in a Well-Stirred Reactor," *Ph.D. Thesis, University of Dayton*, Dayton OH, 1995.

Zelina, J., Ballal, D.R., "Combustion Stability and Emissions Research Using a Well-Stirred Reactor," ASME IGTI 95-GT-109, 1995.

Vita

Ryan grew up in Seattle where he aspired to play college football and become an engineer since the 5th grade. In the summer of 1994 he entered the United States Air Force Academy as a student and intercollegiate athlete with the hopes of eventually becoming an officer in the United States Air Force. Ryan took a major in Mechanical Engineering and a minor in Mathematics and enjoyed his experiences playing football, making friends and learning.

In the summer of 1998 he married his wife who is also from Seattle. They took an assignment in Colorado Springs coaching football and teaching at the United States Air Force Academy Preparatory School. In May of 1999 Ryan was moved to Wright-Patterson AFB and took an assignment in the C-17 System Program Office. He served as the C-17 hydraulics engineer and also received an MS in Engineering Management from the University of Dayton. In August of 2001 his desire for a technical graduate degree led him to attend the Air Force Institute of Technology (AFIT) for an MS in Aeronautical Engineering.

| REPORT DOCUMENTATION PAGE | | | | Form Approved OMB No. 074-0188 | |
|---|------------------|-----------------------------------|---|--|---|
| <p>The public reporting burden for this collection of information is estimated to average 1 hour per response, including the time for reviewing instructions, searching existing data sources, gathering and maintaining the data needed, and completing and reviewing the collection of information. Send comments regarding this burden estimate or any other aspect of the collection of information, including suggestions for reducing this burden to Department of Defense, Washington Headquarters Services, Directorate for Information Operations and Reports (0704-0188), 1215 Jefferson Davis Highway, Suite 1204, Arlington, VA 22202-4302. Respondents should be aware that notwithstanding any other provision of law, no person shall be subject to a penalty for failing to comply with a collection of information if it does not display a currently valid OMB control number.</p> <p>PLEASE DO NOT RETURN YOUR FORM TO THE ABOVE ADDRESS.</p> | | | | | |
| 1. REPORT DATE (DD-MM-YYYY) 25-03-2003 | | 2. REPORT TYPE Master's Thesis | | 3. DATES COVERED (From – To) Jun 2002 – Mar 2003 | |
| 4. TITLE AND SUBTITLE EXPERIMENTAL RESULTS FOR A HIGH SWIRL, ULTRA COMPACT COMBUSTOR FOR GAS TURBINE ENGINES | | | | 5a. CONTRACT NUMBER | |
| | | | | 5b. GRANT NUMBER | |
| | | | | 5c. PROGRAM ELEMENT NUMBER | |
| 6. AUTHOR(S) Quaale, Ryan, J., Captain, USAF | | | | 5d. PROJECT NUMBER | |
| | | | | 5e. TASK NUMBER | |
| | | | | 5f. WORK UNIT NUMBER | |
| 7. PERFORMING ORGANIZATION NAMES(S) AND ADDRESS(S) Air Force Institute of Technology Graduate School of Engineering and Management (AFIT/EN) 2950 P Street, Building 640 WPAFB OH 45433-7765 | | | | 8. PERFORMING ORGANIZATION REPORT NUMBER AFIT/GAE/ENY/03-5 | |
| 9. SPONSORING/MONITORING AGENCY NAME(S) AND ADDRESS(ES) Dr. Julian Tishkoff AFOSR/NA 801 North Randolph Street Room 732 Arlington, VA 22203-1977 | | | | 10. SPONSOR/MONITOR'S ACRONYM(S) | |
| | | | | 11. SPONSOR/MONITOR'S REPORT NUMBER(S) | |
| 12. DISTRIBUTION/AVAILABILITY STATEMENT APPROVED FOR PUBLIC RELEASE; DISTRIBUTION UNLIMITED. | | | | | |
| 13. SUPPLEMENTARY NOTES | | | | | |
| 14. ABSTRACT Laser Doppler Velocimeter (LDV) experiments have been conducted within the cavity of an Ultra Compact Combustor (UCC). The UCC uses highly swirled flow in a cavity around the outside periphery of the combustor to generate high centripetal acceleration in the fluid for enhanced mixing. Residence time is provided by the circumference of the engine rather than axial length. These two effects produce observed flame lengths less than half those of conventional combustors. Short flame lengths lead to reduced engine size and weight and make inter-turbine burning (ITB) reheat cycles possible for aircraft engines. The ITB reheat cycle has shown potential for large gains in specific thrust (>50%) with equal or reduced thrust specific fuel consumption. LDV measurements indicate circumferential velocities of ~20-50 m/s with turbulence intensities of ~20%. These velocities correspond to accelerations of ~1000-4000g. | | | | | |
| 15. SUBJECT TERMS High Swirl, Ultra Compact Combustor, Combustion, High g-loading, LDV Measurements for Combustion, Inter-turbine Burning, Reheat Cycle, Short Flame Length, High Centripetal Acceleration, Velocity Measurements, Increased Turbine Blade Life, Gas Turbine Engines, Gas Turbine Engine Combustion | | | | | |
| 16. SECURITY CLASSIFICATION OF: | | | 17. LIMITATION OF ABSTRACT UU | 18. NUMBER OF PAGES 131 | 19a. NAME OF RESPONSIBLE PERSON Ralph A. Anthenien, Capt, USAF (ENY) |
| a. REPORT U | b. ABSTRACT U | c. THIS PAGE U | | | 19b. TELEPHONE NUMBER (Include area code) (937) 255-3636, ext 4643; e-mail: Ralph.Anthenien@afit.edu |